Neutron-Star Equation of State and Its Thermal Evolution

土肥, 明

Doctral Thesis

Neutron-Star Equation of State and Its Thermal Evolution

Dissertation Submitted to Kyushu University
for the Degree of Doctor of Science

Akira Dohi

Theories of Particle Physics, Nuclear Physics and Astrophysics/Astronomy,
Department of Physics, Graduate School of Science, Kyushu University

September 2022

Abstract

Neutron stars (NSs) are compact objects with a typical mass of 1.4 $M_\odot$ and a radius of about 12 km. A central density of NSs reaches several times the nuclear saturation density. Neutron stars consist of a thin, low-density outer crust of about several hundred meters and a thick, high-density inner core. Since the core is affected by highly uncertain nuclear forces due to the ultra-high density environment, the equation of state (EOS) for the dense matter describing the inner structure is still unknown. Furthermore, there is no reliable experiment to probe the high-density and relatively low-temperature regions of NSs. To constrain the EOS that describes the properties of dense matter, model comparisons with observations of NSs have been widely done for a long year.

With the recent progress of X-ray astronomy, observed temperature and luminosities of NSs have been used for constraining the EOS with theoretical models of their thermal evolution. Isolated NSs born from supernova explosions cool down by mainly neutrino emissions. Since the neutrinos are produced by fundamental processes inside the NS, their emissivity highly depends on the EOS. Most temperature observations of isolated NSs can be explained by a minimal cooling scenario, which includes slow cooling processes and nucleon superfluid effects. However, some NSs are too cold to be explained. To reproduce them, some enhanced cooling processes, such as the nucleon direct Urca (DU) process and a pion condensation, are necessary. The threshold of such fast cooling processes is determined by the compositions inside NSs, and therefore temperature observations enable us to constrain the EOS, including the strength of nucleon superfluidity.

Neutron stars often form binary systems with other stellar objects. When the companion star is a light star with less than the mass of the Sun, accretion from the companion star to the NS always occurs through the accretion disk, resulting in gravitational energy release and heating process in the crust due to a transformation of accreted matter into heavier nuclei in some exothermal reactions. Such accreting NSs have periods of outburst phase alternating with quiescent phases, where the surface temperatures are $T \lesssim 0.1$ keV and $T \gtrsim$ keV, respectively. As with the isolated NSs, some accreting NSs in the quiescent phase are observationally cold enough to require fast cooling processes.

During the outburst phase, rapidly brightening events called Type-I X-ray burst have often been observed. This is thought to be triggered by unstable nuclear burning of hydrogen and helium onto the surface of accreting NSs. After igniting the light elements, the rapid-proton capture (rp) process finally occurs in bursting NSs. Thus, X-ray bursts are powerful sites for the synthesis of proton-rich (p-nuclei) heavy elements. Among 115 X-ray bursts observed so far, GS 1826–24 is an exceptionally regular burster where the shape of the light curves during a series of outbursts is constant. Therefore, GS 1826–24 is a useful observation for constraining burst models. In fact, several studies have done numerical modelings for GS 1826–24, which can probe uncertainties of several parameters related to the NS exterior, such as the mass accretion rate and composition of accreted material. However, no previous studies have examined the influence of the physics inside NSs, such as the EOSs and neutrino cooling effects in the core.

In this study, we focus on the effects of EOS uncertainties on the various thermal evolution of NSs. We take several EOSs with different properties and perform numerical simulations of

the thermal evolution of NSs covering entire stars. In the cooling of isolated and accreting NSs, we mainly focus on the recently-constructed Togashi EOS in a variational method. A special feature of the Togashi EOS is that it has small symmetry energy of nuclear matter and prohibits the DU process even with the maximum mass. To introduce another fast cooling process, we consider a pion Urca process operating due to the pion condensation. We find that a new model incorporating the pion condensed with the Togashi EOS (Togashi$+\pi$) generally reproduces the various observational constraints on NS mass and radius. In contrast, other pion condensed EOSs with high symmetry energy do not reproduce the 2 $M_\odot$-mass observations. This is due to the difference of the symmetry energies; Compared with other large symmetry energy EOSs, the Togashi EOS does not become in the high-density regions comparable to the central density.

Using the constructed EOS, we performed cooling calculations for isolated and accreting NSs, focusing on the Togashi EOS. The original Togashi EOS cannot explain the cold observations because the DU process is prohibited, while Togashi$+\pi$ cannot explain almost all observations due to the strong pion Urca process. Furthermore, when the strong neutron superfluid effect is considered, the pion Urca process is highly suppressed, and most cooling observations can be explained. Thus, we find that the low symmetry energy EOSs such as the Togashi EOS become consistent with NS mass, radius, and temperature observations with pion condensation and strong neutron superfluidity. For large symmetry energy EOSs, most cooling observations can be reproduced by the DU process even without the pion condensation because the DU process easily occurs even with low mass NSs.

Finally, we performed X-ray burst calculations with the different symmetry energy or different radius EOSs, using an approximate nuclear reaction network including 88 nuclei. We find that the recurrence time and peak luminosity tend to be higher for the larger-radius EOSs. This is due to the difference of the strength of surface gravity on NSs. On the other hand, the recurrence time and peak luminosity are larger for heavier NSs due to the difference of the strength of neutrino cooling, including the absence or presence of the DU process. Therefore, it can be interpreted that the effects of surface gravity and the neutrino cooling are conflicted with the NS mass relationship of the recurrence time and peak luminosity. We compare our models with the observed burst light curve of GS 1826–24. As a result, large-radius EOSs tend to be rejected because the peak luminosity is so high that a photospheric radius expansion could occur.

In contrast to the recurrence time and peak luminosity, a burst parameter α, which indicates the efficiency of accretion energy against the burst energy, strongly correlates to the surface gravity, not neutrino cooling effects. Thus, α is a powerful observed property for probing the EOS than others. If the α value is higher, heavier p-nuclei should be produced by the nucleosynthesis. We also examine the EOS dependence of final products of nucleosynthesis during X-ray burst. We find that heavier p-nuclei than ^{64}Ge, which is a strong waiting point for the rp process, tends to be synthesized for smaller-radius EOSs.

Contents

Chapter 1

Introduction

In this chapter, we firstly review the current states of understanding the equation of states of neutron stars from theoretical, experimental, and observational points of view. To probe the dense matter equation of state in neutron stars, comparing theoretical models of their thermal evolution with the observed temperature and luminosity is a powerful tool. We also review the modern theories of neutron star cooling and Type-I X-ray burst. Finally, we explain our motivation in this thesis.

1.1 Neutron Stars

1.1.1 Neutron Star Structure

Neutron Stars (NSs) are very dense and directly observable stellar objects in the universe. The typical mass and radius of NSs are $M_{\rm NS} \approx 1.4\ M_\odot$ and $R_{\rm NS} \approx 12$ km, respectively, the latter of which is less than $6{\times}10^4$ times as many as the radius of the Sun ($R_\odot = 696340$ km). Hence, the averaged density of NSs should be more than 10^{12} times as many as that of the Sun. Actually, the central density of NSs reaches around several times of $\rho_{\rm nuc}$, where $\rho_{\rm nuc} = (2-3) \times 10^{14}$ g cm^{-3} is the nuclear saturation density, while that of the Sun is 156 g cm^{-3} [18]. In such an extremely high-density environment, particle interactions in NS matter are governed by nuclear force. The particle interactions in the dense matter are used to construct the nuclear *equation of states* (EOSs), which are specific relations among thermodynamic quantities such as the pressure–density relation. We need the EOS based on theories, experiments, and observations to elucidate the behavior of dense matter in NS.

However, there is no unique theoretical prediction for the EOS for two reasons: One is that it is mathematically hard to describe the multiple-particle interactions in dense matter. The functions of the EOS are initially derived from the underlying microphysical theory of the strong interactions, *quantum chromodynamics* (QCD). Unfortunately, the first-principle calculation in QCD, the so-called lattice Monte Carlo QCD simulation, does not work in high-density regions due to the famous "sign problem". Another attempt based on the QCD to probe the dense matter is perturbative QCD calculation (e.g., Ref. [19]), but this method is reliable only for $\rho \gtrsim 50\ \rho_{\rm nuc}$ [20] because quark-quark interactions become more robust with increasing the point-to-point distance, corresponding to decreasing the density. In the end, the perturbative
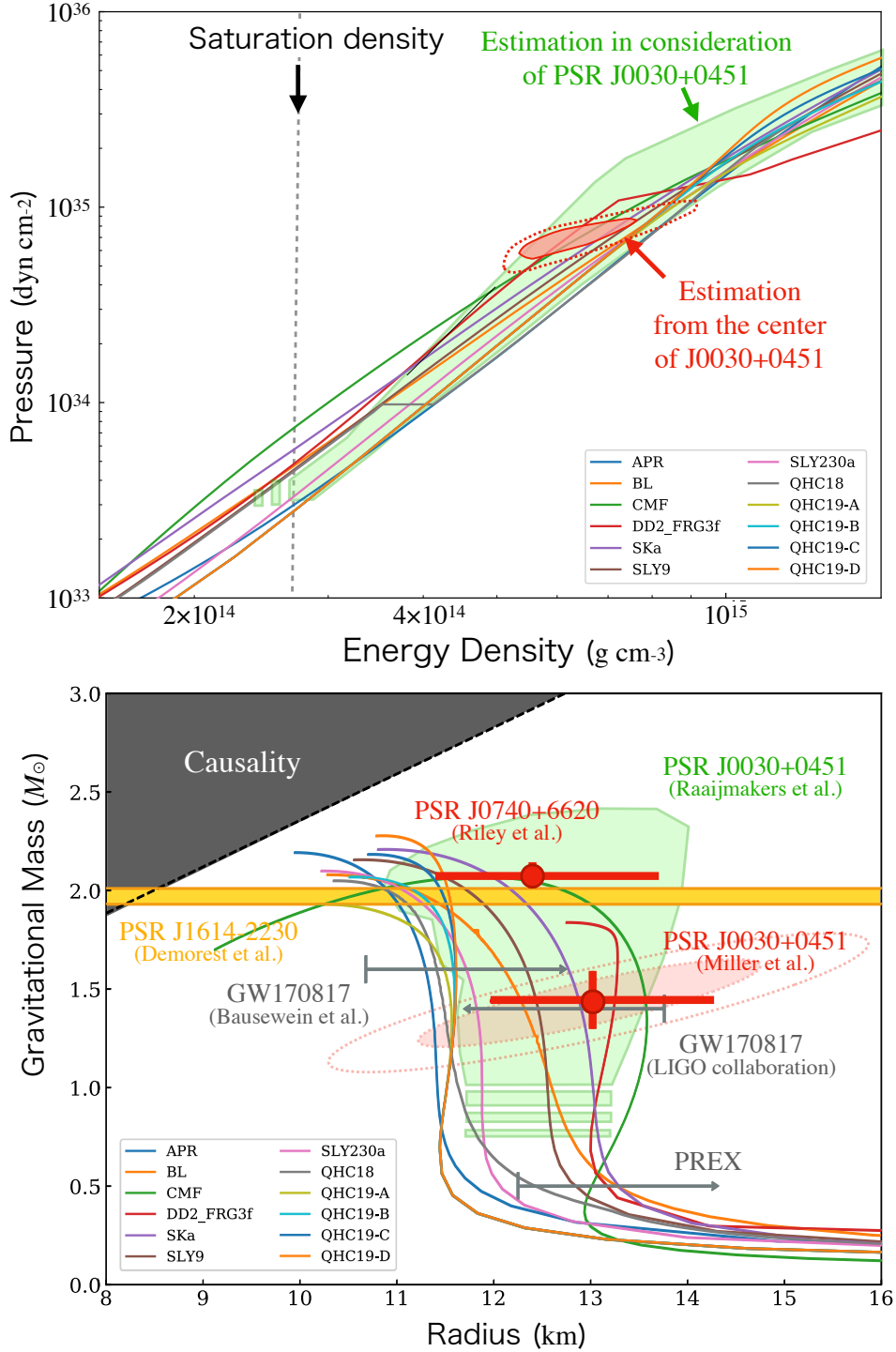
Fig. 1.1: Pressure–density (top) and mass-radius relation (bottom) for cold NSs [1] (courtesy: Prof. Teruaki Enoto and Prof. Nobutoshi Yasutake). The color of curves indicates the EOS corresponding to the left-bottom corner: APR [2], BL [3], CMF [4], DD2_FRG3f [5], SKa [6], SLY9 [6], SLY230a [6], QHC18 [7], and QHC19 A–D [8]. In both panels, red and green regions indicate the observational constraints of PSR J0030+0451 from Ref. [9] and Ref. [10], respectively. Observational constrains from PSR J1614−2230, PSR J0740+6620, and GW 170817 are taken from Ref. [11], Ref. [12], and Refs. [13, 14], respectively. The recent experimental constraints from neutron skin thickness of ^{208}Pb are based on Ref. [15] (for the updated experiment, PREX–II and relating to the controversy, see Refs. [16, 17].)
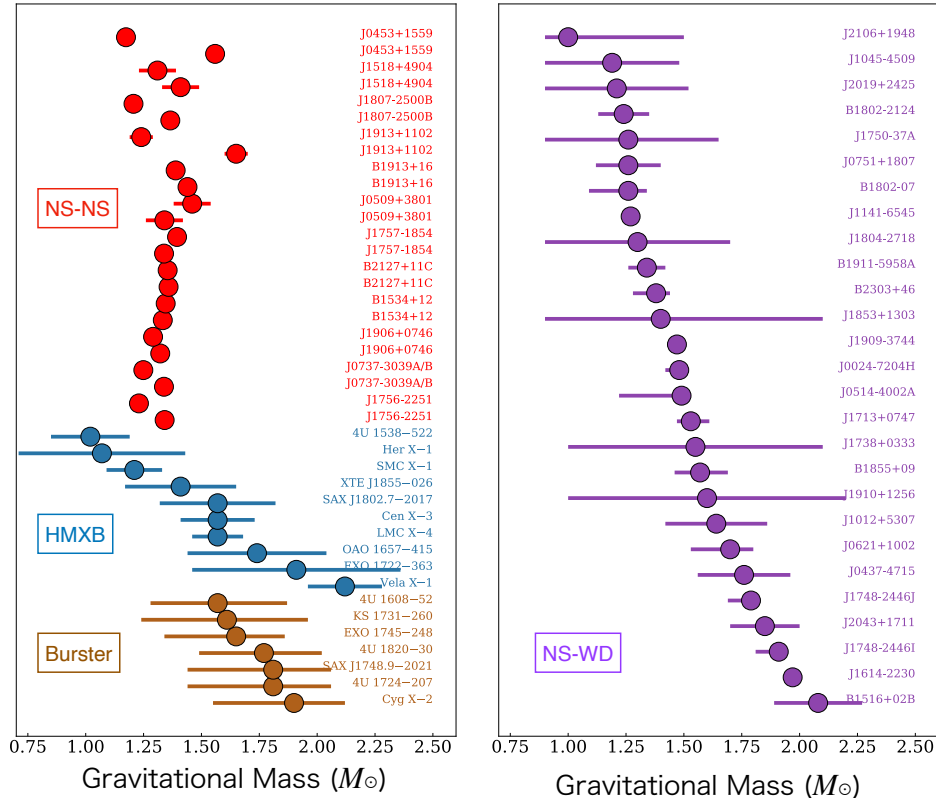
Fig. 1.2: Mass and radius distribution of observed NSs as of 2021 [1] (courtesy: Prof. Teruaki Enoto and Prof. Nobutoshi Yasutake). The system with the NS is as follows: X-ray bursters in low-mass X-ray binaries (brown) [24], NS-NS binaries (red), high-mass X-ray binaries (HMXB) (blue) in the left panel, and NS-WD binaries (purple) in the right panel [25].

method is broken in the relatively low-density regions of NSs. To avoid the difficult problem of QCD, many phenomenological approaches relative to the lattice QCD calculations have been developed and used for the construction of the EOS (for a review, see Ref. [21]).

The other is that high-density ($\rho \gtrsim \rho_{\mathrm{nuc}}$) and (relatively) low-temperature ($T \lesssim 1$ MeV) regions are very hard to be probed through experiments in Earth-based laboratories, although investigations of heavy-ion collisions with large hadron accreralators could be helpful to know the properties of dense and hot nuclear matter (e.g., Ref. [22]). Even with the latest experiment to measure the stiffness of the neutron matter, the investigated density is at most $1.5\rho_{\mathrm{nuc}}$ (SPiRIT [23]). Thus, understanding the EOSs of ultra-dense cold matter solely relies on astrophysical observations of NSs.

The uncertainties of EOSs are reflected in the various observations of NSs. The clearest observable quantities of NSs are the mass and radius, which are directly connected to the pressure–density relation according to general relativity through the Tolman-Oppenheimer-Volkov (TOV) equations as we introduce in Section 2. Fig. 1.1 shows the direct mapping between the pressure-density and mass-radius relations for several EOSs. This unique mapping implies that the observations of NS mass and radius can constrain the properties of dense matter, including the possibilities of exotic matter such as hyperons, deconfined quarks, and kaon condensation. The most crucial observations for the constraints on EOSs are the discovery of massive pulsars whose masses are $M_{\mathrm{NS}} \gtrsim 2M_\odot$ [11, 26, 27]. If the exotic states are considered, the EOS becomes soft.
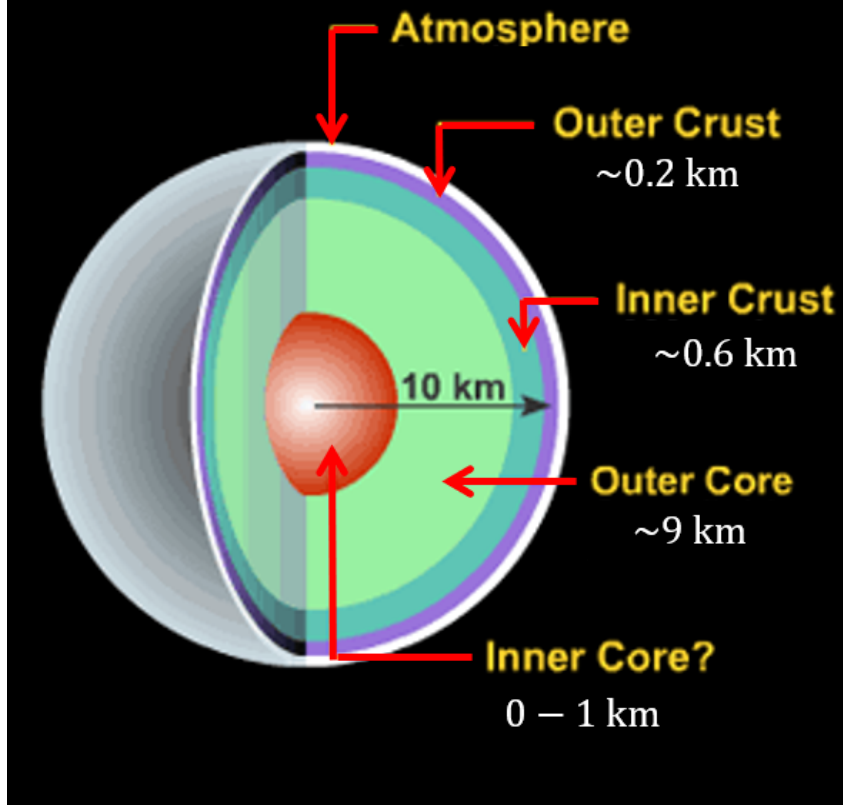
Fig. 1.3: Schematic picture of NS structure [29] (courtesy: Prof. Tsuneo Noda).

Finally, the maximum mass may be highly reduced, though whether to satisfy the constraints of $2\ M_\odot$ observations depend on physical models of particle interactions (for a review, see Ref. [7]). This problem is called the *hyperon puzzle*, regarded as the minimum condition to be satisfied for the construction of exotic-matter EOSs (see Ref. [28]). Fig. 1.2 shows the population of NSs, and there have already been many reliable NS mass data. Compared with the measurements of NS radius as shown in Fig. 1.1, the most direct measurements of NS masses have comprehensively high observational accuracy. Hence, accurate radius measurements will become important in the future and must provide more rigid constraints on pressure-density relations. Several observations to measure the NS radius have already been performed and now succeed in testing the EOSs. We refer to Section 2.2 for the details.

The standard picture of the interior of NSs has been established. We show a schematic picture of the NS structure in Fig. 1.3, where the NS is roughly composed of a thick and massive liquid core (about $0.99\ M_{\rm NS}$ and $0.9\ R_{\rm NS}$) and thin and light solid crust (about $0.01\ M_{\rm NS}$ and $0.1\ R_{\rm NS}$) covered by a thin atmosphere (with ocean). Let us classify the NS structure by dividing it into three layers:

- Atmosphere and Ocean ($\rho \lesssim 10^{10}$ g cm^{-3})

  The atmosphere is a plasma of nuclei and free electrons. Low-density regions ($\rho \lesssim 10^6$ g cm^{-3}) correspond to the atmosphere, which contains light elements such as H and He since the heavier elements should sink to the deeper layers on a concise time scale. In such a regime near the NS surface, the plasma can be partially ionized, which means that nuclei and non-relativistic electrons can be non-ideal gases. The degree of ionization depends

on the low-density EOSs, including temperature, density, and composition information. With increasing density, ions are entirely ionized, and electrons behave as degenerated relativistic ideal gases. Since the free electrons make the compressible negative background, the moving ions can be in any state of gas, liquid, or solid, i.e., Coulomb plasma. This region is sometimes called Ocean. The ocean generally extends to a maximum density of $\rho \sim 10^{10}$ g cm^{-3} where ions are hard to survive due to a neutralization, as we explain in the next paragraph (for a review, see Ref. [30]).

- Crust (10^{10} g cm$^{-3} \lesssim \rho \lesssim (0.3 - 0.5)\,\rho_{\mathrm{nuc}}$)

  The crust is further divided into outer and inner crusts. The outer crust extends from the bottom of the atmosphere to the neutron drip density ($\rho_{\mathrm{drip}} \approx 4.31 \times 10^{11}$ g cm^{-3}), where neutrons begin to drip from nuclei. For $\rho < \rho_{\mathrm{drip}}$, matter consists of relativistic degenerated electrons and ions. In low-density regions close to the atmosphere, the β decay ($n \to p + e^- + \bar{\nu}_e$) is basically active. However, if the density becomes higher, since the Fermi energy of electrons becomes larger enough to exceed the difference of rest mass energy between neutrons and protons of 1.3 MeV, the β decay is blocked. Instead, the inverse-β decay ($p + e^- \to n + \nu_e$) begins to operate. Thus, the nuclei become more neutron-rich, creating free neutrons (neutralization). For $\rho > \rho_{\mathrm{drip}}$ corresponding to the inner crust, matter consists of electrons, neutron-rich nuclei, and free superfluid neutrons with the singlet state. If the density gets close to the crust-core interface, whose density highly depends on the EOS, all nuclei begin to melt, and free particles of electrons, protons, and neutrons appear. It is also suggested that nuclei with non-spherical shapes, i.e., nuclear pasta structure, may appear in such density regions corresponding to the bottom of the crust [31, 32, 33, 34].

- Core ($\rho \gtrsim (0.3 - 0.5)\,\rho_{\mathrm{nuc}}$)

  The core is also subdivided into the outer and inner cores. In such a high-density matter, the symmetry energy of the nuclear matter becomes larger and allows the blocked β decay to occur again. Thus, the outer core is composed of not only neutrons but also protons, electrons, and muons, the last two of which appear due to charge neutrality. Here, we call such a matter with neutrons, protons, electrons, and muons, the standard nuclear matter. In the inner core of the NS, it is the most mysterious and interesting part of NSs; the EOSs are poorly known due to experimental and theoretical difficulties. The central density reaches typically $\rho_{\mathrm{c}} \sim 10^{15}$ g cm^{-3}, depending on the EOS. In such an ultra-high density region, various exotic particles beyond standard nuclear matter could appear because the Fermi energies of each particle become very high enough to make the energetically favorable conditions for exotic particles. Thus, exotic matter such as the hyperons, deconfined quarks, and meson (π, K) condensations may exist in the inner core. Furthermore, we should mention that various states of superfluidity and superconductivity might appear due to the low-temperature environment, such as the triplet neutron superfluidity, singlet proton superconductivity, singlet hyperon superfluidity, and quark color-superconductivity [35].

As I introduced above, measurements of NS mass and radius are useful for probing the

complicated NS structure, but the extracted information is the only pressure-density relation. In other words, we cannot pin down the states of matter inside NSs, including exotic ones. On the other hand, the observed temperature and/or luminosity give clues to clarify the complicated NS structure because particle reactions inside NSs, which affect the temperature and luminosity, are peculiar to each state of matter. Hence, X-ray observations during thermal evolution of NSs could give more substantial constraints, including the composition.

1.1.2   Cooling of Isolated Neutron Stars

A neutron star is born just after supernova explosion of a massive progenitor with a mass less than around $20M_\odot$. After that, it is believed that the hot NS cools down due to losses of neutrinos and photons. For the age of $t \lesssim 10^5$ yrs after the formation of NSs, the cooling behavior is dominated by the losses of neutrinos because of the discussions of their long mean free path as below (based on Ref. [36]).

Here, we consider the charged and neural current weak interactions in Weinberg-Salam-Glashow (WSG) theory, and cold NSs with less than around 10^9 K. For the charged-current interaction, the important interaction for neutrino energy loss is the electron scattering, whose cross section is

$$\sigma_e \simeq 1.06 \times 10^{-45} \left(\frac{E_\nu}{0.511 \text{ keV}} \right)^2 \frac{E_\nu}{E_\text{F}} \text{ cm}^2 , \tag{1.1}$$

where E_ν is the neutrino energy and E_F is the Fermi energy of electrons. Then, the mean free path of electron-type neutrinos is calculated to be

$$\lambda_e = \frac{1}{\sigma_e n_e} \sim 1.5 \times 10^8 \left(\frac{\rho_\text{nuc}}{\rho_\text{B}} \right)^{4/3} \left(\frac{0.1 \text{ MeV}}{E_\nu} \right)^3 \text{ km} , \tag{1.2}$$

where n_e and ρ_B denote electron number density and baryon density, respectively. For the neural-current interactions, on the other hand, elastic scattering between lepton-neutrinos and neutrons is valid and could reduce λ_e effectively. The cross section for the elastic scattering off neutrons is

$$\sigma_n \simeq 4.40 \times 10^{-45} \left(\frac{E_\nu}{0.511 \text{ keV}} \right)^2 \text{ cm}^2 . \tag{1.3}$$

The corresponding mean free path of neutrinos is calculated to be

$$\lambda_n = \frac{1}{\sigma_n n_n} \simeq 3.0 \times 10^2 \frac{\rho_\text{nuc}}{\rho_\text{B}} \left(\frac{0.1 \text{ MeV}}{E_\nu} \right)^2 \text{ km} , \tag{1.4}$$

where n_n denotes neutron number density. Considering that neutrinos continuously encounter neutrons and electrons, the averaged mean free path should be considered in not simple arithmetic average but geometric one, just like the case of the averaged energy loss due to multiple inelastic collisions between particles. Thus, the *effective* mean free path for neutrinos inside cold

NSs is estimated to be

$$\lambda_{\mathrm{eff}} \simeq \sqrt{\lambda_e \lambda_n} = 2 \times 10^5 \ \mathrm{km} \left(\frac{\rho_{\mathrm{nuc}}}{\rho_{\mathrm{B}}}\right)^{7/6} \left(\frac{0.1 \ \mathrm{MeV}}{E_\nu}\right)^{5/2} . \tag{1.5}$$

Note that neutrino energy can be regarded as the thermal energy $k_{\mathrm{B}}T$ for $T \lesssim 1$ MeV (e.g., Ref. [37]). With decreasing the temperature of $T \lesssim 0.1$ MeV, therefore, such a cold NS becomes transparent to neutrinos, i.e., $\lambda_{\mathrm{eff}} \gg R_{\mathrm{NS}}$. Thus, once neutrinos are produced inside NSs, they escape from the stars freely.

Many kinds of neutrino emissions processes are thought to occur in NSs. In modern cooling theory, they are classified into two categories, i.e., minimal (slow) and fast cooling scenarios. All neutrino cooling processes always operate under the former scenario, while they are not always open in the latter. We introduce the detailed mechanisms of neutrino emissions processes, including nucleon superfluidity.

1.1.3 Minimal Cooling Scenario

In the neutrino cooling era, the thermal energy of NSs is lost from the crust and core due to neutrino emissions. In the crust, we consider the following neutrino cooling processes:

- Cooling Processes in the Crust

  - Electron-ion bremsstrahlung [38, 39]:

    $$e + (A, Z) \rightarrow e + (A, Z) + \nu + \bar{\nu} , \tag{1.6}$$

    where (A, Z) stands for an atomic nucleus with an atomic number Z and mass number A.

  - Electron synchrotron [40]:

    $$e \xrightarrow{B} e + \nu + \bar{\nu} , \tag{1.7}$$

    where the symbol B indicates that this process works in the presence of the magnetic field.

  - Electron-positron pair creation [41]:

    $$e + e^+ \rightarrow \nu + \bar{\nu} . \tag{1.8}$$

  - Photo-neutrino process [42, 41]:

    $$e + \gamma \rightarrow e + \nu + \bar{\nu} , \tag{1.9}$$

    where γ stands for a plasmon or photon.

  - Plasmon decay process [41]:

    $$\gamma \rightarrow \nu + \bar{\nu} . \tag{1.10}$$

13

– Neutrons-neutrons bremsstrahlung

$$n + n \rightarrow n + n + \nu + \bar{\nu}. \tag{1.11}$$

– Pair and Breaking Formation (PBF) process with singlet neutrons

$$n + n \rightarrow [nn] + \nu + \bar{\nu}, \tag{1.12}$$

where $[nn]$ denotes the cooper pair of neutrons with a singlet state and behaves like a boson. This process operates for $T \lesssim T_{\mathrm{cr}}$ where T_{cr} is the superfluid transition temperature, which is explained later.

For the reactions of (1.6)–(1.11), the dominant cooling processes in cold NSs without the magnetic field are the electron-nucleus and neutron-neutron bremsstrahlung in the crust [43]. Although the electron-positron pair creation, photo-neutrino process, and plasmon decay process also contribute to cooling curves as the temperature increases around $T \gtrsim 10^9$ K [44], the interior temperature of observed most NSs is estimated to be $T \lesssim 10^9$ K according to the simple isothermal models of $T \simeq 20\ T_{\mathrm{s}}$ [45], with the use of their observed surface temperature $T_{\mathrm{s}} \sim 10^6$ K. Thus, the only electron-nucleus and neutron-neutron bremsstrahlung are the most important in the crust. However, they are much weaker than cooling processes occurring in the core, which we introduce below.

The emissivity of electron-nucleus bremsstrahlung is expressed [46]

$$\epsilon_\nu^{\mathrm{eN}} = 8.6 \times 10^{19} \left(\frac{\rho_{\mathrm{B}}}{\rho_{\mathrm{nuc}}} \right) Z Y_e T_9^6 L \ \mathrm{erg\ s^{-1}\ cm^{-3}} \ , \tag{1.13}$$

where Y_e is the electron fraction, and T_9 is the temperature in units of 10^9 K. $L \sim 1$ is a dimensionless function that depends on the phases in the crust [39]. The emissivity of neutron-neutron bremsstrahlung is calculated [47]

$$\epsilon_\nu^{\mathrm{nn}} = 7.3 \times 10^{19} \left(\frac{m_n^*}{m_n} \right)^4 \left(\frac{\rho_{\mathrm{B}}}{\rho_{\mathrm{nuc}}} \right)^{1/3} Y_n^{1/3} T_9^8 \ \mathrm{erg\ s^{-1}\ cm^{-3}}, \tag{1.14}$$

where Y_n is the neutron fraction. m_n and m_n^* denote the static and effective neutron masses and depends on the EOS, especially important for the effects of three-body forces.

Since neutrons degenerate and the internal temperature is quite lower than the Fermi temperature ($T_{\mathrm{F}} \sim 10^{11}$ K), nucleon could be in superfluid and superconductive states according to the BCS theory [49]; In such cold environment, if the temperature is lower than the superfluid transition temperature T_{cr}, nucleons could make the (Cooper) pair because the system is more energetically favorable than the unpaired states. Fig. 1.4 shows density dependence of phase shifts for nucleon-nucleon scattering. As we see, the nucleons with singlet ($^1\mathrm{S}_0$) states appear in low-density regions due to the attractive force which corresponds to the nucleon pairing. In fact, neutrons $^1\mathrm{S}_0$ channels are known to appear in the inner crust while protons $^1\mathrm{S}_0$ channels are known to appear in the core. Meanwhile, neutron triplet ($^3\mathrm{P}_2$) state is expected to appear in high-density regions $\gtrsim \rho_{\mathrm{nuc}}$. When the
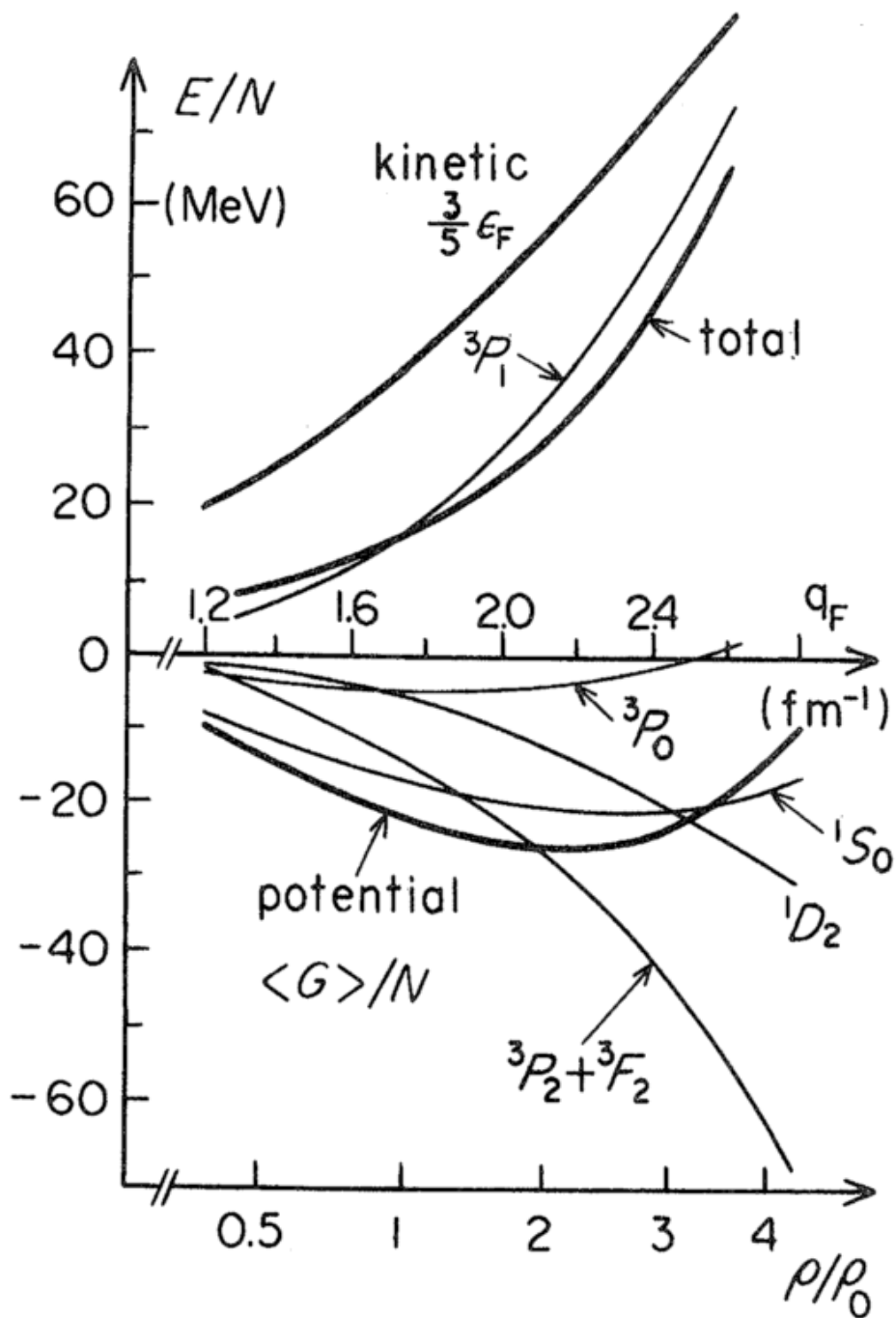
Fig. 1.4: Neutron Matter energy for the partial wave contribution per a nucleon in the normal state v.s. neutron Fermi number density (middle axis) or normalzied density by the saturaion density [48] (taken from Ref. [29], courtesy: Prof. Tsuneo Noda).
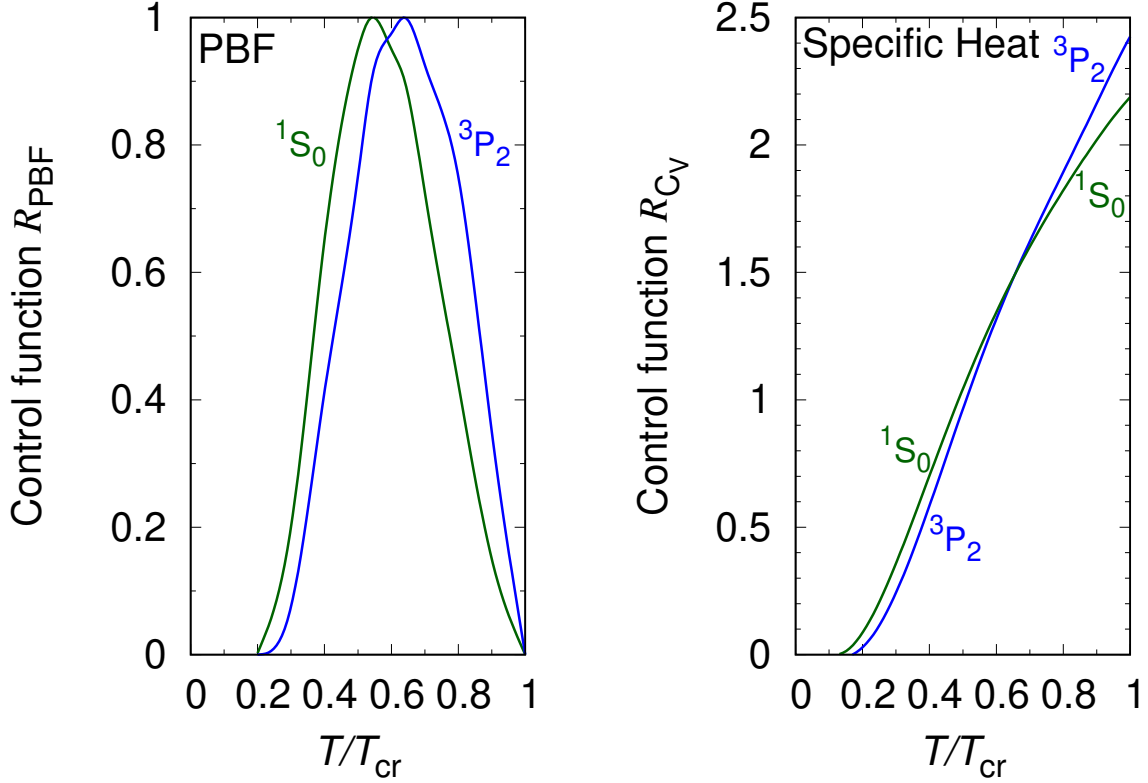
Fig. 1.5: Control functions (efficiency as a function of $T/T_{\rm cr}$) of the PBF process (Left) and specific heat (Right) for singlet and triplet nucleons, respectively.

neutrons in the crust transit into a $^1{\rm S}_0$ superfluid state due to the neutrino cooling, the release of the latent heat, called the PBF process, occurs as seen in the reaction of (1.12). The emissivity of the PBF process of neutrons $^1{\rm S}_0$ channels is given in Ref. [50].

$$\epsilon_\nu^{n\ ^1{\rm S}_0} = 1.0 \times 10^{22} \left(\frac{m_n^*}{m_n}\right) \left(\frac{\rho_{\rm B}}{\rho_{\rm nuc}}\right)^{1/3} Y_n^{1/3} R_{{\rm PBF},s} \left(\frac{T_{\rm cr}}{T}\right) T_9^7 \ {\rm erg\ s^{-1}\ cm^{-3}}, \qquad (1.15)$$

where $R_{{\rm PBF},s}$ is the control function of the singlet-state nucleons which indicates the efficiency of the PBF process as a function of $T/T_{\rm cr}$. Left panel of Fig. 1.5 shows the temperature dependence of $R_{\rm PBF}$. As we see, the PBF processes take a maximum value at $T \simeq 0.5T_{\rm cr}$ and mimimum value of zero for $T \lesssim 0.2\ T_{\rm cr}$.

- Cooling Processes in the Core

  - Nucleon-nucleon bremsstrahlung

$$b + b' \rightarrow b + b' + \nu + \bar{\nu}, \qquad (1.16)$$

where b and b' denote baryons $(n, p, \Lambda, \Sigma, \Xi, \Omega)$, respectively. In the core, since the free protons are created due to the nuclear symmetry energy, neutron-protons and protons-protons bremsstrahlung also work in addition to neutron-neutron bremsstrahlung as shown in the reaction of (1.11), whose emissivity is the same as Eq. (1.14). The

emissivities of neutron-protons and protons-protons bremsstrahlung are written as follows [47]

$$\epsilon_\nu^{\text{np}} = 3.1 \times 10^{20} \left(\frac{m_n^*}{m_n}\right)^2 \left(\frac{m_p^*}{m_p}\right)^2 \left(\frac{\rho_\text{B}}{\rho_\text{nuc}}\right)^{1/3} Y_p^{1/3} T_9^8 \text{ erg s}^{-1} \text{ cm}^{-3}, \quad (1.17)$$

$$\epsilon_\nu^{\text{pp}} = 1.7 \times 10^{19} \left(\frac{m_p^*}{m_p}\right)^4 \left(\frac{\rho_\text{B}}{\rho_\text{nuc}}\right)^{1/3} Y_p^{1/3} T_9^8 \text{ erg s}^{-1} \text{ cm}^{-3}, \quad (1.18)$$

where Y_p is the proton fraction. m_p and m_p^* denote the static and effective proton masses. It should be emphasized that both processes always occur.

– Modified Urca processes

$$
\begin{aligned}
n + b &\rightarrow p + b + l + \bar{\nu}, \\
p + b + l &\rightarrow n + b + l + \nu,
\end{aligned}
\quad (1.19)
$$

where l is the lepton (e, μ). It should be noted that the modified Urca process does not basically work in the crust where the symmetry energy is low enough not to create free protons. The emissivities of modified Urca processes with neutron and proton branches are calculated, respectively [47]:

$$
\begin{aligned}
\epsilon_\nu^{\text{n}} = {} & 5.81 \times 10^{21} \left(\frac{m_n^*}{m_n}\right)^3 \left(\frac{m_p^*}{m_p}\right) \left(\frac{\rho_\text{B}}{\rho_\text{nuc}}\right)^{1/3} \left(Y_e^{1/3} + Y_\mu^{1/3}\right) \\
& \times \left(1.76 - 0.63 \left(\frac{\rho_\text{nuc}}{\rho_\text{B}}\right)^2\right) T_9^8 \text{ erg s}^{-1} \text{ cm}^{-3}, \quad (1.20)
\end{aligned}
$$

$$
\begin{aligned}
\epsilon_\nu^{\text{p}} = {} & 5.81 \times 10^{21} \left(\frac{m_n^*}{m_n}\right) \left(\frac{m_p^*}{m_p}\right)^3 \left(\frac{\rho_\text{B}}{\rho_\text{nuc}}\right)^{1/3} \left(Y_e^{1/3} + Y_\mu^{1/3}\right) \\
& \times \left[1 - \left(\frac{Y_e}{4Y_p}\right)^{1/3}\right] \left(1.76 - 0.63 \left(\frac{\rho_\text{nuc}}{\rho_\text{B}}\right)^2\right) T_9^8 \text{ erg s}^{-1} \text{ cm}^{-3}. \quad (1.21)
\end{aligned}
$$

The modified Urca process always operates for the neutron branch while it occurs for the proton branch only if $Y_p > 1/65$ because of the momentum conversation. Focusing on the coefficients of neutrino emissivities, the modified Urca process is stronger by 1–2 orders of magnitude than the bremsstrahlung processes in the core. Thus, the modified Urca (core) and bremsstrahlung processes (core+crust) are dominant for the thermal evolution of NSs under the slow cooling scenario.

– PBF process with singlet protons and triplet neutrons

$$b + b \rightarrow [bb] + \nu + \bar{\nu}, \quad (1.22)$$

In the core regions, neutrons and protons are expected to become the superfluid state with ${}^3\text{P}_2$ channel and the superconductive state with ${}^1\text{S}_0$ channel, respectively, as we see in Fig. 1.4. Hence, their PBF processes should occur if $T < T_\text{cr}$ and their
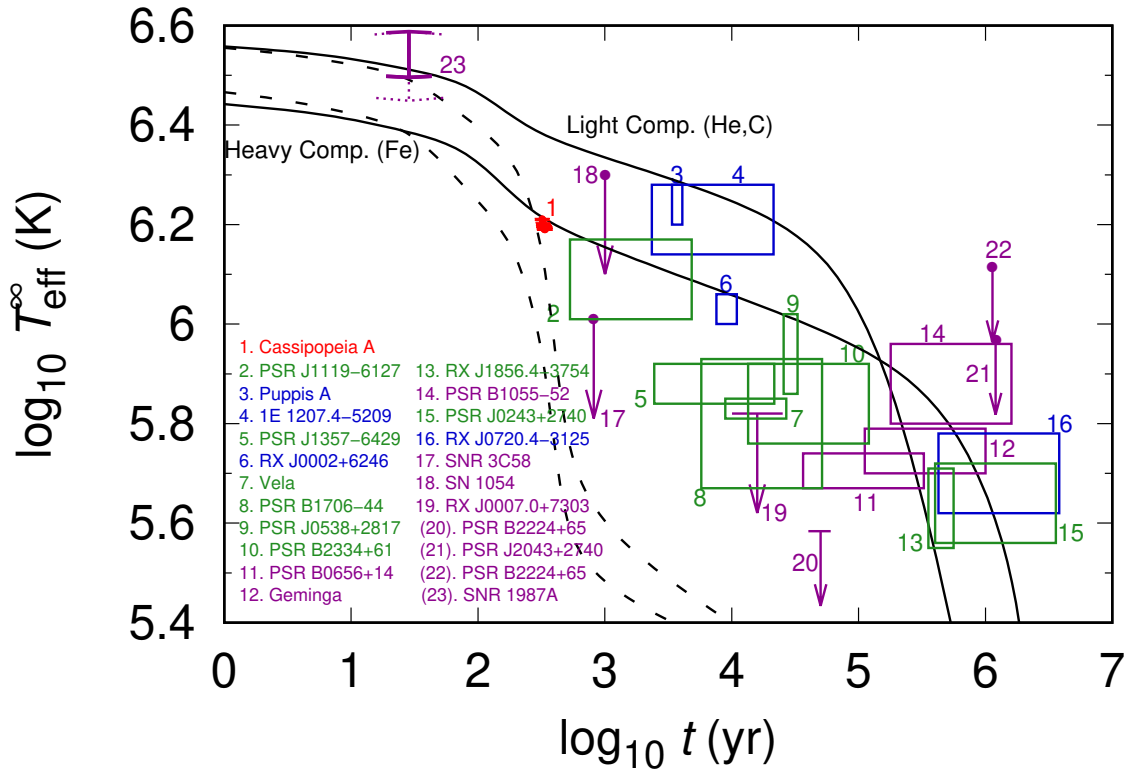
17

Fig. 1.6: Observed age and effetcive temperature of isolated NSs. Solid curves show examples of standrad cooling models with heavy (Fe) and light (He, C) surface compositions. Dotted curves show typical fast cooling models where the nucleon Direct Urca process operates.

emissivities are given in [50, 51] (see also Ref. [52])

$$\epsilon_\nu^{n\ ^3P_2} = 8.6 \times 10^{21} \left(\frac{m_n^*}{m_n}\right) \left(\frac{\rho_B}{\rho_{nuc}}\right)^{1/3} Y_n^{1/3} R_{PBF,t} \left(\frac{T_{cr}}{T}\right) T_9^7 , \qquad (1.23)$$

$$\epsilon_\nu^{p\ ^1S_0} = 2.6 \times 10^{22} \left(\frac{m_p^*}{m_p}\right) \left(\frac{\rho_B}{\rho_{nuc}}\right)^{1/3} Y_p^{1/3} R_{PBF,s} \left(\frac{T_{cr}}{T}\right) T_9^7 , \qquad (1.24)$$

where $R_{PBF,s}$ and $R_{PBF,t}$ denote control functions of the singlet and triple states nucleons, respectively, whose temperature dependences are shown in Fig. 1.5. Focusing on the coefficients of the emissivities, the PBF process is comparable with the modified Urca process and bremsstrahlung. Hence, the effects of nucleon superfluidity on cooling curves are very large, depending on the density dependence of T_{cr}.

Fig. 1.6 shows the age and surface temperature of isolated NSs observed so far (we call them cooling observations). We can probe the NS physics, such as the EOS, by comparing the models with cooling observations. A scenario that includes the only *conventional* slow cooling processes (modified Urca process and bremsstrahlung) and PBF processes due to the nucleon superfluidity is often called *minimal cooling scenario*, where any fast cooling process is absent [51, 53]. The minimal cooling scenario can explain most isolated NSs observations by changing model parameters. Thus, the minimal cooling scenario is widely regarded as the standard cooling model.

18

1.1.4 Fast Cooling Processes

The minimal cooling scenario has been a successful cooling theory. However, some observed NSs are too cold to be clearly explained by the minimal cooling scenario. For example, focusing on cooling observations of isolated NSs as shown in Fig. 1.6, Vela, PSR J0205+6449 in supernova remnant 3C58 and RX J0007.0+7302 are known to be too cold for their young ages. Other compact objects, such as G127.1+0.5, G084.2+0.8, G074.0−8.5, G065.3+5.79, and G043.3−0.210 are extraordinary cold from X-ray observations, although they have not been identified yet (see also Figure 11 in Ref. [44]). To reproduce such cold cooling observations, fast cooling processes are necessary.

The most powerful candidate for fast cooling processes is the nucleon direct Urca (DU) process, as we explain below. Furthermore, if we consider some states of exotic matter in NSs, other rapid cooling processes beyond the DU process may occur, such as exotic cooling processes with hyperons, deconfined quarks, and meson condensations [54]. In this thesis, we introduce the nucleon DU and pion Urca processes due to pion condensation, which do not implicitly contain s quarks, unlike other exotic cooling processes.

- Nucleon direct Urca (DU) process

$$
\begin{aligned}
n &\rightarrow p + l + \bar{\nu}, \\
p + l &\rightarrow n + l + \nu.
\end{aligned}
\tag{1.25}
$$

This process is the neutrino emission due to the just β decay and inverse β decay. The neutrino emissivity of the DU process is obtained [55]:

$$
\epsilon_\nu^{\mathrm{DU}} = 4.00 \times 10^{27} \left(\frac{m_n^*}{m_n}\right) \left(\frac{m_p^*}{m_p}\right) \left(\frac{n_{\mathrm{B}}}{n_0}\right)^{2/3} T_9^6 \left(\sum_{l=e,\mu} Y_l^{1/3} \Theta_{npl}\right) \quad \mathrm{erg\ cm^{-3}\ s^{-1}} \ , \tag{1.26}
$$

where Θ_{npl} is the step function satisfying

$$
\Theta_{npl} = \Theta(\boldsymbol{k}_n - \boldsymbol{k}_p - \boldsymbol{k}_l) = \begin{cases} 1 & \text{if } |\boldsymbol{k}_n - \boldsymbol{k}_p| \geq |\boldsymbol{k}_l| \\ 0 & \text{otherwise} \ , \end{cases}
\tag{1.27}
$$

where $\boldsymbol{k}_i$ is the Fermi wave number of i particles. Compared with the standard cooling processes including the modified Urca , bremsstrahlung, and the PBF processes, the DU process is stronger by around seven orders of magnitude around a typical NS temperature of $T_9 \sim 0.3$ [56]. Once the DU process is open, it decreases the temperature in the core rapidly as we see in Fig. 1.6. However, the DU process is forbidden to occur if the momentum among reactant particles is not conserved in conventional NS matter. Namely, the DU process does not occur unless the momemtum conversation $\boldsymbol{k}_n - \boldsymbol{k}_p = \boldsymbol{k}_l$ is satisfied. From the triangle condition of $|\boldsymbol{k}_n| \leq |\boldsymbol{k}_p + \boldsymbol{k}_l|$, charge neutrality $Y_p = Y_e + Y_\mu$ and baryon number conversation $Y_n + Y_p = 1$, one can obtain the threshold proton fraction $Y_p^{e\mathrm{DU}}$ and

$Y_p^{\mu\mathrm{DU}}$ for the DU process via electrons and muons, respectively [55]:

$$Y_p \geq Y_p^{e\mathrm{DU}} = \begin{cases} 1/9 & \text{if } Y_\mu = 0 \\ 0.1477 & \text{if } Y_\mu = Y_e \\ \left\{1 + \left(1 + x_e^{1/3}\right)^3\right\}^{-1} & \text{otherwise} \end{cases} \tag{1.28}$$

$$Y_p \geq Y_p^{\mu\mathrm{DU}} = \begin{cases} 0.1477 & \text{if } Y_\mu = Y_e \\ \left\{1 + \left(1 + x_\mu^{1/3}\right)^3\right\}^{-1} & Y_\mu > 0 \end{cases} \tag{1.29}$$

where $x_e = Y_e/(Y_e + Y_\mu)$ and $x_\mu = Y_\mu/(Y_e + Y_\mu)$. The important condition is Eq. (1.28) because below $Y_p < Y_p^{e\mathrm{DU}}$, the only slow cooling processes operates. It is also important that the DU (and slow) cooling processes are suppressed by copper pairing due to the nucleon superfluidity, and their emissivities decrease in proportional to T/T_{cr} for $T \gtrsim 0.2\, T_{\mathrm{cr}}$ and to $\exp(-T_{\mathrm{cr}}/T)$ for $T \lesssim 0.2\, T_{\mathrm{cr}}$. We note that the specific capacity of NSs is also suppressed similarity as shown in the right panel of Fig. 1.5 (based on Ref. [57]), which indirectly ehnahces the cooling effects of the DU process because the cooling rate is higher by not only the neutrino cooling but also the reduction of the specific capacity.

- Pion Urca Process

$$\begin{aligned} \pi^- + n &\rightarrow n + l^- + \bar{\nu}_l, \\ n + l^- &\rightarrow \pi^- + n + \nu_l, \\ \eta(\boldsymbol{p}) &\rightarrow \eta(\boldsymbol{p'}) + l + \bar{\nu}_l, \\ \eta(\boldsymbol{p}) + l &\rightarrow \eta(\boldsymbol{p'}) + \nu_l \end{aligned} \tag{1.30}$$

where η denotes a quasi-nucleon appearing due to the pion condensation, $\boldsymbol{p}$ and $\boldsymbol{p'}$ denote momentum of η particles. Here, we take the pion condensation modeled by Ref. [58] where two phases of pure charged pion (π^c) condensation and neutral–charged pions (π^0–π^c) condensation are included.

The possibility of pion condensation in the dense matter and NS core has been discussed for decades (for review, see Refs. [60, 61]). In this idea, the pion condensation is induced by the coherent ground states with the same quantum number, spin, and isospin, i.e., Alternating-Layer-Spin (ALS) structure [62]. If the pion condensation occurs, charged pions appear and may contribute to the pion Urca process (first two reactions in (1.30)). It is also considered that the momentum of quasi-particles becomes large enough to cause the DU process by pion condensation (last two reactions in (1.30)). The emissivities of the pion Urca process are shown in Fig. 1.7. As we see, they are roughly $\epsilon_\nu \approx 10^{25} T_9^6$ erg cm^{-3} s^{-1}, which is much higher than slow cooling processes. Furthermore, the pion Urca process occurs at a relatively low density $\rho_{\mathrm{B}} \simeq 4.3 \times 10^{14}$ g cm^{-3} for $\tilde{g}' = 0.5$. This implies that even low-mass NSs cool rapidly, although the critical mass naturally depends on the EOS. In some EOSs with low symmetry energy, since the DU process is prohibited, the pion Urca process could be a candidate to explain cold NSs.
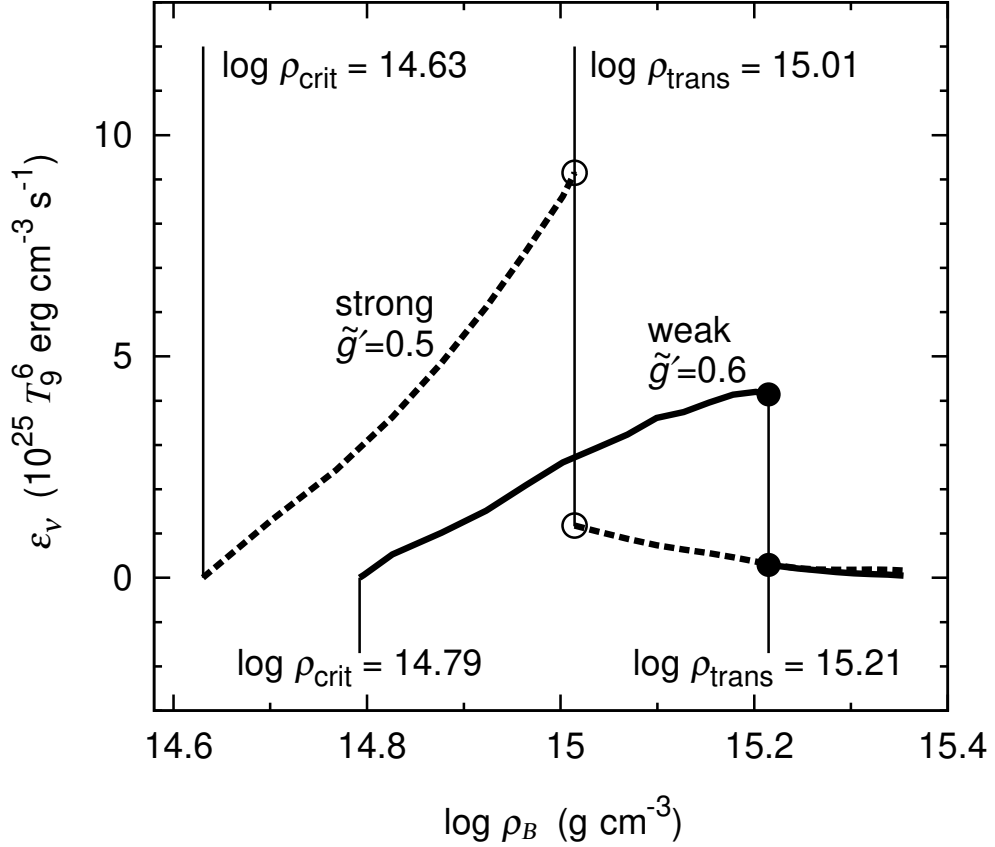
Fig. 1.7: Baryon-density dependence of neutrino emissivities of pion Urca process for the Landau Migdal parameter $\tilde{g}' = 0.5$ and 0.6, which indicates the strength of pion condensation. ρ_{crit} stand for the critical density between normal and pure π^c states, while ρ_{trans} between pure π^c and mixed π^0–π^c states [59] (courtesy: Dr. Yasuhide Matsuo).

1.2   Accreting Neutron Stars

1.2.1   Low-Mass X-ray binaries

Most NSs observed so far form binary systems in which the main sequence or evolved star accompanies them. Because of the strong gravity, matter falls onto the NS from the companion star through the accretion disk. The binary with NS is classified into two types, i.e., high-mass X-ray binary (HMXB) and low-mass X-ray binary (LMXB). HMXBs are young systems with the age of $t \lesssim 10$ Myr and strong magnetic field $B \approx 10^{12-14}$ G. The companion star is typically heavier than about 10 $M_\odot$, and steller wind works as the accretion mechanism. The NS in HMXBs emits the pulse associated with its spin, which is non-thermal emissions. On the other hand, LMXBs are an ancient system with $t \gtrsim 1$ Gyr, and $B \lesssim 10^{12}$ G, which is the value of typical pulsars. The companion star's mass is less than 1 $M_\odot$, which is thought to be evidence to be stripped by the NS, resulting in the mass loss for long years. The accretion mechanism is a Roche-lobe overflow, which forms the accretion disk around the NS, as shown in
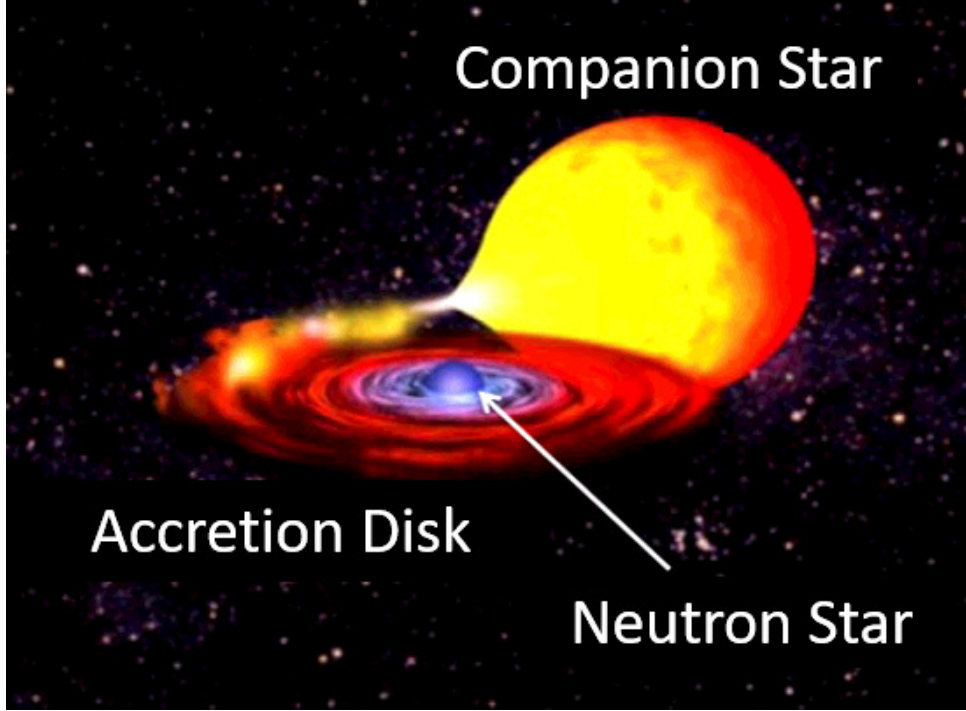
Fig. 1.8: Schematic picture of LMXB (taken from Ref. [63], courtesy: Dr. Yasuhide Matsuo).

Fig. 1.8. Currently, more than 200 LMXBs have been observed as X-ray sources [64]. The X-ray spectrum emitted from the accretion disk and NS surface has been observed in LMXBs. Since the X-ray radiation emitted at the NS surface is the thermal emission, we could also extract the information about interior NSs from the observations of LMXBs.

1.2.2 X-ray Outburst and the Quiescent States

According to X-ray observations, the luminosity is periodically changed in the range from minutes to hundreds of days. We show a typical light curve of LMXBs in Fig. 1.9. In LMXBs, there are two kinds of epochs, i.e., short outbursts and long quiescent phases. In the outburst phase, the X-ray luminosity of NSs varies in a wide range of $L_X \sim 10^{35-38}$ erg s^{-1}. The original energy source is gravitational energy release. The observed luminosity can be explained by thermal emissions emitted not at the NS surface but from the accretion disk. Thus, the X-ray luminosity is regarded as the accreting luminosity

$$L_X \approx \frac{GM_{\mathrm{NS}}}{R_{\mathrm{NS}}\sqrt{1 - 2GM_{\mathrm{NS}}/c^2 R_{\mathrm{NS}}}} \cdot \dot{M} \;. \tag{1.31}$$

Thus, the accretion rate in the outburst phase can be obtained as the observational amount, assuming the NS mass M_{NS} and radius R_{NS}.

In the quiescent phase, on the other hand, mass accretion from the companion star is reduced considerably, and gravitational energy is not released. Then, only thermal emissions at the NS surface are observed, and the quiescent luminosity is the observational quantity. The primary energy source in the quiescent state is the heating in the NS crust, which is the energy released due to the transformation of accreted matter into heavier nuclei in some exothermal reactions.
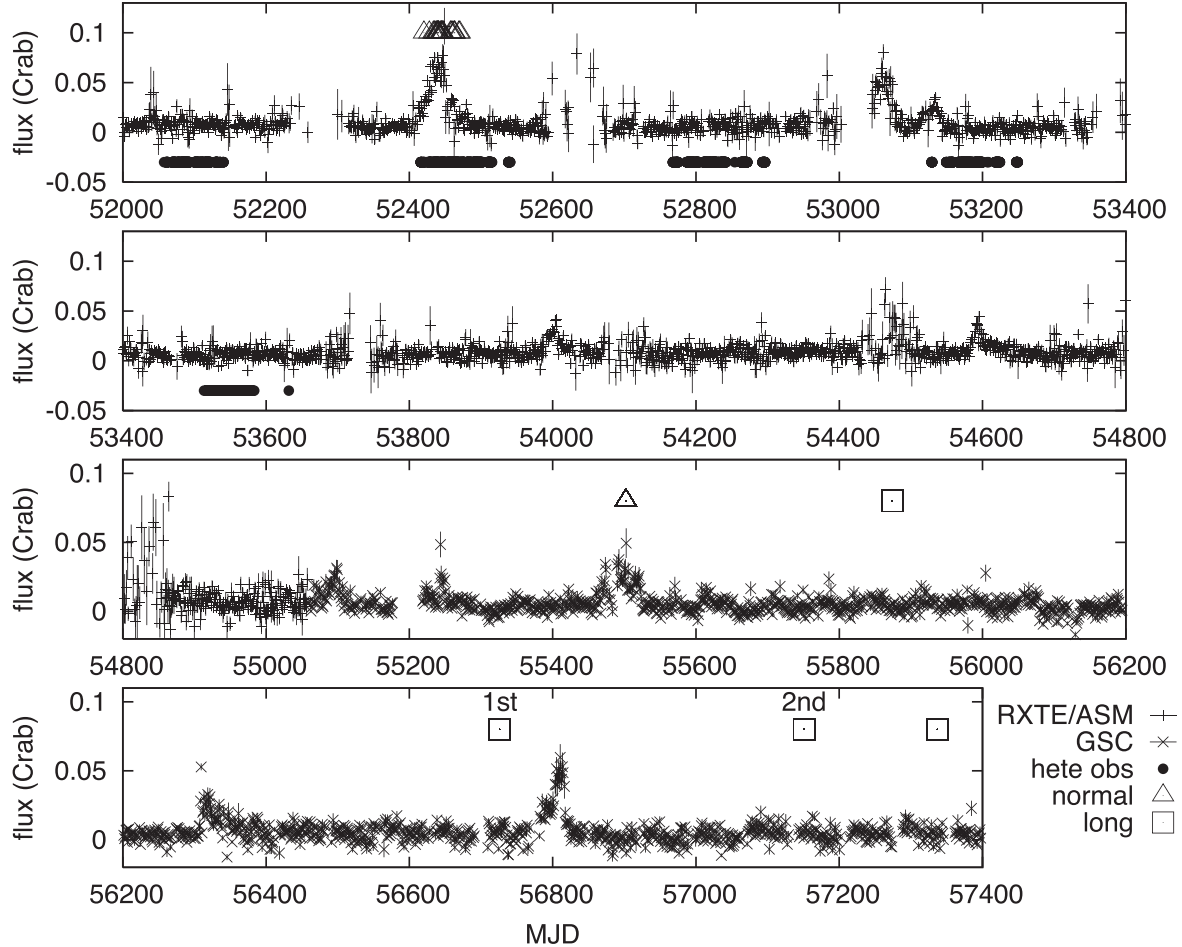
Fig. 1.9: The observations of accreting NS, 4U 1850–086 in more than 10 years [65] (courtesy: Prof. Wataru Iwakiri). The persistent fluxes observed in X-ray satellites RXTE/ASM (plus) and Monitor of All-sky X-ray Image, MAXI/GSC (cross) are plotted. The circle shows the period when the source was viewed by a Wide X-ray monitor loaded onto High-Energy Transient Explore-2 (HETE-2). The triangles and squares show the time of Type-I X-ray bursts with short and long durations, respectively. Note that the X-ray bursts considered in our studies fall within the former case.

These reactions heat the NS crust, reflected in observable thermal emission in quiescent phases. Therefore, such a crustal heating process is essential for the thermal evolution of NSs, but its heating rate has large uncertainties in theory (e.g., Refs. [69, 70]).

Theoretically, the quiescent luminosity is calculated with the condition of the thermal luminosity in steady-state without compressional heating, where the crustal heating is balanced with the neutrino and photon cooling for old NSs; In the neutrino cooling era, since the neutrino (and photon) luminosities highly depend on the temperature of NSs, the crustal heating is negligible because it is independent of temperature. However, if NSs become old and the temperature decreases, the crustal heating contributes to the observed luminosity according to the accretion rate, and finally, the time derivative of the temperature becomes zero as follows

$$\frac{dT}{dt} = \frac{L_{ch} - L_\nu - L_\gamma}{C_V} \, , \tag{1.32}$$
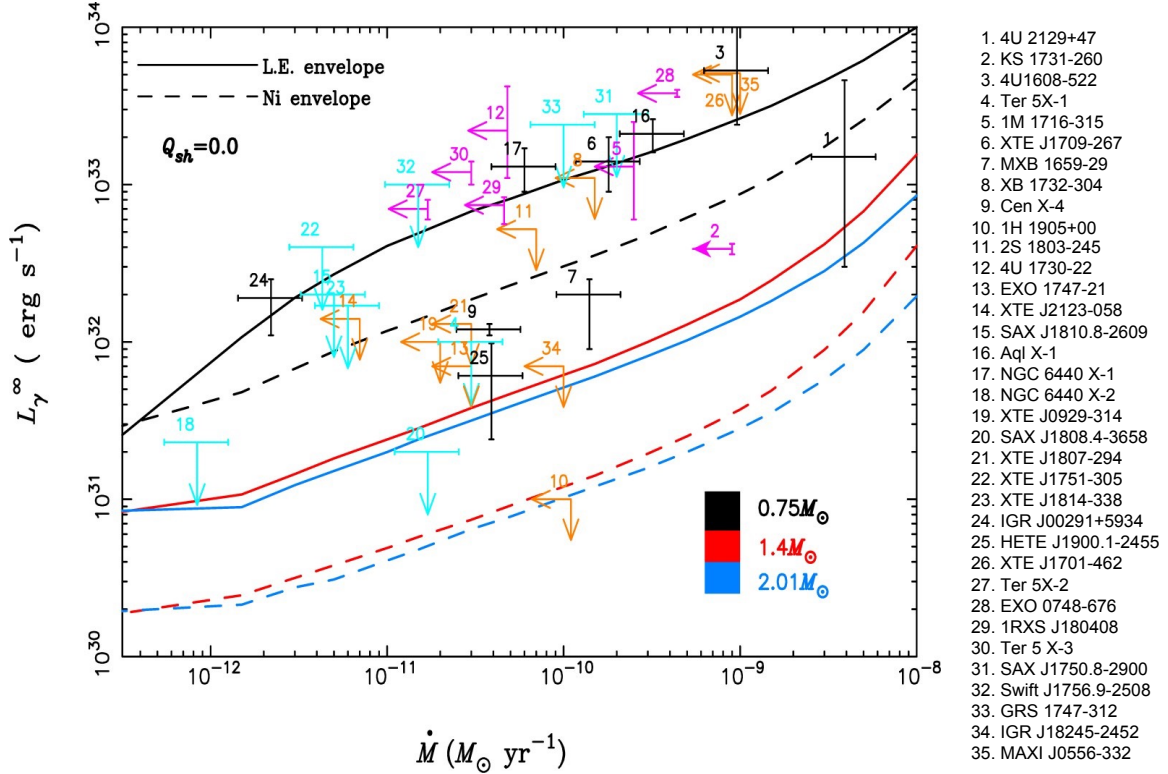
23

Fig. 1.10: Redshifted quiescent luminosity versus averaged mass-accretion rate for different neutron star masses (marked by color) and surface compositions (marked by line style) [66] (courtesy: Prof. Helei Liu). The errorbars and arrows show the observations of 35 Soft X-ray transients listed in the right margin, whose data are taken from Ref. [67]. Q_{sh} denotes the *unphysical* shallow heating rate artificially used to explain some hot Soft X-ray transients such as RX J0812.4–3114 [68], which we introduce in Section 5.

where L_{ch} is the crustal heating luminosity, L_ν is the neutrino luminosity, L_γ is the photon luminosity, and C_V is the capacity of NSs. Note that this is a non-relativistic energy conversation. We also note that initial states to move into the quiescent phase are not important though we consider the very hot NSs as the initial era as the above. Therefore, we can obtain thermal luminosity comparable with observations as

$$L_\gamma = L_{ch} - L_\nu(> 0) , \qquad (1.33)$$

Fig. 1.10 shows the observational quiescent luminosities and time-averaged accretion rate in the outburst phase. In cooling models shown in this figure, the DU process operates with $M_{NS} = 1.4$, and 2.1 $M_\odot$ and hence the quiescent luminosities become low compared with those of $M_{NS} = 0.75\ M_\odot$. In particular, to explain the data of 1H 1905+00 and SAX 1808.4−3658, a stronger rapid cooling process than the meson Urca process is required, although previous cooling models have not considered the corresponding EOSs with meson condensation [53]. Hence, as with the isolated NSs, observations of accreting NSs can also probe the interior of NSs by comparing with models as in the case of cold isolated NSs.
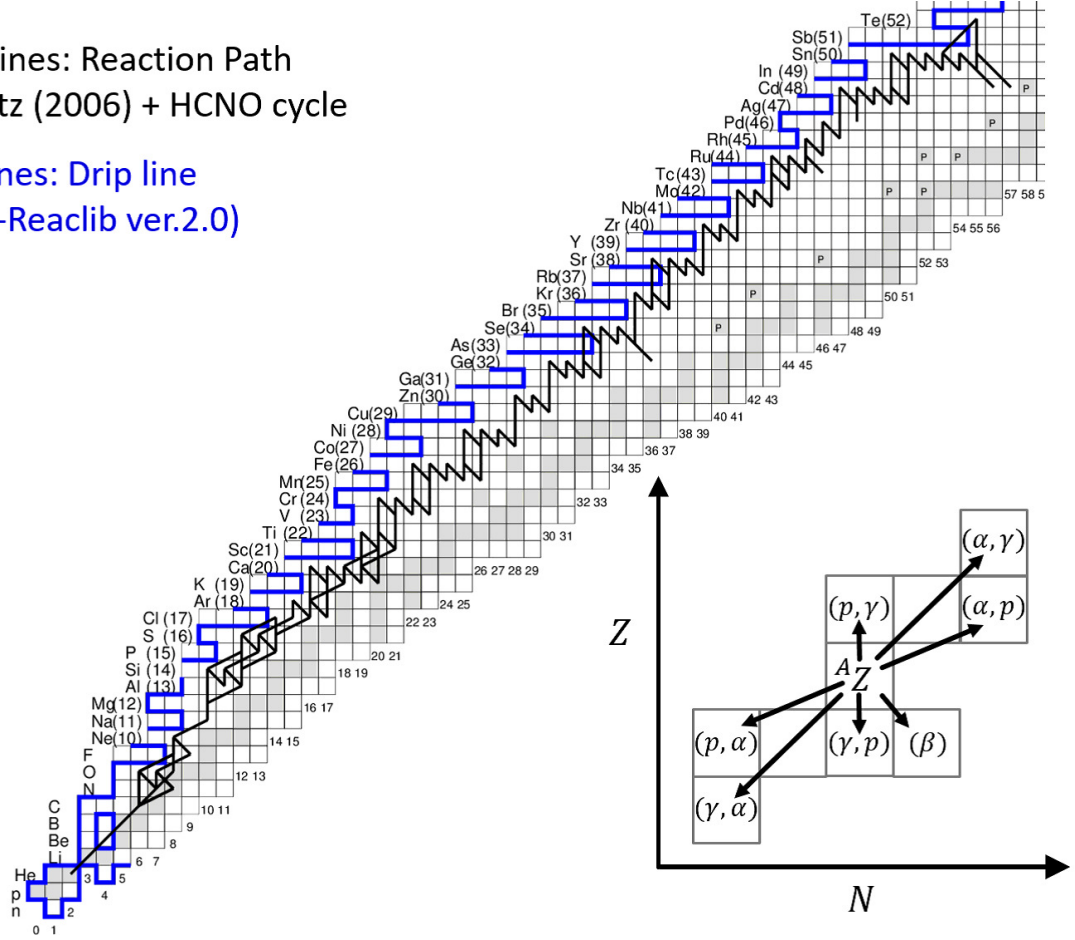
Fig. 1.11: Nuclear reaction flow during X-ray bursts with unstable mixed H/He burning. Black lines indicate the flow of X-ray burst nucleosynthesis baed on the typical model [75]. Blue lines are proton drip lines obtained from Jina Reaclib ver 2 [76] (Taken from Ref. [63], courtesy: Dr. Yasuhide Matsuo).

1.2.3 Type-I X-ray Bursts

X-ray bursts are rapidly brightening phenomena observed in LMXBs. Since the first discovery of X-ray burst in 4U 1820–30 in 1975 [71], 115 X-ray bursters have been observed so far [72]. There are two categories of X-ray burst from the point of energy generation; Type-I and Type-II X-ray bursts. Type-II X-ray burst is thought to be caused by the release of gravitational energy, and the corresponding X-ray bursters are the only MXB 1730–335 [73] and GRO J1744–28 [74] so far. Hence, we focus on the Type-I X-ray burst in this thesis.

In the outburst phase, NSs actively accrete from their companions, and the NS temperature continues to increase because the matter is accumulated on the surface. If the temperature is higher than around $T = 0.2$ GK, roughly corresponding to the temperature of helium ignition, unstable nuclear burning is triggered by hydrogen and helium burning. Such a thermonuclear explosion leads to Type-I X-ray burst. The type-I X-ray burst begins from the ignition of helium, i.e., triple-α reaction of $\alpha(\alpha\alpha, \gamma)^{12}$C. The reaction flow after triple-α reaction is summarized in Fig. 1.11. The typical burst light curve is shown in Fig. 1.12. For the behavior of burst light curves associated with nucleosynthesis, we explain below.

After carbon synthesis, the next nucleosynthesis is the hot-CNO cycle, which is the loop
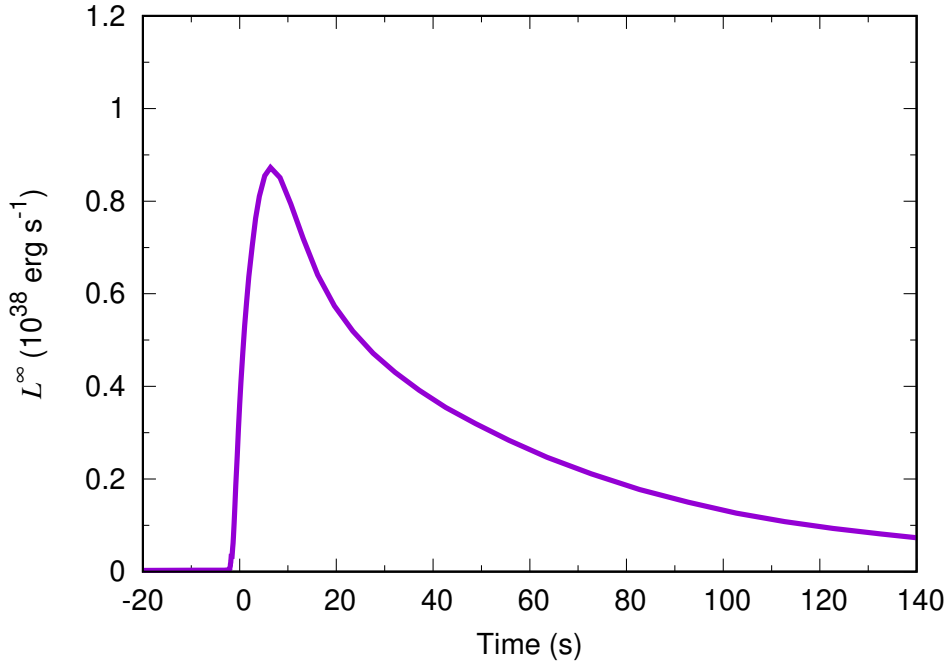
Fig. 1.12: A typical light curve during X-ray burst: Redshifted luminosity against time sequence.

reactions through the fuels of carbon, neon, and oxygen. The flow is shown in Fig. 1.13. During the hot-CNO cycle, since the half-life of ^{14}O (1 minute) is much shorter than that of ^{13}N (10 minutes), the temperature rapidly increases and the luminosity linearly increases. When the temperature exceeds $T \approx 0.5$ GK, the breakout from the hot CNO-cycle occurs, and the luminosity reaches the maximum value, typically $L \sim 10^{38}$ erg s^{-1}. After the breakout of the hot CNO-cycle, the luminosity decreases exponentially until $t \sim 100$ s.

Nucleosynthesis just after the breakout from the hot CNO cycle is initiated by mainly a αp process, which is a series of (α, p) reactions and (p, γ) reactions. Due to the small or negative proton capture Q-value, (p, γ) reaction rates are usually larger than (α, p) ones. Thus, nucleosynthesis proceeds via both (α, p) and (p, γ) reactions. However, (α, p) reactions are suppressed as the charge of target nuclei becomes large because of the Coulomb barrier, whose potential is proportional to the products of charges of each nucleus. Thus the αp-process can synthesize the heavy nuclei with the charge $Z \lesssim 20$.

For the synthesis of nuclei with $Z \gtrsim 20$, the dominant nucleosynthesis is a rapid proton capture (rp) process, which is a series of proton capture reactions and β decays. For the same reason as the αp-process, (p, γ) reactions are much faster than β decays. Thus, nucleosynthesis must wait for the relatively slow β decay. Especially an even-even nucleus with a small Q-value and long life is often called a waiting point. However, the total lifetime of a waiting point nucleus may be significantly reduced by sequential two-proton capture reactions $(2p, \gamma)$ [77, 78], depending on the nuclear masses of nuclei [79]. If the temperature increases enough, the nucleosynthesis proceeds towards the nuclei having the mass number $A \approx 107$ by the rp process with sequential two-proton capture reactions. The rp process is thought to end with the SnSbTe cycle [80]. Then, the burst phase is regarded to be terminated.

As there has been no clear observational evidence of compositions in nuclear ashes, light
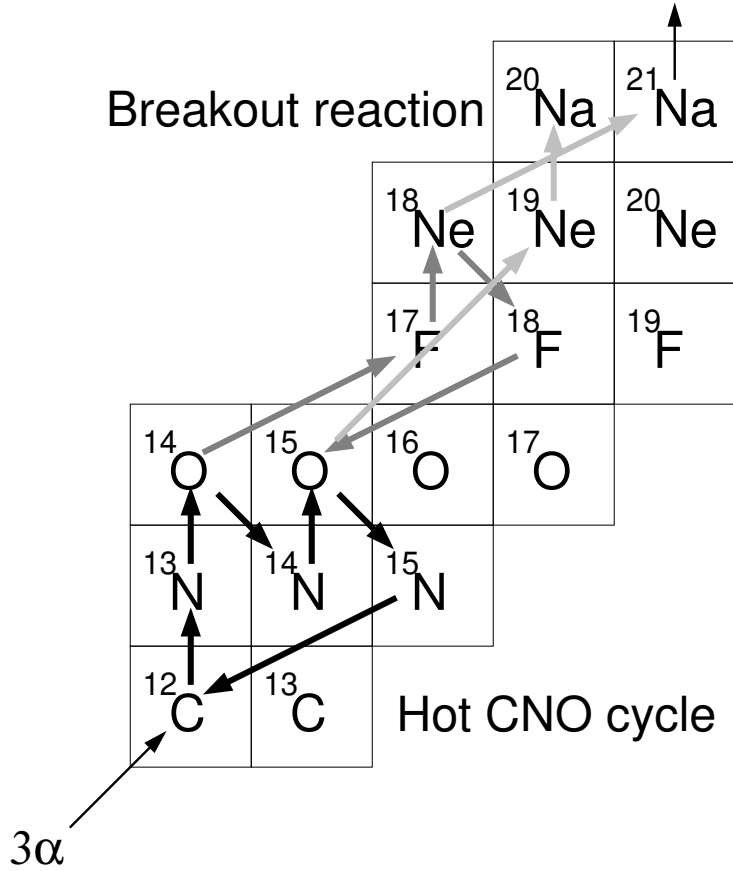
Fig. 1.13: Nuclear reaction sequences for the Hot CNO cycle and the breakout from the cycle.

curves are almost the only observational probe for X-ray bursts. The physical mechanism of X-ray bursts has been investigated in many works (e.g., Refs. [56, 81, 82]) with the use of numerical simulations. They found some input parameters are of importance in describing the burst models: the mass accretion rate $(\dot{M})$, the initial metallicity (Z_{CNO}) in the accreted matter, the hydrogen to helium ratio (X/Y), the reaction rates of the light nuclei, and the rp-process path. On the other hand, properties of burst light curve are characterized by a set of observable parameters: the recurrence time (Δt) between burst events, the peak luminosity (L_{peak}), the burst duration from the peak (τ), and the α parameter, which is the ratio of the persistent flux to the burst flux. For most burst observations, the burst behavior is not periodic mainly due to the difference in the accretion rate for each epoch and the observable parameters such as Δt and L_{peak} vary irregularly.

Remarkably, a few bursters show the almost same pattern of light curves in a burst sequence. They are often called *Clocked bursters* or *textbook burster*. In particular, X-ray bursts from GS 1826–24, whose first X-ray burst was observed in 1989 by the Ginga satellite [84], are the most commonly used as such references. Fig. 1.14 shows the burst light curves of GS 1826–24 for three epochs. As we see, the shape of the light curve for each epoch seems almost constant.
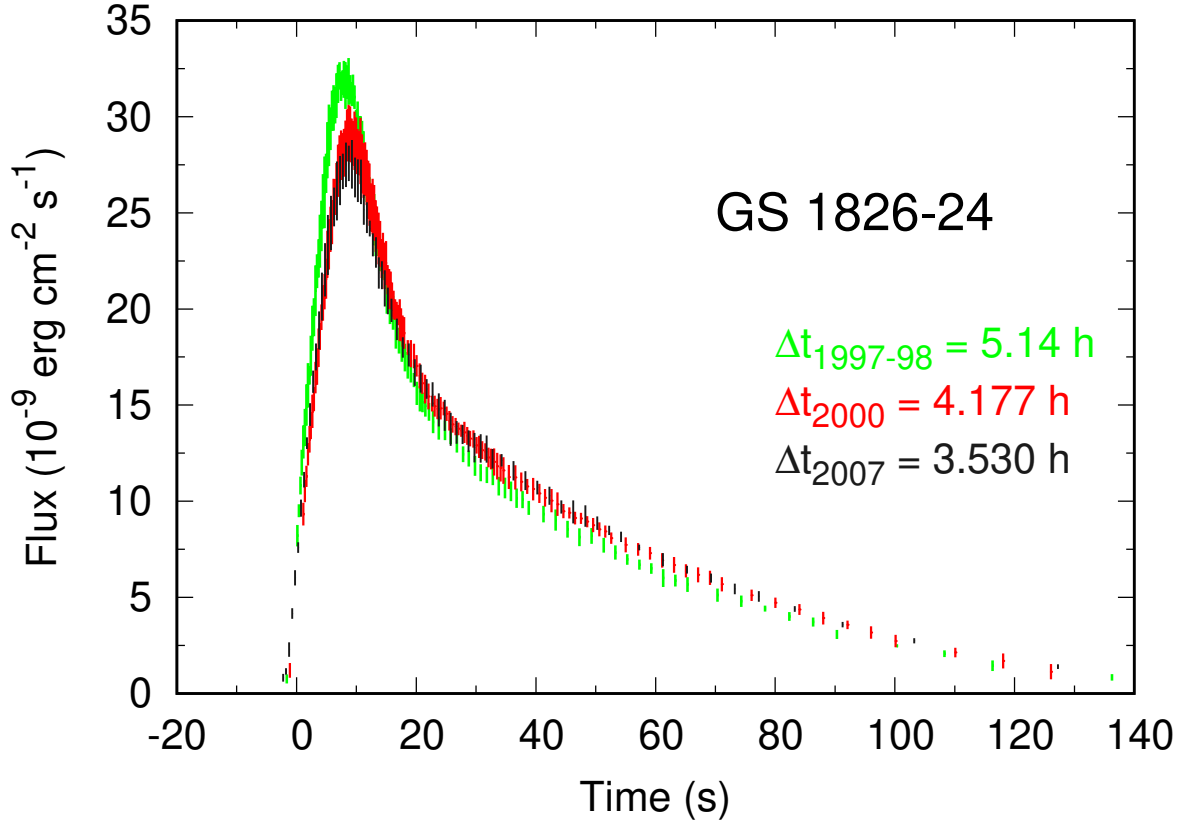
Fig. 1.14: Averaged burst light curves of GS 1826–24 for three epoch based on the observational data of Ref. [83]. Averaged recurrence time for each epoch is also shown.

We also note that the recurrence time Δt is almost unchanged. Hence, observations of *Clocked bursters* help test the validity of theoretical models [85]. In fact, the constraints on several physical parameters especially for NS exterior have been performed using light curves of a Clocked burster GS 1826–24 [56, 85, 86, 87, 88, 89].

However, there is no previous work to examine the effects of NS physics on X-ray bursts, such as the EOS uncertainties and neutrino cooling effects. These come from the Newtonian formalisms of previous work to exclude the regions inside NSs. This brings up the following two issues: One is the treatment of NS self-gravity, based on non-relativistic hydrodynamic formulation. Although sophisticated correction of general relativity has been considered [90], burst models based on a relativistic formulation are primarily desired for more exact calculation of light curves.

The other one is to give the boundary condition on the crust surface. In other words, they necessarily treat the boundary luminosity or temperature, which is artificially given without fully considering the microphysics inside NSs, e.g., the crustal heating, the neutrino emission, and the EOS uncertainties. The heating and neutrino cooling of the NS, which affect the burst light curves via the change in the surface temperature, are essential for X-ray burst modeling [91, 81, 92]. To include the energy exchange between the interior NS and the accreting layer, previous studies have adopted a heating factor Q_b on the crust in the energy equation, which was treated as an adjustment parameter. Hence, this parameter should be essentially determined by solving the thermal evolution of the NS.

Related to the NS heating and cooling, the EOS also plays an important role in X-ray-burst modeling because the surface gravity affects the amount of fuel [93]. We also emphasize that the heating and cooling rates inside NSs crucially depend on EOSs, such as the presence or absence of the DU process. Therefore, observations of X-ray bursts, particularly Clocked bursters, may give a constraint on the EOS. Similar to the treatment of Q_b, the general-relativistic effect should be included by solving X-ray-burst calculations over whole NS regions.

1.3 Purpose

There are still large uncertainties in nuclear EOSs apart from recent observational developments, especially for NS mass and radius. However, since the X-ray thermal emissions from the NS surface indirectly reflect the information inside NSs, the observed temperature and luminosity of NSs can extract the NS physics such as the EOS through modeling the various thermal evolution of NSs.

At first, focusing on the observations of cold isolated/accreting NSs necessary for rapid cooling processes, we examine the uncertainties of EOS on the cooling history of NSs. In particular, we shall consider the pion condensation in both EOSs and neutrino cooling processes, while previous work did not consider the softening effects on EOSs due to meson condensation. Next, we investigate the EOS dependence in connection with burst light curves and their characterized parameters, such as Δt and L_{peak}. To probe physics inside NSs, we compare our models with the *Clocked burster* GS 1826–24. Finally, we also examine the EOS dependence on final products after proton-rich nucleosynthesis.

This thesis is organized as follows. Section 2 presents our adopted EOSs without and with pion condensation and their comparison with various observations. Section 3 shows the basic formulae and numerical method for thermal evolution of NSs. Section 4 presents the EOS dependence of cooling curves of isolated NSs. Section 5 presents the EOS dependence of quiescent luminosities of accreting NSs. In Section 6, which is the main part of this thesis, presents EOS dependence and neutrino cooling effects in close relation to burst light curves and focuses on the modeling GS 1826–24 and proton-rich nucleosynthesis. Section 7 is devoted to a conclusion.

Chapter 2

Equation of States

In this chapter, we present some EOS models with different properties of nuclear matter, including the effects of pion condensation. We discuss the differences of the symmetry energy on the softening effects on EOSs due to the pion condensation, which is crucially important for the consistency with the observations of high-mass NSs $\gtrsim 2\ M_\odot$. We also compare them with various observational constraints and evaluate the consistency for each EOS.

2.1 EOS Models

The simplest description of the compositions inside NSs is that the core contains only neutrons, protons, electrons, and muons. As such a standard nuclear-matter EOS, we adopt four kinds of finite-temperature EOSs: Togashi [94], LS220 [95], TM1 [96, 97, 98], and TM1e [99, 100]. The LS220 EOS is constructed based on Skyrme interaction with the incompressibility of 220 MeV. The TM1 EOS is based on the relativistic mean-field theory with several meson couplings. They have been used in many astrophysical simulations for long years, while the Togashi and TM1e EOSs have been recently constructed. The Togashi EOS is based on the bare nuclear force for two-body interaction and phenomenological three-body interaction in the variational approach. The TM1e EOS is based on the extended relativistic mean-field theory updated from the TM1 EOS, where the ω–ρ coupling term is newly added to the nucleonic Lagrangian density, which significantly affects the softness of EOSs.

The information of NS EOS such as the pressure and energy density comes from the energy per nucleon $w(\rho_B, Y_p)$, where ρ_B is the baryon density and Y_p is the proton fraction, which can be expanded around the saturation density ρ_{nuc}:

$$w(\rho_B, Y_p) = w_0 + \frac{K_0}{18\rho_{\mathrm{nuc}}^2}\left(\rho_B - \rho_{\mathrm{nuc}}\right)^2 + \cdots + \left[E_{\mathrm{sym}} + \frac{L}{3\rho_{\mathrm{nuc}}}\left(\rho_B - \rho_{\mathrm{nuc}}\right) + \cdots\right]\left(1 - 2Y_p\right)^2, \quad (2.1)$$

where w_0, K_0, E_{sym}, and L are, respectively, energy per nucleon, incompressibility, symmetry energy, and its slope at ρ_{nuc}. The term inside the square bracket of Eq. (2.2) is a density-dependent symmetry energy $S_0(\rho_B) = E_{\mathrm{sym}} + \frac{L}{3\rho_{\mathrm{nuc}}}\left(\rho_B - \rho_{\mathrm{nuc}}\right) + \cdots$, which indicates the efficiency to create protons in the NS core. In the vicinity of the saturation density, the properties of nuclear matter are mostly characterized by the five parameters, i.e., ρ_{nuc}, w_0, K_0, E_{sym}, and L, which are tabulated in Table 2.1. Recent terrestrial experiments suggest 220 MeV $\lesssim K_0 \lesssim$ 260 MeV,

Table 2.1: Physical quantities at the nuclear saturation density for adopted EOSs

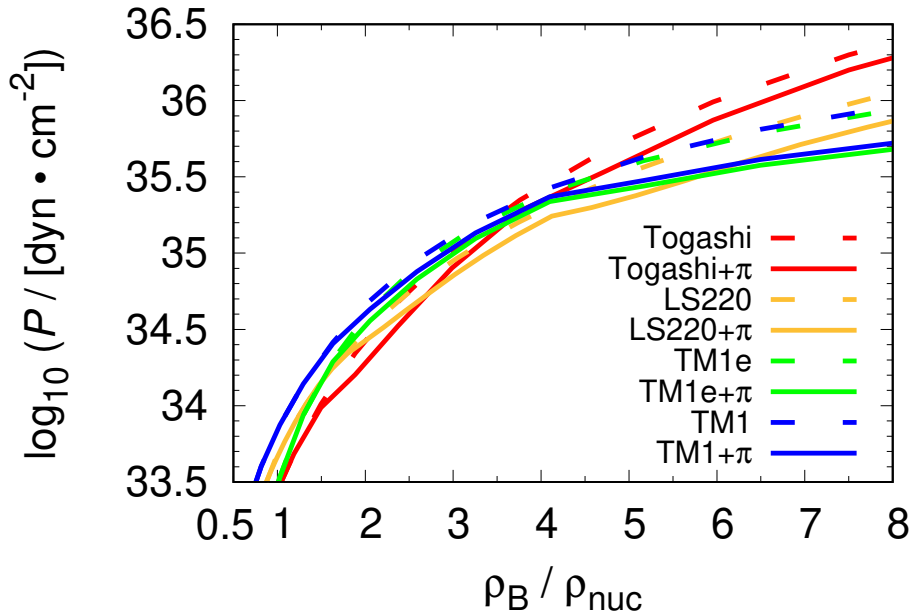| EOS	ρ_{nuc} $[10^{14}$ g cm$^{-3}]$	w_0 [MeV]	K_0 [MeV]	E_{sym} [MeV]	L [MeV]
Togashi	2.66	-16.0	245	30.0	35.0
TM1	2.41	-16.3	281	36.9	111
TM1e	2.41	-16.3	281	31.4	40.0
LS220	2.57	-16.0	220	28.6	73.8

Fig. 2.1: Pressure-Density relation with adopted EOSs: Togashi(red), LS220(yellow), TM1e(green), and TM1(blue). Solid curves indicate EOS without pion condensation while Dashed curves with pion condensation modeled by Ref. [58] (labeled as "EOS+π").

$S_0 \lesssim 36$ MeV, and $L \lesssim 80$ MeV [101, 102]. Therefore, the Togashi and LS220 EOSs are consistent with the experimental values among adopted EOSs. For low-density regions around the crust surface ($\rho < 10^{10}$ g cm^{-3}), since the results of nuclear-matter EOSs are inappropriate for such low-density matter, we connect the nuclear EOSs to the BPS EOS in Ref. [103] adding thermal components of ideal gases. For the density regions of accreted layers, we apply the Helmholtz EOS in Ref. [104].

Recent studies indicate the possibilities of exotic states inside NSs, such as hyperons, deconfined quarks, and meson condensation (for a review, see Ref. [105]). In the present study, we consider a pion condensation, which is known to appear in lower-density regions compared with other exotic states. For the pion condensation model, we adopt Ref. [58] based on SU(2) chiral symmetry approach. This model incorporates the attractive force by isobar $\Delta(1232)$ excitations and the repulsive force by nucleon-nucleon short-range correlations. Since their interactions conflict with each other, the competitive relationship of nuclear force arises. Then, if the total nuclear interaction becomes attractive, the pion condensation could occur. The apparent density is characterized by Landau-Migdal parameter $\tilde{g}'$, which means the strength of nucleon-

nucleon($\tilde{g}'_{NN}$), nucleon-isobar($\tilde{g}'_{N\Delta}$), and isobar-isobar($\tilde{g}'_{\Delta\Delta}$) interactions, assuming universality as $\tilde{g}' \equiv \tilde{g}'_{NN} = \tilde{g}'_{N\Delta} = \tilde{g}'_{\Delta\Delta}$. We adopt $\tilde{g}' = 0.5$ in our models. Charged pion (π^c) condensation phase appears at $\rho_B \simeq 1.6\rho_{\rm nuc}$. In much higher density regions, π^c condensation phase transits into a combined phase of neutral and charged pions (π^0–π^c) condensation at $\rho_B \simeq 3.9\rho_{\rm nuc}$ [106] (see Table 5 in Ref. [107]). Although the short-range correlation in nuclei is highly uncertain, some experiments have indicated that the pion condensation begins at $(1.9 \pm 0.3)\rho_{\rm nuc}$ or $(1.8-2.4)\rho_{\rm nuc}$ [108, 109]. These experimental results agree with the theoretical prediction of Ref. [58]. If the pion condensation occurs, the EOS becomes significantly soft. The quantitative effect depends on the stiffness of properties with the standard-nuclear matter without pion condensation phases. Focusing on this point, we investigate how the stiffness of standard-nuclear EOS changes the pressure-density and mass-radius relations with pion condensation.

By adding the energy density and pressure in the normal nuclear matter to their negative gain because of pion condensation, we construct the EOS in the pion-condensation matter. The numerical value of gains is adopted in Ref. [107]. First, we show the pressure-density relations of EOSs in Fig. 2.1. As we see, the Togashi is soft for $\rho \sim \rho_{\rm nuc}$ and stiff for $\rho \gg \rho_{\rm nuc}$. This trend is in contrast to TM1, TM1e, and LS220. Considering the pion condensation, the softening effect appears at a lower density with the Togashi than with other EOSs. Meanwhile, the Togashi does not become softer for $\rho_B \gtrsim 4\rho_{\rm nuc}$ than other EOSs. The difference in density dependence of EOSs comes from the symmetry energy, especially for the slope parameter L. As we see in Table 2.1, the Togashi EOS has the smallest value of L, while the TM1 has the largest value. If the L is lower, the density gradient of symmetry pressure inside NSs is lower, and this correctly corresponds to the pressure-density relation in Fig. 2.1.

Next, we consider the mass-radius relation, which is obtained by solving Tolman-Oppenheimer-Volkoff(TOV) equations follows [118, 119] :

$$\frac{\partial M_{tr}}{\partial r} = 4\pi r^2 \rho \,, \tag{2.2}$$

$$\frac{\partial P}{\partial r} = -\frac{GM_{tr}\rho}{r^2} \frac{\left(1 + \frac{P}{\rho c^2}\right)\left(1 + \frac{4\pi r^3 P}{M_{tr}c^2}\right)}{1 - \frac{2GM_{tr}}{c^2 r}} \,, \tag{2.3}$$

where M_{tr} is the gravitational mass and ρ is the energy density. We present the results for each EOS in Fig. 2.2. Numerical values of maximum mass and radius are listed in Table 2.2. If the pion condensation is included, the maximum mass and radius are reduced in any EOS. We can see that their density dependence is different among EOSs; Stiff EOSs for $\rho_B \gg \rho_{\rm nuc}$ do not feel the softening effect due to pion condensation so much. Hence, the maximum mass with the Togashi is not significantly reduced due to the pion condensation, while highly reduced with other EOSs. On the other hand, the Togashi is soft around $\rho_B \sim \rho_{\rm nuc}$ and the radius is highly reduced even with light stars. These trends are opposite to stiff EOSs such as the TM1. The TM1e and LS220 have roughly intermediate properties between Togashi and TM1, although the softening effect in LS220 can be seen compared with others. Thus, if the symmetry energy roughly corresponding to the value of L is lower, although the radius becomes smaller even with low-mass NSs, the maximum mass is less affectable by the pion condensation. Considering the observations of massive NSs with $\sim 2\,M_\odot$, low-symmetry-energy EOSs such as the Togashi
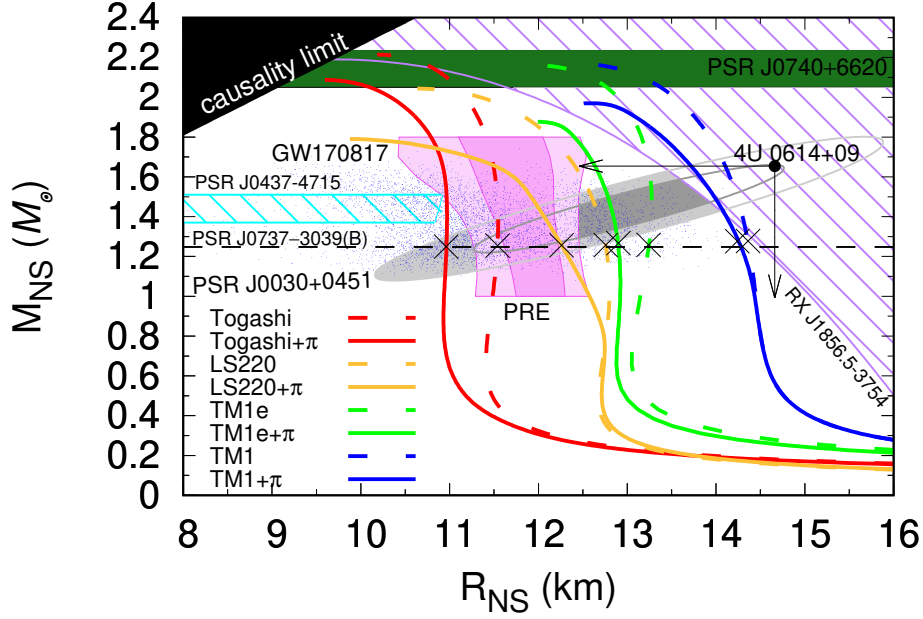
Fig. 2.2: Mass-radius relation with adopted EOSs. The green band shows the highest-mass measurement of $2.14^{+0.10}_{-0.09} M_\odot$ of PSR J0740–6620 [27]. Many blue dots indicate the results from the observation of GW170817 [110]. Grey cycles indicate the limits of allowed 1σ(thick) and 2σ(thin) regions of pulsar J0030+0451 discovered by *NICER* observation [10, 111]. Thick(1σ) and thin(2σ) magenta regions show the allowed ones from observational constraints of photospheric radius expansion in six low-mass X-ray binaries (LMXBs) [112]. The black point shows the upper-limit mass and radius implied from the kHz QPO observations in LMXBs 4U 0614+09 [113]. Two hatched regions labeled with purple and cyan indicate the excluded ones derived from the thermal radiation of the isolated NS RX J1856.5−3754 [114, 115] and thermal pulses from a radio millisecond pulsar PSR J0437–4715 (3σ regions in Ref. [116]), respectively. For the latter constraint, we combine it with the observed mass of $M_{NS} = 1.44 \pm 0.07\ M_\odot$ reported by Ref. [117]. "×" denotes the mass with the baryon mass $M_B = 1.375\ M_\odot$ which is the upper limit from observation of PSR J0737−3039(B). The dashed black line shows its lower limit of observational mass $M_{NS} = 1.248\ M_\odot$. If the observational mass is higher than the mass denoted as "×", the EOS is rejected.

Table 2.2: Maximum mass M_{max} and radius with different masses for each EOS.

EOS	M_{max} ($M_\odot$)	$R_{\mathrm{NS}}(1.0M_\odot)$ (km)	$R_{\mathrm{NS}}(1.4M_\odot)$ (km)	$R_{\mathrm{NS}}(1.8M_\odot)$ (km)	$R_{\mathrm{NS}}(M_{\mathrm{max}})$ (km)
Togashi	2.21	11.49	11.57	11.41	10.18
Togashi+π	2.09	10.94	10.97	10.79	9.60
LS220	2.04	12.80	12.68	12.14	10.64
LS220+π	1.79	12.46	12.07	-	9.88
TM1e	2.13	13.15	13.27	13.16	12.40
TM1e+π	1.88	12.92	12.85	12.40	11.99
TM1	2.18	14.45	14.30	13.93	12.35
TM1+π	1.97	14.44	14.12	13.40	12.51

might be observationally favored, as we explain later. On the other hand, if the symmetry energy is higher, the maximum mass is highly reduced enough not to reach 2 $M_\odot$.

2.2 Various Observational Constraints

To test our constructed EOSs in detail, we compare our EOSs with various observational constraints, which we explain below. The final results for testing EOSs are summarised in Table 2.3.

2.2.1 Maximum mass constraint from a heaviest object of PSR J0740+6620

Recent observations of some massive pulsars exclude many soft EOSs which cannot support $2M_\odot$. In particular, if exotic states are included, the EOS tends to become soft significantly and may fail to reproduce $2M_\odot$ stars (*hyperon puzzle*, but see also Ref. [120]). Hence, *hyperon puzzle* is the most crucial condition for testing exotic-matter EOSs. Currently, the heaviest NS observed so far is a pulsar PSR J0740+6620. The Shapiro-delay based mass measurement shows $M = 2.14^{+0.10}_{-0.09}M_\odot$ [27]. For standard nuclear-matter EOSs, the only LS220 EOS cannot slightly reach the lower maximum mass of 2.05 $M_\odot$, while others can reproduce the observations of maximum mass. In adopted EOSs, the LS220+π, TM1e+π, and TM1+π are inconsistent with the observation, while the Togashi+π is consistent. As the above, the main reason is the difference in stiffness of standard-nuclear-matter EOS in high-density regions. Hence, considering the low-symmetry-energy EOS with pion condensation has a high possibility to reproduce $2M_\odot$ stars.

2.2.2 Constraint from GW170817

The first discovery of gravitational wave emitted from NS-NS merger, GW170817, gives the constraint on the radius. The key to extracting the information of interior NS from the analysis of gravitational-wave data is how the NSs are deformed by the tidal force, which is estimated to be $\Lambda_{1.4} \lesssim 800$ [13] or $\Lambda_{1.4} \lesssim 580$ [110] where $\Lambda_{1.4}$ is the tidal deformability with 1.4 $M_\odot$ stars. The data of mass-radius constraints are adopted from Ref. [110], which results in $R_{\mathrm{NS}} \lesssim 13.6$ km with $1.4M_\odot$ stars. Hence, many EOSs with high symmetry energy, such as the TM1, are rejected.

2.2.3 Constraint from recent *NICER* observation of PSR J0030+0451

Recently, the X-ray timing observation of a millisecond pulsar PSR J0030+0451 by Neutron Star Interior Composition Explorer (*NICER*) enables us to constrain the EOS, in particular, the compactness M/R [10]. The detailed analysis considering the correlation between mass and radius has been done by Ref. [111], which results in $M_{\rm NS} = 1.44 \pm 0.145\sigma$ $M_\odot$ and $R_{\rm NS} = 13.02 \pm 1.15\sigma$ km, where σ is the standard derivation. The constraints in 1σ and 2σ regions are adopted in this study. In our EOSs, all EOSs except Togashi+π can pass through the allowed 1σ regions. Considering the 2σ regions, Togashi+π becomes a consistent model. This means that the current observation by *NICER* cannot reject all adopted EOSs, and we have waited for future observations by *NICER* for more constraints on EOS.

2.2.4 Constraint from the observations of photospheric radius expansion

The observational fluxes of burst and quiescent phases in LMXBs enable us to probe the mass and radius. In particular, the observations of photospheric radius expansion (PRE) give their constraints due to their high brightness, which is equal to the Eddington luminosity ($> 10^{38}$ erg s^{-1}). In this work, we adopt the analysis of six LMXBs of Ref. [112], which results in a preferred radius of around 11–12 km. Therefore, the Togashi and LS220+π EOSs are in good agreement with the allowed 1σ regions. Furthermore, Togashi+π, LS220, and TM1e+π can pass through the allowed 2σ regions. We note that, however, the constraining regions of PRE observations might be changed due to some uncertain factors, such as the distance, compositions of the atmosphere, and the position of the photosphere (for review, see Ref. [24]).

2.2.5 Constraint with the analysis from PSR J0437−4715

The observed X-ray pulsations with XMM-Newton from the closest millisecond pulsar PSR J0437−4715 can probe the EOS [116]. The constraint in 3σ regions is adopted in this study. Moreover, we combine this constraint with its latest measured mass, which is measured in a radio timing method in the Parkes Pulsar Timing Array ($M_{\rm NS} = 1.44 \pm 0.07$ $M_\odot$) [117]. Finally, the radius with this corresponding mass region is constrained as $R_{\rm NS} > 10.9$ km. All our models, including the smallest-radius model of the Togashi+π, match with the above constraints[1].

2.2.6 Constraint from kHz QPO in LMXB 4U 0614+09

In several LMXBs, quasi-periodic brightness oscillations (QPOs) have been observed. If the frequency is highly comparable to the orbital frequency of NS, the upper mass and radius could be determined simultaneously. So far, the highest frequency of the QPOs observed is 1.33 kHz in 4U 0614+09 [113]. Such a kHz QPO observation gives following loose constraints: $M_{\rm NS} < 1.65$ $M_\odot$ and $R_{\rm NS} < 14.7$ km without NS spin. Our EOSs are all consistent. If another kHz QPO with a higher frequency than 4U 0614+09 is observed in the future, the NS radius is preferred to be small with light stars.

---

[1]Note that, however, the observational constraints of thermal pulses from PSR J0437−4715 in 2σ regions exclude the Togashi and in 1σ areas the TM1e as well, in regardless of the effect of pion condensation.

Table 2.3: Summary of the results to test our EOSs with use of observational constraints present in subsections 2.2.1–2.2.8.

EOS	2.2.1 ($M_{\mathrm{max}} \geqslant 2.05 M_\odot$)	2.2.2	2.2.3 1σ	2.2.3 2σ	2.2.4 1σ	2.2.4 2σ	2.2.5 (3σ)	2.2.6	2.2.7	2.2.8
Togashi	✓	✓	✓	✓	✓	✓	✓	✓	$M_{\mathrm{NS}} \lesssim 2.1 M_\odot$	✓
Togashi+π	✓	✓	×	✓	×	✓	✓	✓	✓	✓
LS220	×	✓	✓	✓	×	×	✓	✓	✓	✓
LS220+π	×	✓	✓	✓	✓	×	✓	✓	✓	✓
TM1e	✓	✓	✓	✓	×	×	✓	✓	$M_{\mathrm{NS}} \lesssim 1.7 M_\odot$	✓
TM1e+π	×	✓	✓	✓	×	✓	✓	✓	✓	✓
TM1	✓	×	✓	✓	×	×	✓	✓	$M_{\mathrm{NS}} \lesssim 1.3 M_\odot$	✓
TM1+π	×	×	✓	✓	×	×	✓	✓	$M_{\mathrm{NS}} \lesssim 1.4 M_\odot$	✓

2.2.7 Possible constraint from thermal radiation of RX J1856.5−3754

Seven isolated NSs are known to emit thermal X-ray radiation. In such a group called *magnificent seven*, the only object where the distance is measured is RX J1856.5−3754. Its blackbody radius R_∞ is obtained, and therefore we could constrain on NS mass and radius [114]. We use the best fitting value $R_\infty = 16.8$ km of the spectrum with blackbody emissions [115]. The constraint of $R_{\mathrm{NS}} < R_\infty$ excludes the possibility of high-mass NSs in TM1, TM1+π, TM1e and Togashi. However, the constraint always allows the low-mass NSs to exist with all EOSs, although the distance is uncertain. Hence, compared with other constraints, it is hard to probe high-density EOS from kHz QPO observations.

2.2.8 Possible constraint from the masses of PSR J0737−3039(B)

PSR J0737−3039 is the NS in the double pulsar system, which may probe the EOS in high-density regions. The pulsar B, a lower-mass object in the system, is a light star with $M_{\mathrm{NS}} = 1.249 \pm 0.001\ M_\odot$. Such a light star is generally hard to be born by a type-II supernova, triggered by a collapse of the Fe core of a massive progenitor. As one of the scenarios to produce light NSs, an electron-capture supernova of a ONeMg core is suggested and confirmed from recent observation [121]. Setting the critical density of ONeMg core as 4.5×10^9 g cm^{-3}, the baryon mass of ONeMg core just before its collapse is estimated to be 1.375 $M_\odot$. Then, the baryonic mass of formed NS is given as $M_{\mathrm{B}} \lesssim 1.375\ M_\odot$ [122]. We show the gravitational mass corresponding to $M_{\mathrm{B}} = 1.375\ M_\odot$ for each EOS in Fig. 2.2. We also show the measured mass of $M_{\mathrm{NS}} = 1.249 \pm 0.001\ M_\odot$, which should be higher than the gravitational mass with $M_{\mathrm{B}} = 1.375\ M_\odot$. We confirm that this condition is satisfied for all EOSs.

Some previous studies consider the lower bounds of M_{B} derived from how the matter in the ONeMg core is ejected (e.g., Ref. [123]). If there is no mass loss of the parent ONeMg core, $M_{\mathrm{B}} \gtrsim 1.366\ M_\odot$ [122]. By comparing it with the baryonic mass with $M_{\mathrm{NS}} = 1.249 \pm 0.001\ M_\odot$, we can test the EOS. As a result, all our EOSs are consistent with the constraints without mass loss. If we consider the mass loss, the estimated baryonic mass should be reduced, and the consistency is also changed. For example, one-dimensional core-collapse supernova simulation of ONeMg core shows the result of $M_{\mathrm{B}} = 1.360 \pm 0.002\ M_\odot$ with a mass lose of $\sim 0.015\ M_\odot$ [124]. In that case, none of our adopted EOSs with $M_{\mathrm{NS}} = 1.249 \pm 0.001\ M_\odot$ passes through this allowed

region. Hence, this constraint has large uncertainties with the mass loss of the progenitor, but the baryonic-mass constraints from an electron-capture supernova can probe the NS EOS.

Chapter 3

Basic Formulations

3.1 Basic Equations

We assume that the hydrostatic equilibrium is achieved in the isolated/accreting NSs, including the case of the X-ray burst system, covering from the central NS core to the surface. In addition to the TOV equations Eqs. (2.2) and (2.3), the basic equations for the thermal evolution of neutron stars are written as follows [125, 126]:

$$\frac{\partial(L_r e^{2\phi/c^2})}{\partial M_r} = e^{2\phi/c^2} \left(\varepsilon_\mathrm{n} + \varepsilon_\mathrm{g} - \varepsilon_\nu\right) , \tag{3.1}$$

$$\frac{\partial \ln T}{\partial \ln P} = \min(\nabla_\mathrm{rad}, \nabla_\mathrm{ad}) , \tag{3.2}$$

$$\frac{\partial M_{tr}}{\partial M_r} = \frac{\rho}{\rho_0} \left(1 - \frac{2GM_{tr}}{c^2 r}\right)^{1/2} , \tag{3.3}$$

$$\frac{\partial \phi}{\partial M_{tr}} = \frac{G(M_{tr} + 4\pi r^3 P/c^2)}{4\pi r^4 \rho} \left(1 - \frac{2GM_{tr}}{c^2 r}\right)^{-1} , \tag{3.4}$$

where M_{tr} and M_r are the gravitational mass and the rest mass, respectively, enclosed in the radius r; ρ and ρ_0 denote the energy density and the rest-mass density, respectively; ϕ is the gravitational potential in the unit mass; P is the pressure and T is the temperature in the local frame; ε_ν represents the rate of energy loss via neutrino emission; ε_n and ε_g are the energy generation and the gravitational energy release rates, respectively. For isolated NSs, they are always zero, and then we can see that the luminosity monotonically decreases due to neutrino losses from Eq. (3.1). ∇_rad and ∇_ad are the radiative and adiabatic gradients, respectively. As we can see in Eq. (3.2), we assume the instant mixing of elements, which occurs for $\nabla_\mathrm{rad} < \nabla_\mathrm{ad}$. The only radiative gradient is valid in most cases of thermal evolution of NSs, but if the temperature in accreted layers rapidly increases such as the Type-I X-ray burst, the adiabatic gradient becomes also important.

In the accreted layer, we utilize the Eulerian coordinate of the mass fraction $q \equiv M_r/M(t)$ where $M(t)$ is the total mass each time. For stellar evolution calculations, the variable q is more useful than $M(r)$, because the computational time becomes much shorter [127]. The gravitational energy release rate ε_g, depending on on time, is divided into two terms, i.e., the

non-homologous ($\varepsilon_\mathrm{g}^{nh}$) and the homologous ($\varepsilon_\mathrm{g}^h$) components:

$$\varepsilon_\mathrm{g}^{nh} = e^{-\phi/c^2} \left(T \left. \frac{\partial s}{\partial t} \right|_q + \mu_i \left. \frac{\partial N_i}{\partial t} \right|_q \right), \tag{3.5}$$

$$\varepsilon_\mathrm{g}^h = e^{-\phi/c^2} \dot{M} \left(T \left. \frac{\partial s}{\partial \ln(q)} \right|_t + \mu_i \left. \frac{\partial N_i}{\partial \ln(q)} \right|_i \right), \tag{3.6}$$

where s is specific entropy and μ_i and N_i are the chemical potential and the number per unit mass of the i-th elements, respectively. The latter term ε_g^h indicates the compressional heating due to the accretion, which significantly contributes in the heat source in soft X-ray transients including X-ray bursters (e.g., Ref. [128]). Note that since the accreting NSs in quiescent phase are not compressed by the accretion, then ε_g^h is set to be zero [59].

In addition to TOV equations and Eqs. (3.1)–(3.4), the EOS and the opacity are essential relations to close the hydrostatic equation system:

$$\rho = \rho(P, T, Y_i) , \tag{3.7}$$

$$\kappa = \kappa(P, T, Y_i) , \tag{3.8}$$

where Y_i is the number fraction of i-th particle. The EOSs have already been introduced in the previous section. The opacity κ includes the components of radiation and conductive opacities, which mainly include the contributions from electrons, muons, and neutrons [129, 130, 131] (see also Ref. [132] for concretes expressions of lepton thermal conductivities.).

For the NS surface, we assume the radiative zero boundary condition, which can be expressed as follows [91]:

$$P = \frac{GMM(t)\,(1-q)}{4\pi R^4} \left(1 - \frac{2GM}{Rc^2} \right)^{-1/2} , \tag{3.9}$$

$$L = \frac{4\pi cGM}{\kappa} \frac{4aT^4}{3P} \frac{1 + \frac{\partial \log \kappa}{\partial \log P}}{4 - \frac{\partial \log \kappa}{\partial \log T}} \left(1 - \frac{2GM}{Rc^2} \right)^{1/2} . \tag{3.10}$$

These boundary conditions show that we view the computational luminosity at the outermost mesh point as the closest thing to the total luminosity L. Surface (Effective) temperature T_s is obtained from the Stefan-Boltzmann law:

$$L(r = R_\mathrm{NS}) = 7 \times 10^{32} \text{ erg s}^{-1} \left(\frac{R_\mathrm{NS}}{10 \text{ km}} \right)^2 T_{s,6}^4, \tag{3.11}$$

where $T_{s,6}$ is the surface temperature in units of 10^6 K, which is the typical temperature for the surface of isolated NSs. As the outer-mesh points to be sufficiently close to the photospheric area, we set the outer-mesh mass $M_\mathrm{outer} = 10^{-19} M_\mathrm{NS}$. We confirm the integrated luminosity inside the radius does not vary around $M_\mathrm{outer} \approx 10^{-17} M_\mathrm{NS}$. With the above conditions, we solve these hydrostatic equations from the NS center to the surface by the Henyey-type numerical scheme of an implicit-midpoint method with an adaptive grid in q and t. To numerically solve the above set of TOV equations (Eqs. (2.2) and (2.3)) and Eqs. (3.1)–(3.4), we adopt thermal evolution code of spherically symmetric NSs [91].

3.2 Treatment of Nuclear Reaction Network

For the calculation of X-ray bursts, we implement the nuclear reaction network to calculate the nuclear-burning energy. The nuclear generation energy rate is calculated from

$$\varepsilon_{\mathrm{n}} = 9.6845 \times 10^{17} \sum_i \frac{dY_i}{dt} (\mathrm{BE})_i \ \mathrm{erg \ g^{-1} \ s^{-1}}, \tag{3.12}$$

where $(\mathrm{BE})_i$ and Y_i denote the binding energy and mass fraction of i-th nuclei respectively. The time derivative of Y_i can be obtained by solving the rate equation as

$$\frac{dY_i}{dt} = \sum_j N_i \bar{\lambda}_j Y_j + \sum_{j,k} \frac{N_i}{N_j! N_k!} \rho \bar{\lambda}_{jk} Y_j Y_k + \sum_{j,k,l} \frac{N_i}{N_j! N_k! N_l!} \rho^2 \bar{\lambda}_{jkl} Y_j Y_k Y_l, \tag{3.13}$$

where $\bar{\lambda}_{ijk}$ indicates thermally averaged reaction rate in maximally three-body reactions. For the nuclear reaction rates, we mostly adopt the JINA Reaclib (ver 2.0) [76]. With varying nuclear composition by nuclear burning, we calculate the density and temperature in the hydrostatic stellar structure each time step. To follow the nuclear burning process, we solve the nuclear reaction network consistent with stellar structure. By continuing this procedure each time, we obtain the time evolution of bolometric luminosity of accreting neutron stars.

For the reaction network, we adopt an approximate network with 88 nuclei [133], which is based on the calculations of the nucleosynthesis by full reaction networks with ~ 1000 nuclei [134, 135], covering all relevant reactions in the proton-rich area up to Bi. We show our approximate network in Fig. 3.1. We confirm that the approximate network is 150 times faster than the large reaction networks with 897 nuclei [63]. Furthermore, we also confirm that the approximate network reproduces the energy generation rate and hydrogen mass fraction as the ash after the X-ray burst nucleosynthesis with an extensive reaction network with 897 nuclei within 40% errors [133]. Thus, our approximation reaction network is useful in terms of the saving of numerical computation as well as the sufficient reproducibility of the full nuclear reaction network.
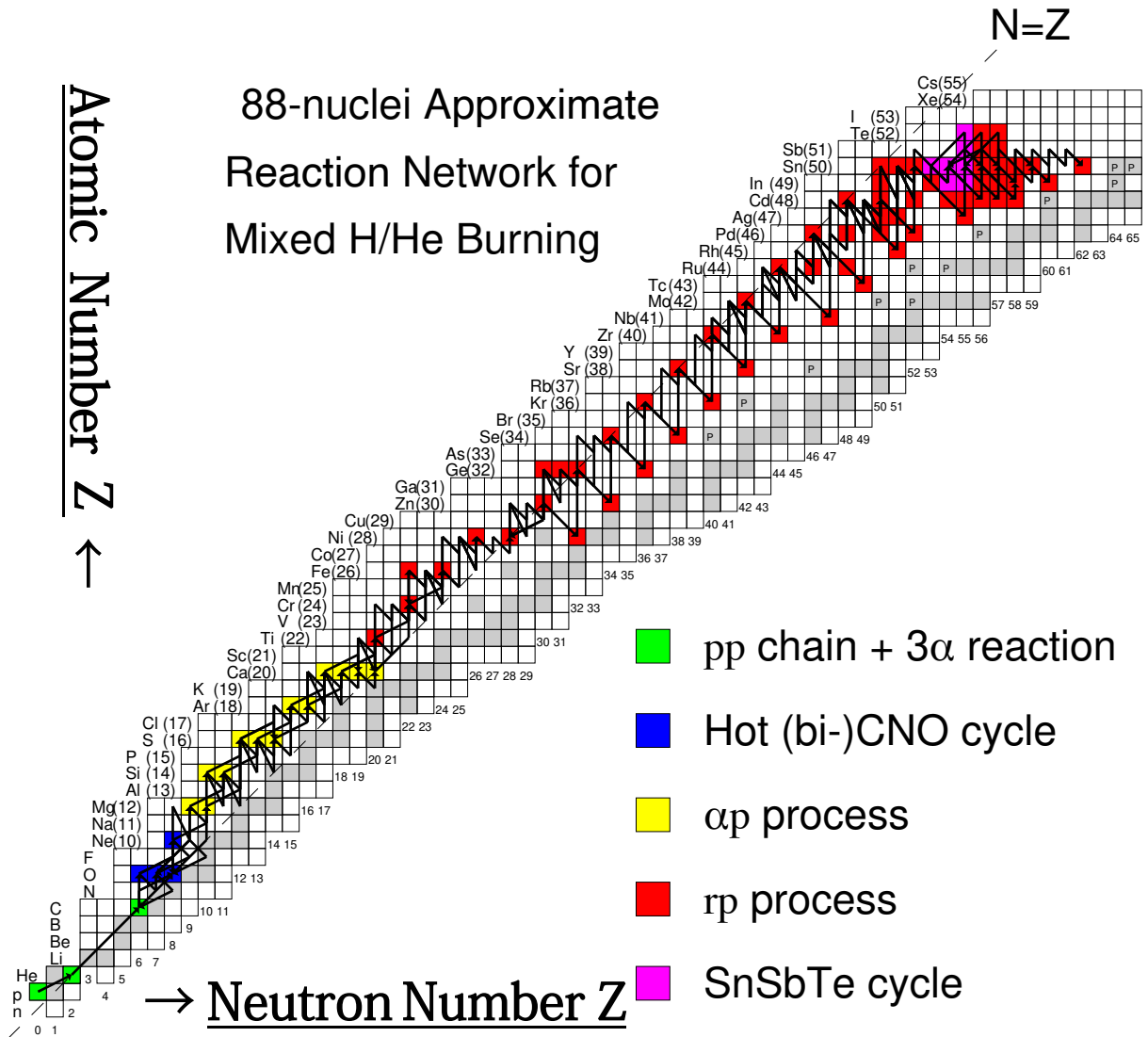
Fig. 3.1: Approximation reaction network with 88 nuclei. Each color of boxes denote the nuclei synthesized from *pp* chain and 3α (green), hot (bi-)CNO reactions (blue), *αp* process (yellow), rp process (red) including SnSbTe cycle (magenta).

Chapter 4

Isolated NS Cooling with Pion Condensation

In this chapter, we discuss the EOS uncertainties on cooling curves of isolated NSs. Most cooling observations can be explained by a minimal cooling scenario, but fast cooling processes are required for some cold NSs. This could become problematic if the symmetry energy in the NS core is quite low enough to prohibit the Direct Urca process. Focusing on this point, we investigate whether low-symmetry-energy EOSs can reproduce cooling observations by considering the pion condensation process. The discussions in this chapter are based on Ref. [136].

4.1   EOS Dependence of the nucleon Direct Urca Process

Before introducing some physical setups, we discuss the possibility of causing the nucleon DU process because it is the most important problem for cold cooling observations. The threshold of proton fraction $Y_p^{e\mathrm{DU}}$ in the DU process via electrons is given in Eq. (1.28), and therefore, whether the DU process occurs or not depends on the EOS. To see the onset density of the DU process, we show the density dependence of Y_p in Fig. 4.1. The high-symmetry-energy EOS, such as the TM1, has high Y_p values even with relatively low-density regions. This implies that the DU process occurs even with low-mass stars. In low-symmetry energy EOS, Y_p is low even with high-density regions. This implies that the DU process occurs with only high mass stars or does not occur. In the case of the Togashi, the DU process is forbidden in NSs. That is why another fast cooling process is required for cold NS observations [137]. In adopted EOSs without pion condensation, the threshold mass is given as follows: $M_{\mathrm{DU}} = 1.35 M_\odot$ for the LS220, $M_{\mathrm{DU}} = 2.06 M_\odot$ for the TM1e, $M_{\mathrm{DU}} = 0.77 M_\odot$ for the TM1, and $M_{\mathrm{DU}} > M_{\max} = 2.21 M_\odot$ for the Togashi. Hence, the higher-M_{DU} value certainly corresponds to the lower symmetry energy, simply L. M_{DU} could be changed because of the softening EOS due to pion condensation, but the effect is negligible in our models.

For the EOS of neutron star matter, Y_p is related to the symmetry energy S. When the symmetry energy is defined as the energy difference between the pure neutron matter and the symmetric nuclear matter as in Eq. (2.2), the β equilibrium condition which we assume in our
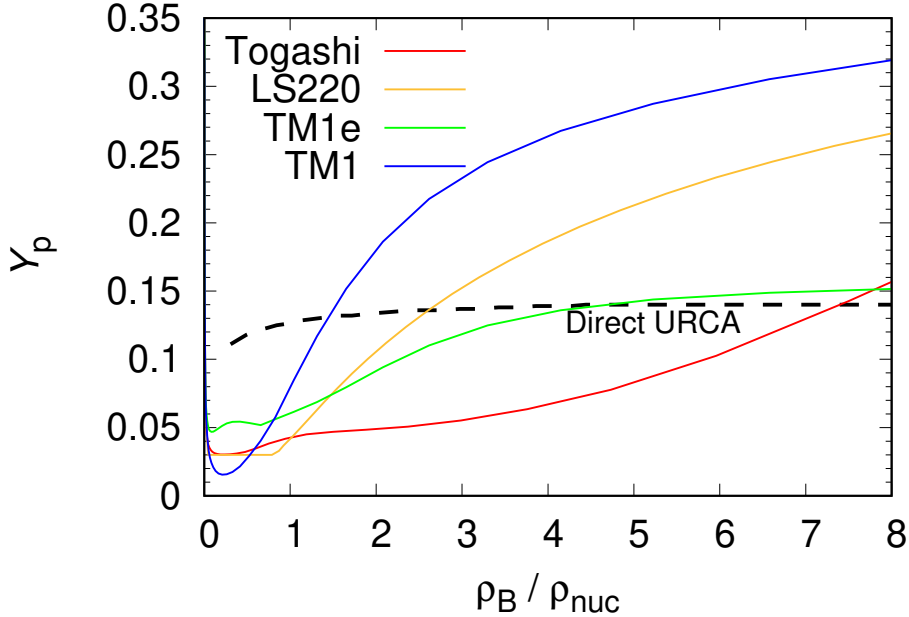
Fig. 4.1: Y_p distribution as a function of the density with adopted EOSs with standard-nuclear matter. The dashed curve indicates the threshold for the DU process.

EOSs can be expressed as

$$\mu_n - \mu_p = 4S\left(1 - 2Y_p\right) = \mu_e = \hbar c \left(3\pi^2 n_{\mathrm{nuc}} u Y_p\right)^{1/3}, \tag{4.1}$$

where μ_n, μ_p, μ_e are chemical potentials of neutrons, protons, and electrons, respectively, $\hbar$ is the Dirac constant, and $u = \rho_{\mathrm{B}}/\rho_{\mathrm{nuc}} = n_{\mathrm{B}}/n_{\mathrm{nuc}}$ is the baryon (number) density normalized by the saturation one. Using the condition for the DU process in Eq. (1.28), we get the condition to cause the DU process for the symmetry energy [138]:

$$S \geq S^{\mathrm{DU}} \simeq 50.7 \left(\frac{u n_{\mathrm{nuc}}}{0.155 \ \mathrm{fm}^{-3}}\right)^{1/3} \ \mathrm{MeV}. \tag{4.2}$$

Here, we neglect muons in Eq. (4.2), but even if muons are also considered, S^{DU} is slightly lower by a factor of a few MeV [137]. We show the symmetry energies as a function of the baryon number density for each EOS in Fig. 4.2, as well as the threshold condition of the DU process for the LS220 EOS with muons. We confirm that Y_p is smaller for the EOS with lower symmetry energy, provided that the baryon number density is the same. At high densities, the Togashi EOS has the lowest symmetry energy while the Shen EOS has the highest. This is consistent with the fact that the symmetry energy slope parameter, L, is small for the Togashi EOS enough to prohibit the DU process even with the maximum mass of 2.21 $M_\odot$ but is large for the Shen EOS, which allows the DU process to occur in low-mass NSs. While the value of L is defined at the saturation density, it can be used as an indicator of symmetry energy at high densities.
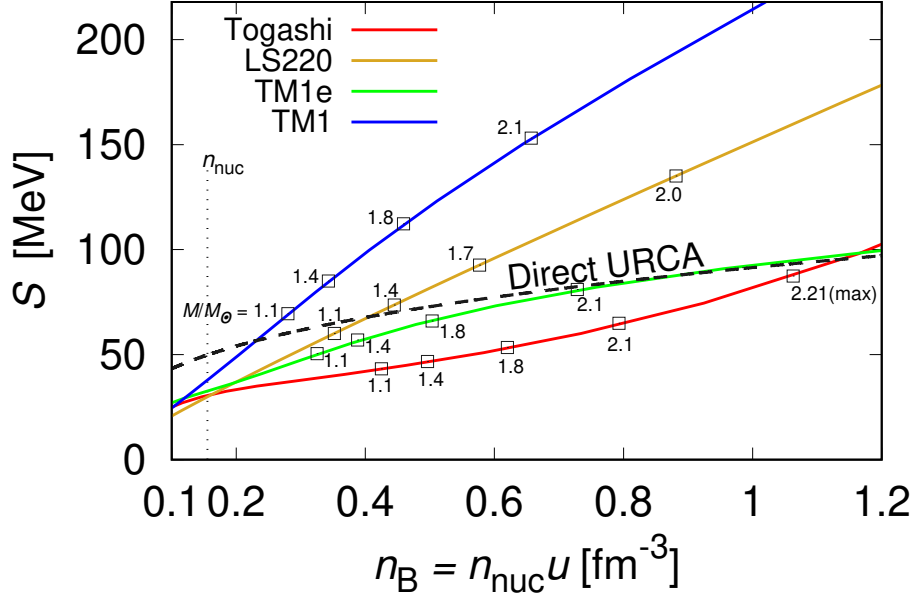
44

Fig. 4.2: Symmetry energies of adopted four EOSs [137]. We adopt the nuclear saturation number density $n_{\mathrm{nuc}} = 0.155$ fm^{-3} and the threshold of the DU process corresponding to the dashed black curves for the LS220 EOS. The symmetry energies at the central baryon number density are plotted for 1.1, 1.4, 1.7, and 2.0 $M_\odot$ models with the LS220 EOS, and 1.1, 1.4, 1.8, and 2.1 $M_\odot$ models with the other EOSs.

4.2 Inputs for Cooling Models

As the slow cooling processes, we consider the neutrino emission of modified Urca, bremsstrahlung of nucleon-nucleon and electron-ion, electron-positron pair creation, photo-neutrino process, and plasmon decay processes as shown in Section 1. In these processes, the modified Urca process and bremsstrahlung are dominant for the slow cooling scenario. These emissivities are approximately $10^{19-21}T_9^8$ erg cm^{-3} s^{-1}, where T_9 is the local temperature in units of 10^9 K. For any slow cooling model, these processes are valid since they are always open. In fast cooling processes, we consider the nucleon DU process for all EOS. The emissivity is given as approximately $10^{27}T_9^6$ erg cm^{-3} s^{-1}, which is much higher than that of slow cooling processes. The EOS dependence of the threshold mass of the DU process has already been discussed in the last subsection. Then, low-symmetry-energy EOSs come up against observational difficulties due to the lack of the DU process. This implies a necessity for another fast cooling process relevant to an exotic state beyond $npe\mu$ in the NS matter. In this work, we consider the pion Urca process arising due to the pion condensation modeled by Ref. [58]. The neutrino emissivity is around $10^{25}T_9^6$ erg cm^{-3} s^{-1} as shown in Fig. 1.7. Although the concrete coefficient of the emissivity is different between π^c and π^0-π^c phase, this pion Urca process is much stronger than slow cooling processes.

Nucleon superfluidity is also important for NS cooling curves since the temperature ($\ll$ 1 MeV) may become lower than the superfluid transition temperature T_{cr}. As the effect of superfluidity on cooling curves, we consider two physical processes (for review, see Ref. [139]):
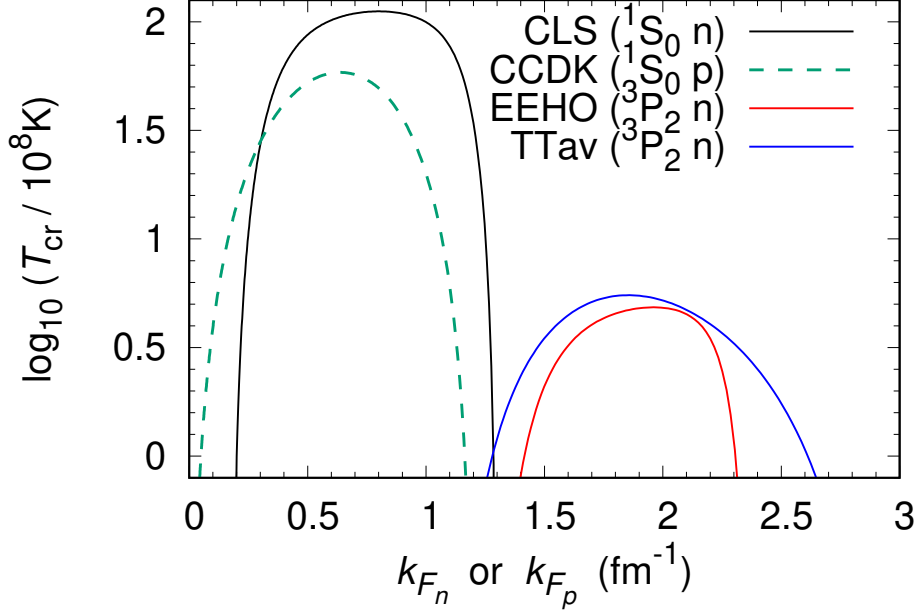
Fig. 4.3: Density Dependence of superfluid transition temperature adopted in this study. The horizontal axis indicates *Fermi*-wave number of neutrons with solid curves, while of protons with dashed curves.

One is the suppression of neutrino emission, specific heat, and thermal conductivity. The other one is the PBF processes. The efficiency of these effects depends on the density dependence of $T_{\rm cr}$, but there are still unknown due to the uncertainties of nuclear interactions. In a lot of nucleon superfluid models (e.g., Ref. [140]), we choose following superfluid models: CLS [141, 142] and CCDK [143] for neutrons and protons $^1S_0$ channels, respectively. For the neutron superfluidity in the $^3P_2$ channel, the DU process and the pion Urca process are greatly suppressed (e.g., Ref. [144]). So, we choose weak and strong pairing models: EEHO [145] and TTav [146], respectively. We show the density dependence of superfluid transition temperature $T_{\rm cr}$ in Fig. 4.3. Compared with EEHO, TTav has a higher superfluid effect in higher-density regions. Hence, pairing effects on cooling curves with high-mass NSs are higher with TTav than EEHO.

NS surface composition is one of the important factors for describing cooling curves (for review, see Ref. [30]). If there are more light elements on the NS surface, the surface temperature is generally higher at the neutrino cooling stage. Meanwhile, this trend becomes the opposite at the photon cooling stage. In this work, we consider two extreme cases: pure Ni surface and pure He surface with $M_{\rm env}/M_{\rm NS} = 10^{-7}$, where $M_{\rm env}$ is the envelope mass and physically up to $\sim 10^{-7}$ times of NS gravitational mass $M_{\rm NS}$ [147].

As temperature observations of isolated NSs, we adopt the data points of 1–19 in Fig. 1.6, whose central compact objects are confirmed to NSs. The data include the observations of PSR J0205+6449 in supernova remnant 3C58 and RX J0007.0+7302 in CTA 1, which are beyond minimal cooling scenario [51]. Hence, these observations are strong evidence for fast cooling processes such as the DU process and pion Urca process. Currently, the only uppers limits of the surface temperature are known for them, so the temperature observations still include large uncertainties. Nevertheless, X-ray observations of NS temperature have recently proceeded

rapidly as a representative of *NICER* (e.g., inhomogeneous surface temperature distributions for PSR J0740+6620 [9, 10]). Thus, if the X-ray observations make progress in the future, we might specify which kind of fast cooling process occurs with the use of the accurately measured temperature data.

4.3   Results

First, we show the simple cooling curves with neither the pion condensation nor nucleon superfluid effects in the upper panel of Fig. 4.4. The cooling curves with the Togashi do not show fast cooling even with $2.1M_\odot$ stars because of low symmetry energy enough to prohibit the DU process. Isolated NSs with the TM1 cause the fast cooling with $M \geq 1.0M_\odot$ because of the high symmetry energy. These two extreme cases cannot explain most cooling observations (see also Ref. [137]). For the TM1e, the DU process occurs with $M = 2.06M_\odot$, but it does not occur with $M = 1.7M_\odot$. The cooling observations between two kinds of cooling curves seem to be on the masses of $(1.7–2.06)M_\odot$, but considering that the DU process is very sensitive to the mass (e.g., see Fig. 9 in Ref. [148]), reproducing such observations without nucleon superfluidity seems to be difficult, with both heavy and light envelope models.

Considering the pion condensation, the cooling curves of all models, shown in the bottom panel of Fig. 4.4, become inconsistent with high-temperature observations due to the strong pion Urca process. Even with the low-mass stars, the pion Urca process is valid since the pion condensation appears with the relatively low density $\rho_\mathrm{B} = 1.6\rho_\mathrm{nuc}$, where the mass is very small ($\lesssim 1M_\odot$). For the Togashi+π, the fast cooling process can lower the surface temperature, whose behavior cannot be seen in the original Togashi, but the pion Urca process is too strong to explain most stars with high-temperature regions.

Next, we show the cooling curves with nucleon superfluidity in Fig. 4.5 and Fig. 4.6. In both the DU process and pion Urca process, the parameter of special importance is the strength of the neutron superfluid model in the $^3P_2$ channel, which significantly contributes to the cooling suppression in theory [149]. In all cooling curves with fast cooling processes, if the neutron superfluid model in the $^3P_2$ channel is stronger, the cooling curves move to higher-temperature regions due to higher cooling suppression. In this work, since we focus on the possibility of pion condensation in NSs, we discuss the cooling curves mainly with the pion condensation.

For the TM1, the DU process occurs with $M_\mathrm{NS} \geq 1.0M_\odot$ as we can see the cooling curves in the top-right panel of Fig. 4.4. For the TM1+π, the pion Urca process occurs, but it seems to be hidden by the stronger DU process as we see the bottom-right panel of Fig. 4.4. Hence, the additional fast cooling process in the exotic matter is required for the high-symmetry-energy EOS. Rather, the pion condensation is not preferred for the high-symmetry-energy EOS because such a model is sensitive to the maximum mass due to the softening effect.

For the TM1e, the fast cooling process derived from the DU process occurs with $M_\mathrm{NS} \geq 2.06M_\odot$. For the TM1e+$\pi$, the pion Urca process also occurs, but it could be hidden by the stronger DU process with $M_\mathrm{NS} \geq 2.06M_\odot$. However, with the masses $M_\mathrm{NS} < 2.06M_\odot$, the pion Urca process is dominant for cooling curves. Considering the nucleon superfluidity, the pion Urca process becomes milder. The EEHO model of neutron superfluidity in the $^3P_2$ channel can be well fitted with cooling observations, but the TTav cannot explain cold NSs because the
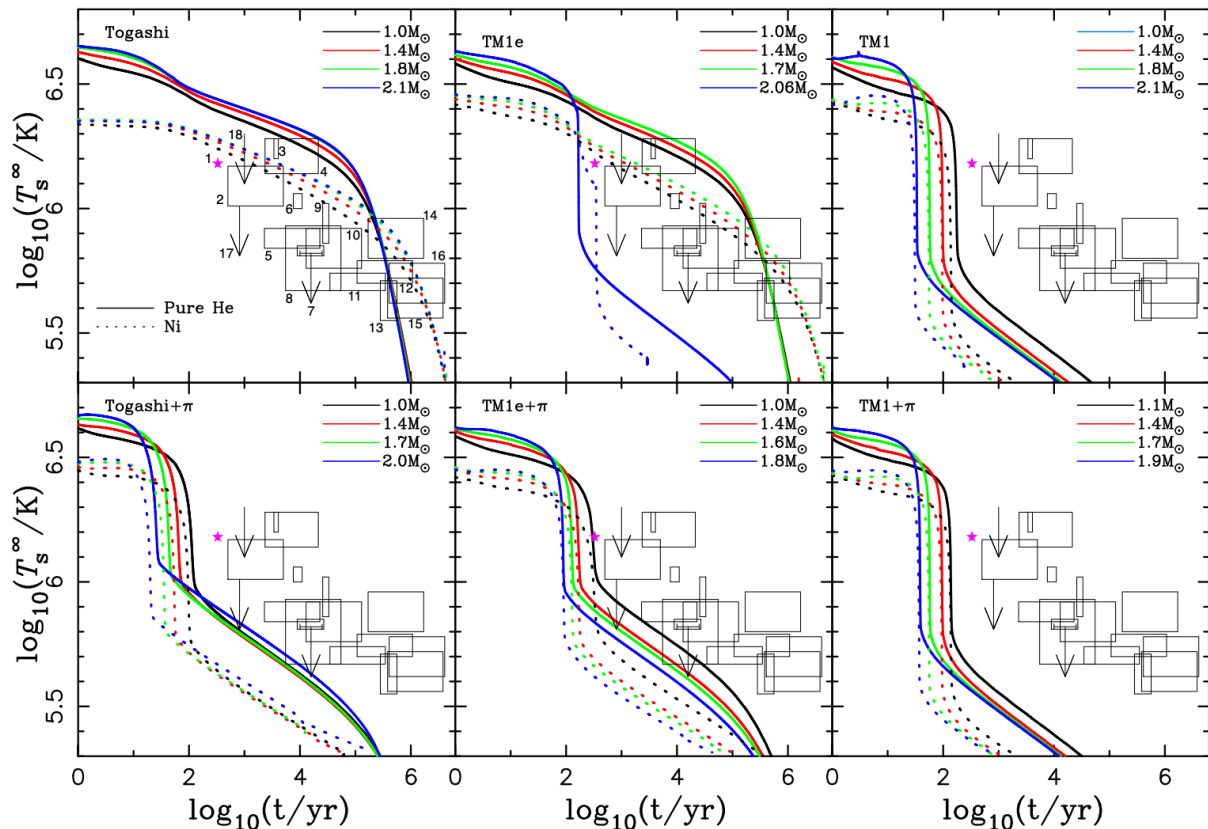
Fig. 4.4: Time evolution of redshifted-surface temperature of isolated NSs, cooling curves, without nucleon superfluidity. Upper panel: pion condensation is not included. The adopted EOSs are as follows: Togashi(left), TM1e(middle), and TM1(right). The pion condensation is considered in lower panel. Solid curves indicates with the He envelope ($M_{env}/M_{NS} = 10^{-7}$) while dotted curves with the Ni envelope. The chosen mass is different from colors of cooling curves. The data of cooling observations (1–18 in left-top panel) are taken from Ref. [148].
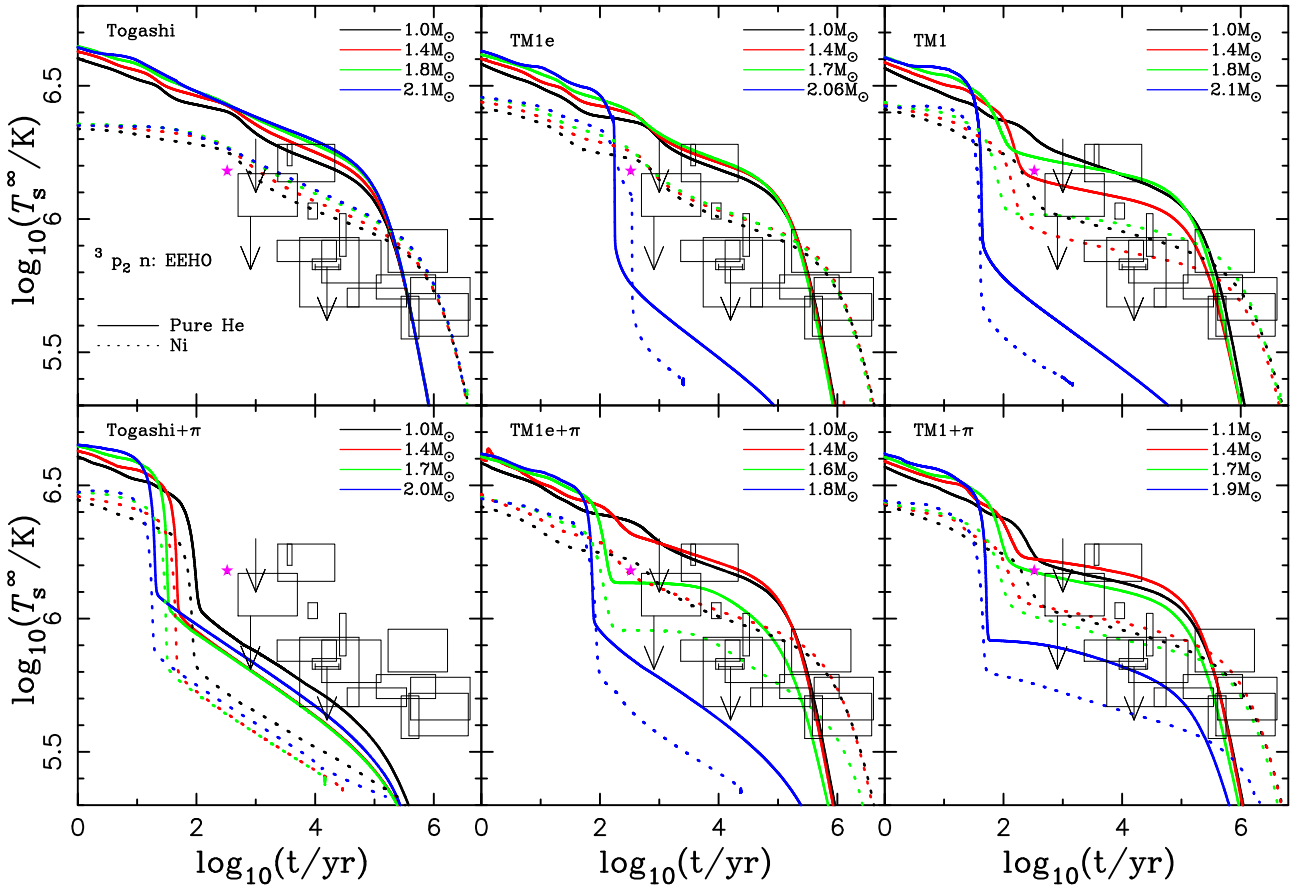
Fig. 4.5: Same as Fig. 4.4, but considering the effect of nucleon superfluidity: CLS, CCDK, and EEHO for neutrons $^1S_0$, protons $^1S_0$, and neutrons $^3P_2$ channels, respectively.
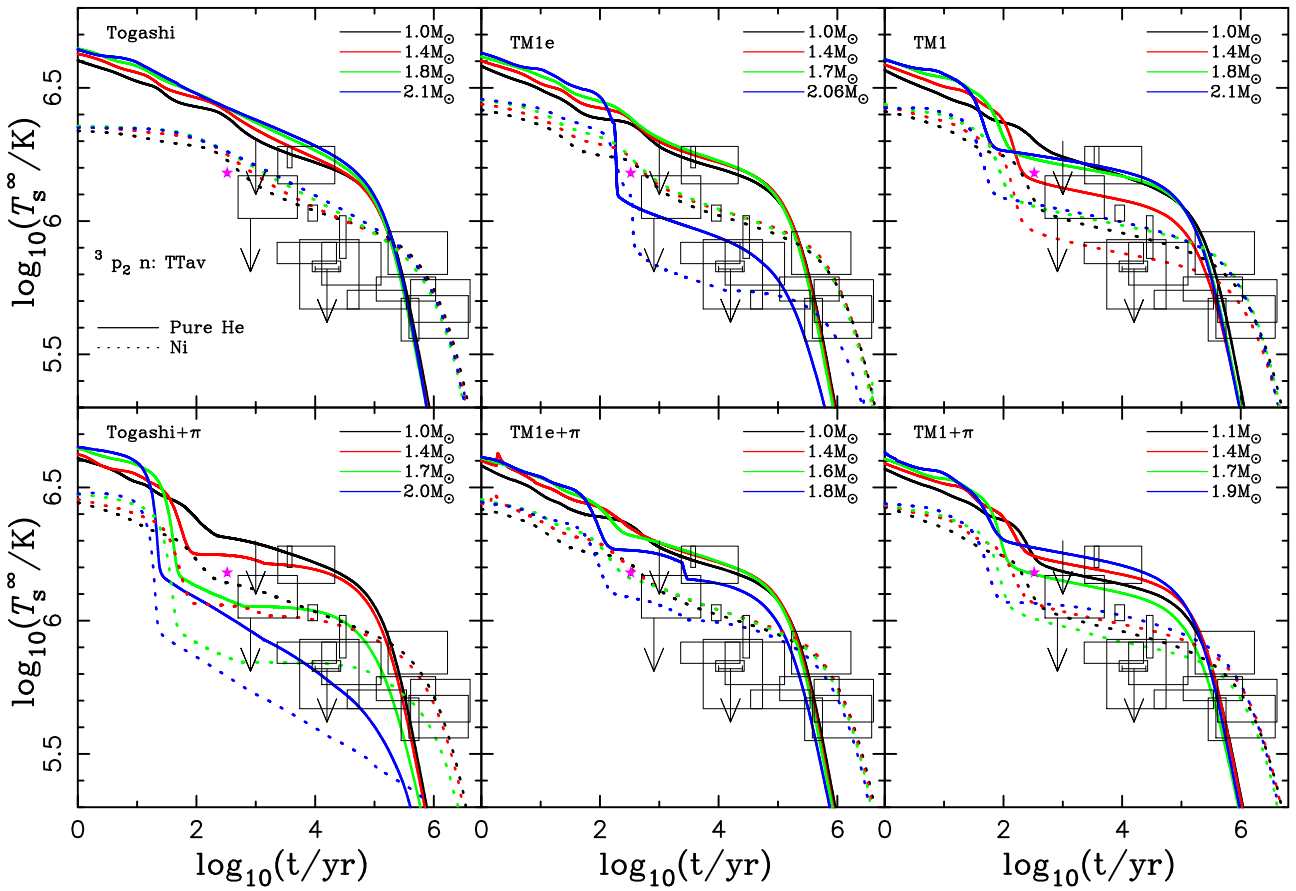
Fig. 4.6: Same as Fig. 4.5, but with the TTav for neutrons $^3P_2$ channel.
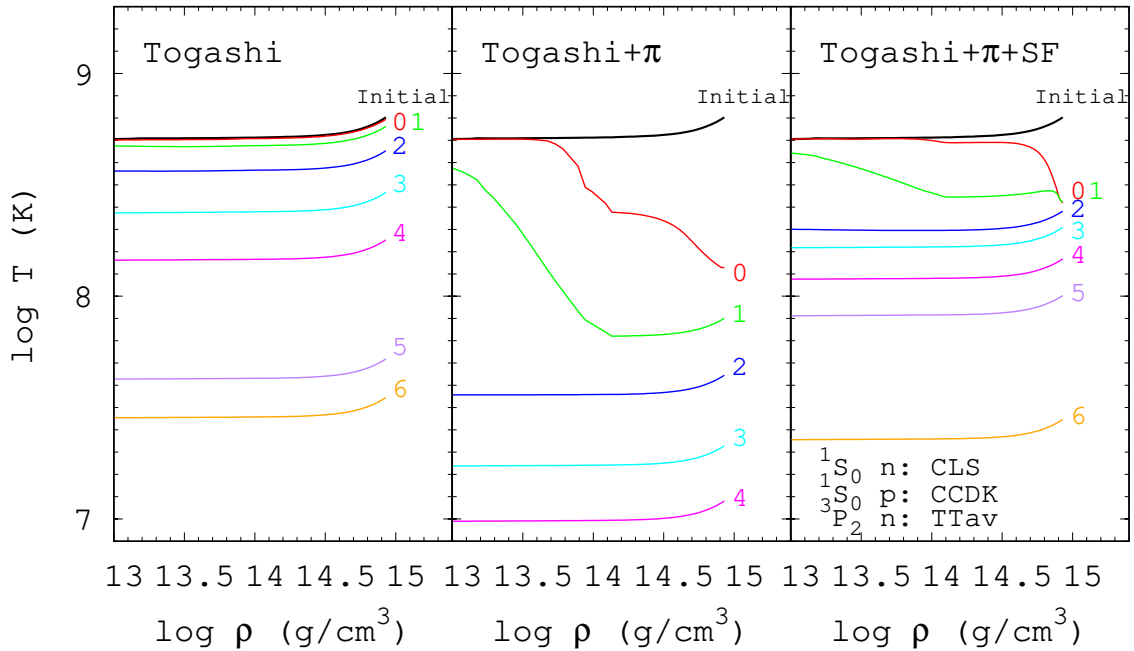
Fig. 4.7: Time evolution of temperature structure (ρ_B-T plane) inside isolated NSs for three models: Togashi, Togashi+π without superfluidity, and Togashi+π with specific kinds of super-fluidity. The number labeled in this figure denotes the age in units of years. We note that initial models are assumed to be isothermal with low temperature $T \simeq 10^{8.7}$ K, which is still valid for $t \gtrsim 1$ yr (e.g., Ref. [137]).

cooling suppression is too strong. Hence, mild superfluid models in the $^3P_2$ channel seem to be better for cooling observations.

For the Togashi+π, the pion Urca process is dominant for cooling curves with any masses. First, we show the evolution of internal temperature in Fig. 4.7. Compared with the Togashi, the core temperature is rapidly cooled due to pion Urca process in the Togashi+π. However, one can see that the nucleon superfluidity greatly suppresses the pion Urca process and keeps the temperature warm. Hence, mild cooling compatible with cooling observations could be realized according to neutron superfluid models.

Next, we explain cooling curves with the Togashi+π and superfluidity. With the EEHO for neutrons $^3P_2$ superfluidity, the cooling suppression is too weak to explain some warm stars. But with the TTav, the cooling observations can be reproduced. Hence, by considering the strong neutrons $^3P_2$ superfluidity within the high-density regions, such a model with low symmetry energy is consistent with cooling observations. Since the low-symmetry-energy EOS is not softened so much in high-density regions $\rho_\mathrm{B} \gg \rho_\mathrm{nuc}$, such a cooling model with pion condensation could be one of the candidates to solve the problem of $2M_\odot$ and cold cooling observations.

As above, if the EOS is different, the efficiency of cooling suppression by nucleon superfluidity is also different. Our results show that the standard-nuclear EOSs with lower symmetry energy need stronger neutron $^3P_2$ superfluidity for cooling observations, not only to reproduce $2M_\odot$ observations as shown in Fig. 2.2. Therefore, the low-symmetry-energy EOS where the DU

process is close could be modified for solving both problems of $2M_\odot$ and cold cooling observations simultaneously by considering the pion condensation and strong neutron superfluidity in the $^3P_2$ channel.

4.4 Concluding Remarks

We studied thermal evolution of isolated NS with constructed EOSs with pion condensation, focusing on the softness of standard-nuclear EOS. As a result, the Togashi+π is in good agreement with the $2M_\odot$ observations and cold cooling observations. The former is based on the softness of EOS with the standard-nuclear matter, which can be associated with the symmetry energy. In high-density regions with $\rho_B \gg \rho_{nuc}$, the EOS with lower symmetry energy does not become softer so much by the pion condensation, and this enables such an EOS to support $2M_\odot$. The latter is connected with fast cooling processes and the neutron superfluidity in the $^3P_2$ channel. The low-symmetry-energy EOS prohibiting the DU process, such as the Togashi, requires another fast cooling process. Then, we considered the pion Urca process as one of the candidates for them. As a result, most cooling observations could be reproduced with the strong neutrons superfluidity in the $^3P_2$ channel. As one of such consistent cooling models, Togashi+π, associated with the TTav neutron $^3P_2$ superfluid model, was present in this thesis.

According to the recent experiment of the Gamow-Teller Giant Resonance in neutron-rich double magic nucleus ^{132}Sn resulted in the following constraint of $\tilde{g}'_{NN} = 0.68 \pm 0.07$ [150]. The value of $\tilde{g}'_{NN}$ is larger than our value of $\tilde{g}' = 0.5$. However, the universality is shown to be against another experiment of the quenching on the Gamow-Teller transitions [151]. Making the universality milder, we finally obtain $\tilde{g}' = 0.5$–0.6 [152], which is lower than $\tilde{g}'_{NN} \simeq 0.68$. Thus, our choice of $\tilde{g}' = 0.5$ would be justified from the nuclear experiment, although it still remains uncertain.

The uncertainties of $\tilde{g}'$ affect cooling curves; if $\tilde{g}'$ is greater, the pion condensation occurs with higher-density regions. The threshold mass of the pion Urca process becomes higher, and therefore only heavier NS cools rapidly (see Ref. [153] for the comparison between $\tilde{g}' = 0.5$ and 0.6). Hence, it is worth making other EOSs with different $\tilde{g}'$ and checking them with temperature observations. Nevertheless, unless the pion condensation is prohibited with any mass due to being larger $\tilde{g}'$, the cooling scenario of low-symmetry-energy EOSs would not be changed, considering the suppression of neutrino emissivities by strong neutron superfluidity.

Chapter 5

Quiescent Luminosities of Accreting NSs with Pion Condensation

In this chapter, we discuss the EOS uncertainties on quiescent luminosities of accreting NSs. As with temperature observations of isolated NSs, several accreting NSs are cold enough to require any fast cooling process. We investigate the consistency with the observations of quiescent luminosities for several EOSs including the pion condensation. Furthermore, we also compare our models with the extraordinarily hot soft X-ray transient RX J0812.4−3114. The discussions in this chapter are based on Ref. [154].

5.1   Inputs for Heating-Cooling Models

The setup of NS EOS, nucleon superfluid models, neutrino cooling processes, and surface compositions are entirely the same as those in Section 4.1. The only difference from the previous Section is that an NS is often accreting from its companion in a system of a low-mass X-ray binary. Thus, in addition to the cooling processes, since accreting NS has a heat source due to the accretion from its companion, one should consider the heating processes caused by the accretion, such as the gravitational energy release (compressional heating) caused by the compression of the matter falling on the NS crust surface, and heating process occurring in the crust. However, in the steady-state accreting NSs, the former is appropriate not to work [59]. Hence, we should consider the only deep crustal healing process, which is the non-equilibrium nuclear reactions such as the electron capture, neutron emission, and pycnonuclear reactions. The deep crustal heating has the following form [155]:

$$Q_i = 6.03 \times \dot{M} q_i 10^{43} \text{ erg s}^{-1}, \tag{5.1}$$

where q_i is the effective heat per nucleon on the i-th reaction surface. For each reaction rate, we adopt Ref. [156] as the heating rate where the initial compositions of the nuclear burning ashes are fixed to be ^{56}Fe (for detail, see table A.3 reference therein). The total released energy is around 1.4 MeV per one accreted nucleon in this model.

53

5.2 Results

5.2.1 EOS dependence of Quiescent Luminosities

One important tool of analysis is the quiescent luminosity(L_γ^∞) vs. time-averaged mass accretion rate ($\langle \dot{M} \rangle$) diagram, in which currently, a few (~ 35) observed accreting NSs are located [67], which We take as the data of quiescent luminosities. Using the specified EOSs constructed in Section 2 except LS220+π EOS for which the maximum mass is less than $2.0 M_\odot$ and TM1+π EOS as the TM1 EOS operates DU process at any mass and we don't need to include other fast cooling processes such as pion condensation, the thermal evolution of accreting NSs are calculated.

Fig. 5.1 shows the redshifted quiescent luminosities of NSs in SXRTs as a function of time-averaged mass accretion rate. For LS220 EOS, since the DU threshold operate at $M_{DU} \simeq 1.35 M_\odot$, the theoretical curves lie in low-luminosity regions in the panel with $M > 1.4 M_\odot$ that the observations can't be explained well. We need to include the effect of superfluidity to suppress the fast cooling due to the DU process. We see that Togashi EOS cannot explain the whole range of the estimated values of L_q^∞ and $\langle \dot{M} \rangle$ simultaneously. Because the DU process is forbidden for Togashi EOS, the quiescent luminosities are high with a fixed mass accretion rate. It is necessary to include other fast cooling in the core of Togashi EOS. For Togashi+π EOS, as the pion DU threshold is $0.3 M_\odot$, the NSs cool fast that the curves with $M \geq 1.0 M_\odot$ are located in the lower panel in order to explain the observations well, we need include the effect of superfluidity. The case of TM1 EOS is similar to Togashi+π EOS, as the DU process operates at $0.77 M_\odot$, the NSs cool too fast that the curves can't explain the observations even with $1.0 M_\odot$ NS. While for TM1e EOS, the DU process operates at $M_{DU} = 2.06 M_\odot$, we also need to include other fast cooling as pion condensation to fit the observations as seen in the middle of the bottom panel of Fig. 5.1. For TM1e+π EOS, as the pion DU threshold is $0.66 M_\odot$, the results cannot explain the observations with high luminosities, which indicates that the superfluidity is also needed for TM1e+π EOS to suppress the fast cooling due to pion condensation.

In Fig. 5.2, we examine the effects of superfluidity on the $L_\gamma^\infty - \dot{M}$ curves. The superfluidity models of CLS for neutron $^1S_0$, CCDK for proton $^1S_0$, EEHO for neutron $^3P_2$ are adopted, and the critical temperature of the models can be found in Fig. 4.3. Here the thermal evolution of accreting NSs using the same model as in Fig. 5.1 but with the effect of superfluidity. As the quiescent luminosities with Togashi and TM1e EOSs have already been high in Fig. 5.1, we don't include these two EOSs in Fig. 5.2. We note that the observations could potentially be explained regarding the effect of superfluidity. However, the impact of superfluidity adopted in the figure seems a little weak for LS220 and Togashi+π EOS; as one can see from Fig. 5.2, for LS220 EOS, the location of the curves with $M \geq 1.7 M_\odot$ change a little compared with that in Fig. 5.1, while for Togashi+π EOS, only the curves with $1.0 M_\odot$ change significantly to fit the high luminosities observations, for $M \geq 1.4 M_\odot$, the curves are not changed compared with that in Fig. 5.1. Due to this problem, Fig. 5.3 shows the curves with a stronger neutron $^3P_2$ model with the TTav. As can be seen in Fig. 4.2, TTav has a wider superfluid effect in high-density regions than the EEHO model, as a result, the former would have a stronger effect than the latter, and the curves in Fig. 5.3 are enhanced compared with Fig. 5.2. For LS220 and
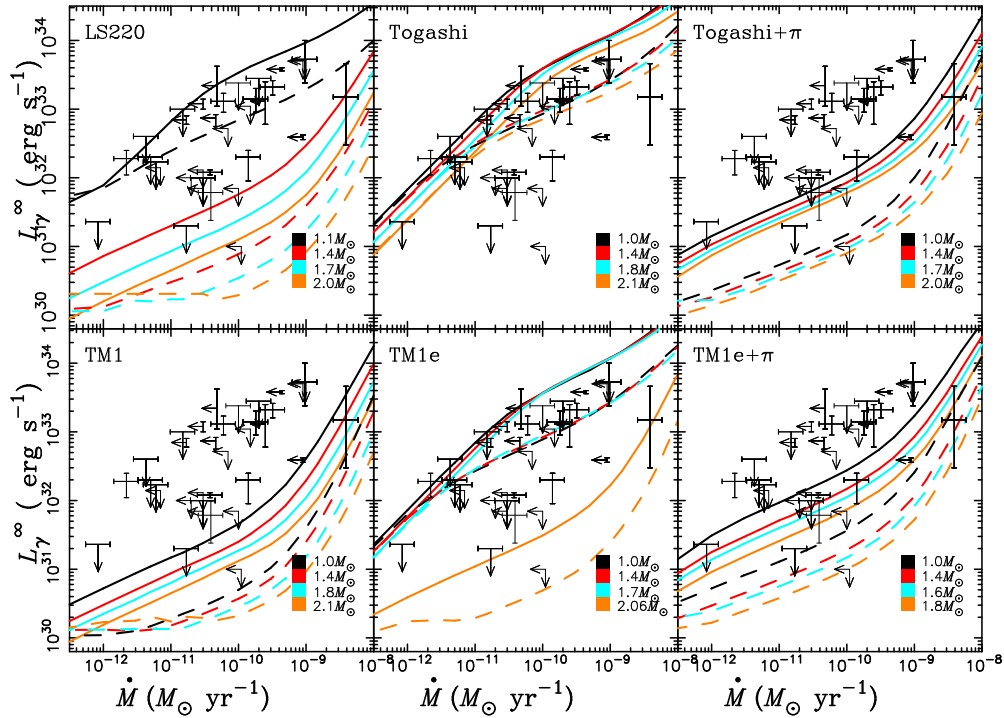
Fig. 5.1: Quiescent luminosities of SXRTs as functions of time-average mass accretion rates, without nucleon superfluidity. Different panels indicate the models with different EOSs. The solid curves indicate the pure He envelope ($\Delta M/M = 10^{-7}$), while the dashed curves indicate the pure Ni envelope. Different masses are marked by color. The error bars in each panel are taken from Table 2 of Ref. [67].

Togashi+π EOSs, most of the observations can be fitted well except the coldest one, but the suppression of $^3P_2$ model is too strong for TM1 and TM1e+π EOSs, the quiescent luminosity is too high for a fixed accretion rate.

In the models described above, large changes in the quiescent luminosities come from adopting different EOSs, which determine the fast cooling process and superfluidity models. In Fig. 5.4, we show the temperature as a function of density for Togashi EOS in three cases as an example. Without nucleon superfluidity, the thermal structure of the models with the Togashi EOS ($1.4M_\odot$) shows that the DU process doesn't operate in the NS core. Since this case corresponds to the slow cooling, the heating curves with Togashi EOS cannot explain the whole range of the observations in Fig. 5.1. While for Togashi+π EOS in the middle panel, the pion DU process works in the NS, and the core temperature drops rapidly at the first 0-100 years, resulting in a low temperature at a steady state. As a result, the $L_\gamma^\infty - \dot{M}$ curves with Togashi+π EOS locate too low to fit the observations. The right panel of Fig. 5.4 shows the effect of superfluidity on the thermal structure of accreting NS with Togashi+π EOS; the neutrons superfluidity suppresses the rapid cooling compared with the middle panel so that the observations can be explained well with Togashi+π EOS in Fig. 5.3.

From Figs. 5.1, 5.2 and 5.3, we conclude that for LS220 and TM1 EOSs, which have low DU threshold, one can fit the observations well with those EOSs by considering proper superfluidity models besides different envelope composition and a range of masses. While for the EOSs such as Togashi and TM1e, for which the DU threshold is too high or forbidden, we can include the other fast cooling process such as pion condensation in the core of NS to operate the fast cooling process, the models with Togashi+π and TM1e+π EOSs can also explain the observations well by choosing proper superfluid models.

5.2.2 Thermal luminosity of RX J0812.4–3114 with minimal cooling

The quiescent luminosity of Be/X-ray pulsar (BeXRP) RX J0812.4–3114 has been estimated as $L_q^\infty \sim (0.6 - 3) \times 10^{33}$ erg s^{-1}, and its time-average mass accretion rate is estimated as $\langle \dot{M} \rangle \sim (4 - 15) \times 10^{-12}$ M$_\odot$ yr^{-1} [68]. It has been shown that the thermal luminosity of RX J0812.4–3114 is too high to be explained by the standard deep crustal heating model. There are two possible explanations: RX J0812.4–3114 may contain a low-mass NS with minimum cooling, or the system may be young enough that the NS is still hot from supernova explosion [68]. We verify the former assumption based on our work. In the minimal cooling scenario, the fast cooling from any DU process will not be included. So we turn off the DU process for LS220 and TM1 EOSs, and the pion DU process for Togashi+π and TM1e+π EOSs. For the effect of superfluidity, we choose the same model as used in Fig. 5.2: CLS for neutron $^1S_0$, CCDK for proton $^1S_0$ and EEHO for neutron $^3P_2$. The results can be found in Fig. 5.5; it is shown that the minimal cooling with small mass NS ($< 1M_\odot$) can probably fit the lower limit of the high thermal luminosity of RX J0812.4–3114, no matter for LS220, TM1, TM1e+π or Togashi+π EOSs. Our results qualitatively agree with Ref. [68], while the quantitative differences may be caused by the different microphysics input. The upper limit luminosity of RX J0812.4–3114 can't be fitted by the standard deep crustal heating model, which indicates that the NS in RX J0812.4–3114 is too hot. One possible way to explain the upper limit luminosity of RX
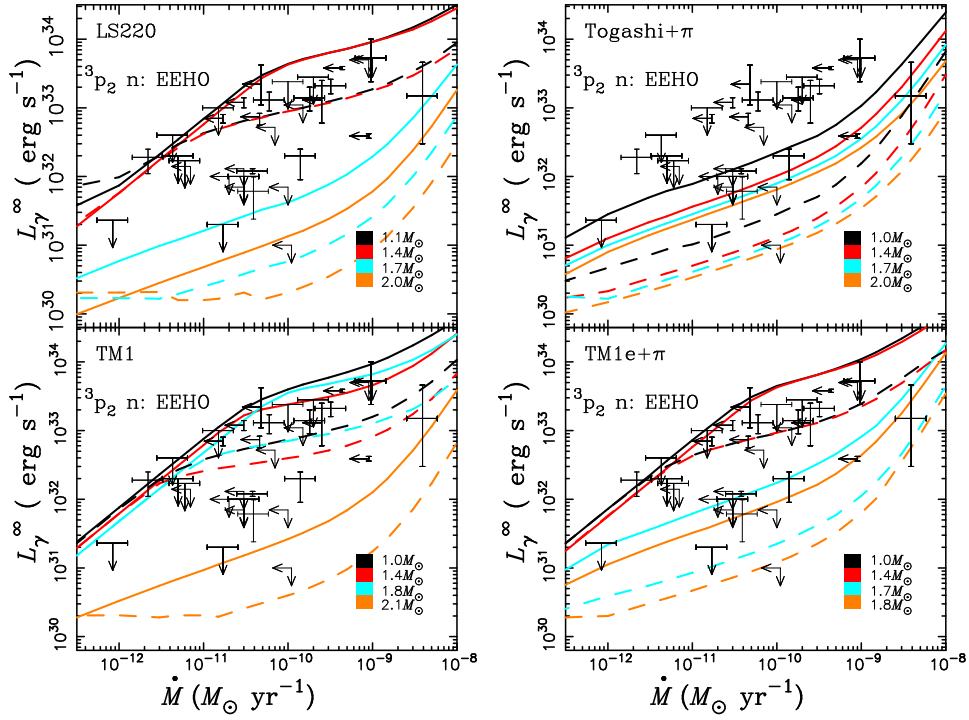
Fig. 5.2: Quiescent luminosities of SXRTs as functions of time-average mass accretion rates, but considering the effect of nucleon superfluidity. The superfluidity models are as follows: CLS for neutron $^1S_0$, CCDK for proton $^1S_0$, EEHO for neutron $^3P_2$, the critical temperature for the models are shown in Fig. 4.3.
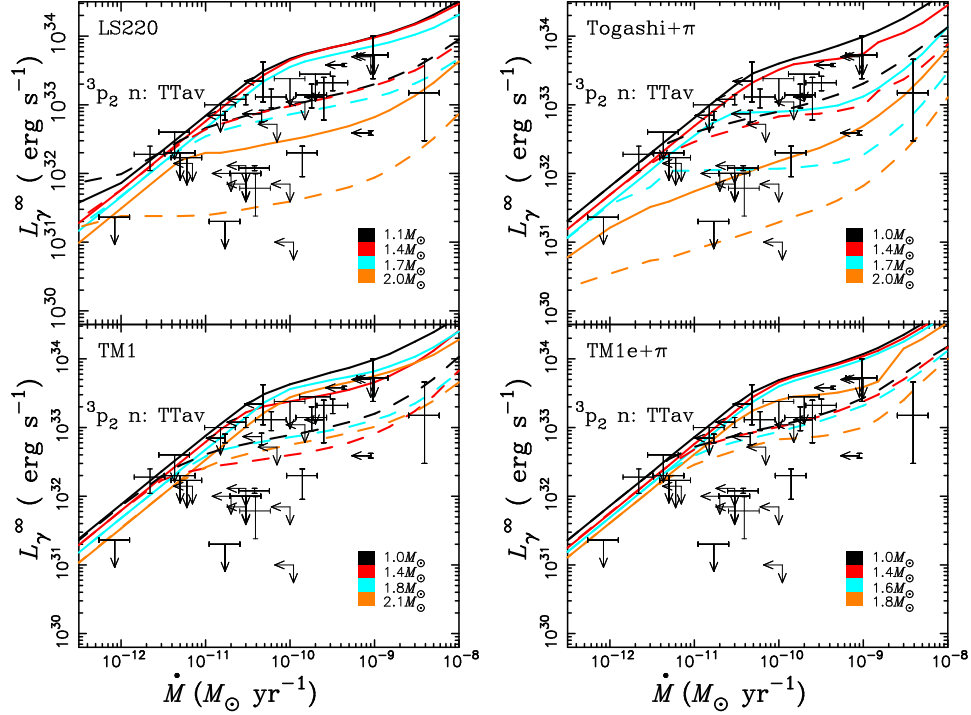
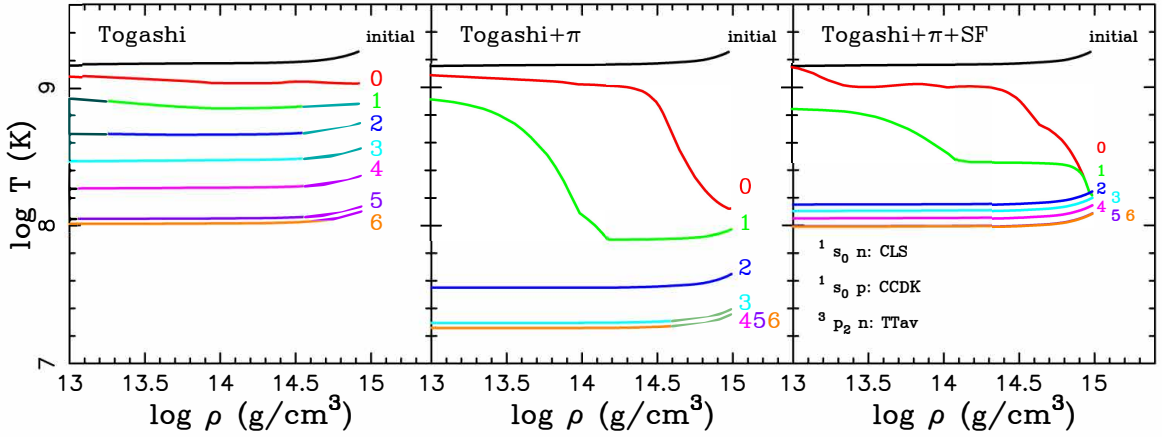Fig. 5.3: The same as Fig. 5.2 but with different neutron $^3P_2$ superfluidity model as TTav.

Fig. 5.4: Time evolution of local temperature towards the steady-state of NSs. The left and middle panels show the results for Togashi, Togashi+π EOSs with $1.4M_\odot$, respectively. The right panel is the same as the middle panel but includes the effect of superfluidity, which we marked as Togashi+π+SF. The accretion rate is set as 1×10^{-10} $M_\odot$ yr^{-1} and the surface composition is pure He for the calculations. The numerals attached indicate the ages of log t (yr).

J0812.4–3114 is to consider that it is still hot from a supernova explosion as the previous work mentioned [68]. Another possible way is that there are other heating mechanisms in addition to standard deep crustal heating in RX J0812.4–3114. We need further observations to understand more about the physics in RX J0812.4–3114.

5.3   Concluding Remarks

Motivated by the cooling of NS is slow with Togashi EOS, the DU threshold is high for TM1e EOSs, and the recent availability of more stringent restrictions on the EOSs of NS provided by GW170817. We have computed the quiescent luminosities of accreting NSs in this work with different EOSs (LS220, TM1, TM1e, Togashi, Togashi+π, and TM1e+π) by using stellar evolutionary calculations. As the DU threshold is low for LS220 ($M_{DU} \approx 1.35 M_{\odot}$) and TM1 ($M_{DU} \approx 0.77 M_{\odot}$) EOSs, we can simulate the quiescent luminosity with those two EOSs to fit the observations well by considering the effect of superfluidity besides the different surface composition and different masses. However, for Togashi and TM1e EOSs, their DU threshold is forbidden or too high; as a result, the steady luminosity is too high with these two EOSs compared with LS220 and TM1 EOSs. To fit the observations well, we include pion condensation with them, named Togashi+π and TM1e+π, respectively. As the pion DU threshold is $0.3 M_{\odot}$ for Togashi+π EOS and $0.66 M_{\odot}$ for TM1e+π EOS, the simulations of quiescent luminosities with those two EOSs are low, and we can improve them also by choosing a proper superfluid model. Besides, the thermal luminosity of RX J0812.4–3114 has been compared with our theoretical model under minimal cooling; we find that the thermal luminosity of RX J0812.4–3114 can be explained with low mass NS ($< 1 M_{\odot}$) under minimal cooling, which qualitatively agrees with those in Ref. [68]. However, to explain the upper limit of the high thermal luminosity of RX J0812.4–3114, another heating mechanism besides standard deep crustal heating should be considered. For example, the effect of unstable nuclear burning may make the NS warm [133, 157, 88], there are few works on the effect of an X-ray burst on the quiescent luminosity of accreting NSs. Another possible mechanism is related to a magnetic field, as RX J0812.4–3114 is a BeXRP which usually includes a highly magnetized NS. The high magnetic field may affect the accretion and heating process compared with low-mass X-ray binaries and may make the NS warm [158, 159, 126]. It is also possible that the NS in RX J0812.4–3114 is still hot from a supernova explosion as the previous work proposed [68].
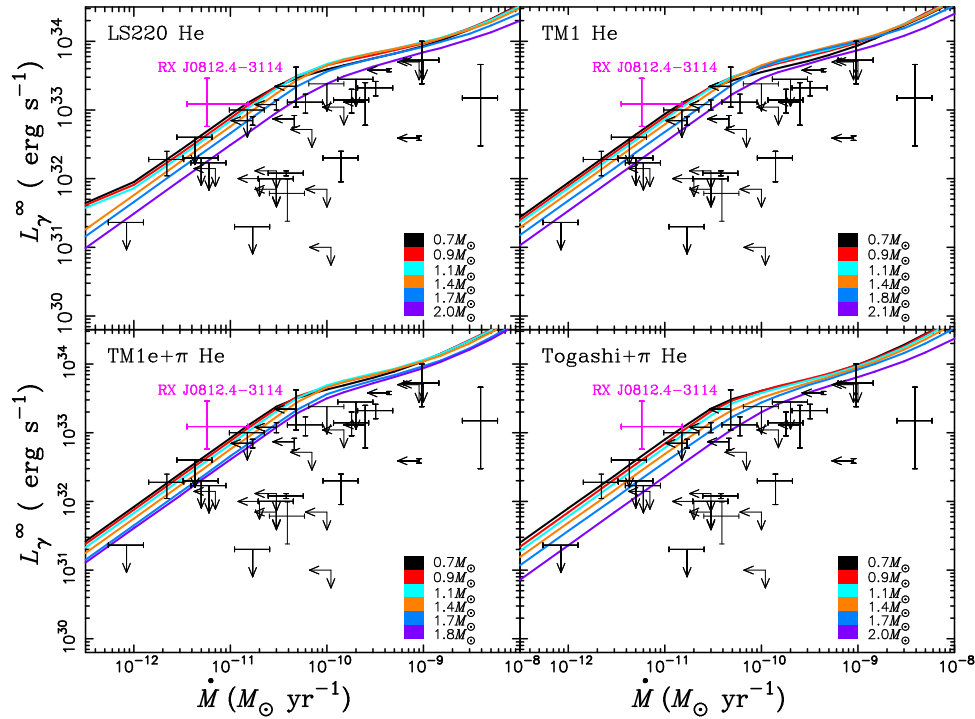
Fig. 5.5: The same as Fig. 5.2 but with minimal cooling for which the DU process are turned off. The pink error indicate the observation of RX J0812.4–3114.

Chapter 6

Type-I X-ray Burst with NS Microphysics

In this chapter, we discuss the effects of NS physics on Type-I X-ray bursts. There are few theoretical studies to consider the physics of NSs in X-ray bursts, though the importance of NS microphysics has been widely recognized under simple burst models. We present the *full* consistent burst models where whole NS regions are covered. Using them, we discuss the EOS and mass dependences on burst light curves and their characterized burst parameters. We also investigate the consistency with the *Clocked* burster GS 1826–24 and final products after X-ray burst nucleosynthesis. Most of the discussions in this chapter are based on Ref. [160].

6.1 Input Physics

We adopt the Togashi, LS220, TM1e, and TM1 without pion condensation present in Section 2. The uncertainty of radius deduced from EOS affects the amount of fuel in outburst [93], and the strength of the heating and cooling which occur in the NS crust and core. As the heating process inside NS, we consider compressional and crustal heating processes modeled by Ref. [155] as introduced in Section 5. There are some developed versions of crustal heating models (e.g., Ref. [161]), but according to Ref. [156], the heating rate of Ref. [155] is shown to be quite a reasonable estimate. For the cooling process inside NS, the neutrino emission occurring inside NS through weak interactions should be considered. As we introduce in Section 3, there are many kinds of neutrino emission processes, including nucleon superfluid effect on thermal evolution of NSs (for reviews, see Refs. [43, 139]), but for simplicity, we adopt the slow neutrino cooling processes including the modified Urca process and bremsstrahlung (but we consider the direct Urca (DU) process in Sec 6.3.4.). For LS220 and TM1 EOSs, since their values of nucleonic symmetry energy are high enough to cause the DU process, as we see in Figs. 4.1 and 4.2, such a fast cooling process occurs with relatively low-mass stars (e.g., Refs. [148, 137]). Moreover, the recent experiment to measure the neutron skin thickness of ^{208}Pb, the updated lead Radius EXperiment (PREX-2), resulted in the symmetry-energy value of the slope parameter $L = (106 \pm 37)$ MeV [16], which is quite large against other experiments and observations [162], the DU process may work even for low-mass stars with $M_{\rm NS} \sim M_\odot$ [163]. In this work, however, to focus on the difference of the radius as the EOS dependence, we do not

incorporate it except Sec 6.3.4.

6.2 Initial Models for Burst Calculation

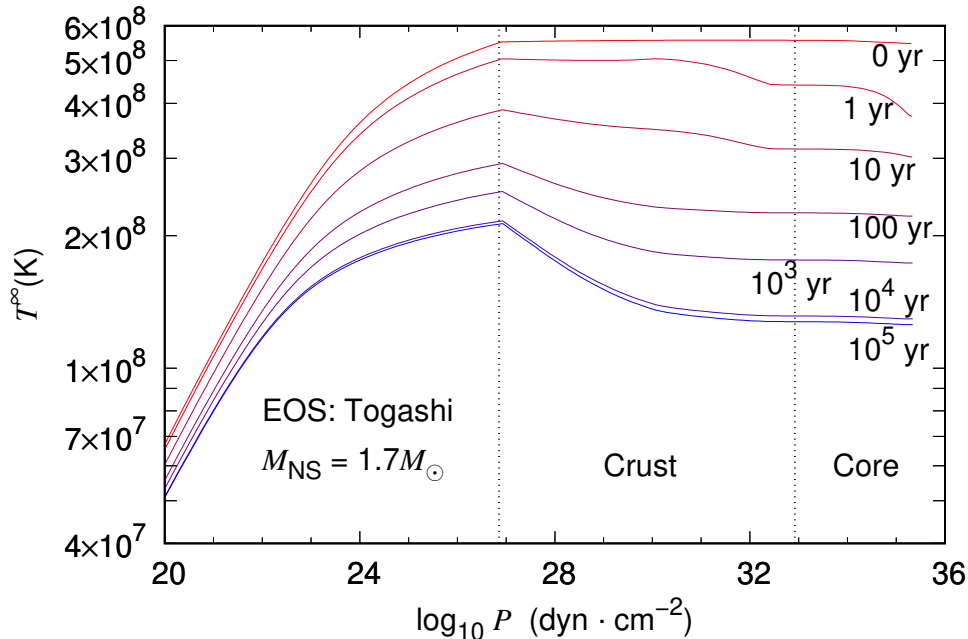### 6.2.1 Preburst evolution without nuclear burning

Fig. 6.1: The redshifted temperature for a 1.7 $M_\odot$ NS with the Togashi EOS with the mass accretion of $\dot{M}_{-9} = 2.5$. The time snapshots from 0 yr to 10^5 yr are plotted, where the initial state satisfies the isothermal condition. The effect of nuclear heating is ignored. Dotted lines indicate the pressure $P \simeq 7 \times 10^{26}$ dyn cm^{-2} on the crust surface and $P \simeq 8 \times 10^{32}$ dyn cm^{-2}, which corresponds to the nuclear saturation density $(= 2.66 \times 10^{14}$ g cm$^{-3})$. We note that the compressional heating works unlike Section 5.

To develop the initial conditions for the X-ray-burst simulations, we first calculate the thermal evolution of accreting NSs without nuclear burning from the isothermal state. The method for calculations is mostly the same as Section 5, but we also consider the gravitational energy release, that is, non-homologous and homologous compressional heating corresponding to Eqs. (3.5) and (3.6), respectively, because the bursting NSs are in the outburst state. In Fig. 6.1, we show the time evolution of the redshifted temperature without nuclear burning from 0 yr at the beginning of the calculation to 10^5 yr at the end of the pre-evolution. We adopt the mass accretion rate of $\dot{M}_{-9} = 2.5$ for 1.7 $M_\odot$ stars with the Togashi EOS, where $\dot{M}_{-9}$ is the accretion rate normalized by 10^{-9} $M_\odot$ yr^{-1}. The initial state at $t = 0$ yr is constructed to satisfy the isothermal condition.

We cover the entire region from the core to the accreted layers in the numerical calculation. Although some previous thermal evolution models of accreting NSs fix the temperature in the core (e.g., [164]), we do not keep it fixed. Due to the neutrino emission from the crust and core of the NS, the temperature decreases with time. However, the temperature structure settles in the steady-state at $t \simeq 10^5$ yr because the effect of crustal heating accompanying the mass accretion
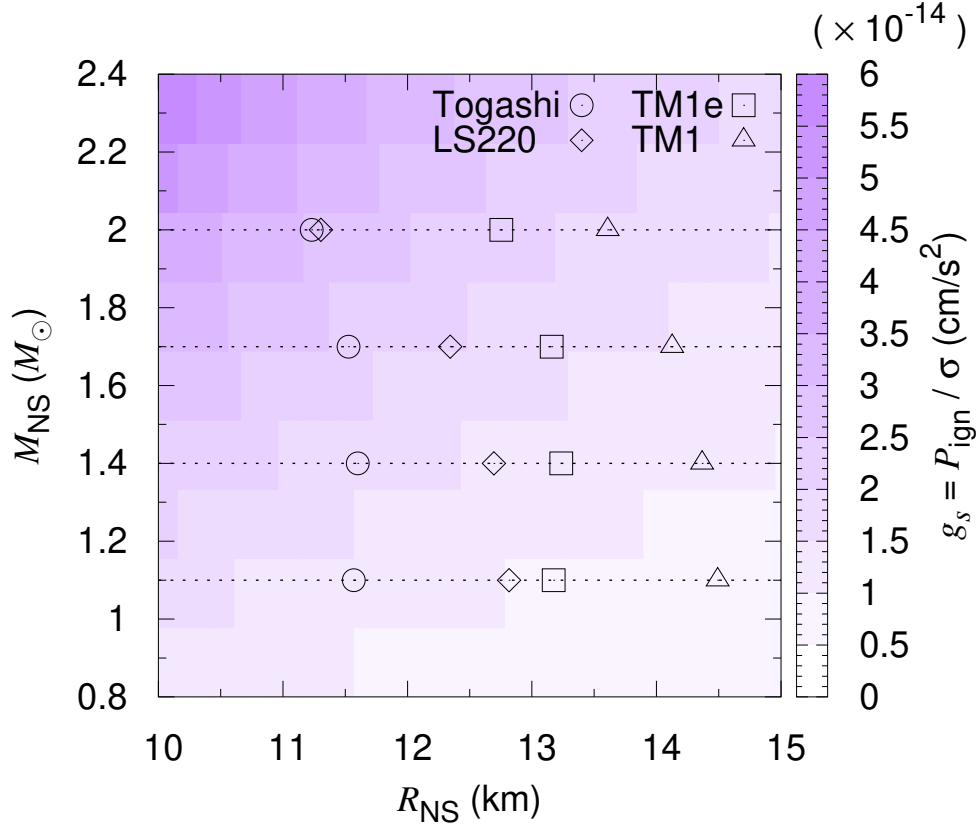
Fig. 6.2: The surface gravity acceleration g_s on the mass-radius plane, based on the (one-zone) shell-flash model [93]. The symbols indicate the values of our multizone X-ray-burst calculations.

in the crust regions becomes significant. Note that we find that the temperature structure bends around $P \sim 10^{27}$ dyn cm^{-2}, which appears to be due to the switching of EOSs around the crust surface. We use such a quiescent NS model with the gravitational energy release as the initial model for X-ray-burst calculation.

6.2.2   The surface gravity and the ignition condition

We consider the physical conditions for the ignition of nuclear burning in the accreting layers on the surface of an NS. The gravitational acceleration at the NS surface g_s is useful to measure the strength of the surface gravity. The balance between g_s and the pressure due to the mass accretion determines the ignition condition. We focus on g_s and P_{ign} (the pressure at the time of nuclear ignition) as critical quantities for the burst light curves.

We can derive a relationship between g_s and P_{ign} based on a simplified one-zone burst condition, called the shell-flashed model, adopted in our previous studies [165, 135]. This model approximately reproduces the structure of accretion layers during the flash, where the position of the NS shell is much lower than the pressure scale height due to the strong gravity [166, 93]. The ignition pressure remains constant during the flash and is derived from the hydrostatic equation,

$$P_{ign} = g_s \sigma, \quad g_s = \frac{GM_{NS}}{R_{NS}^2} \left(1 - \frac{2GM_{NS}}{R_{NS}c^2} \right)^{-1/2}, \tag{6.1}$$
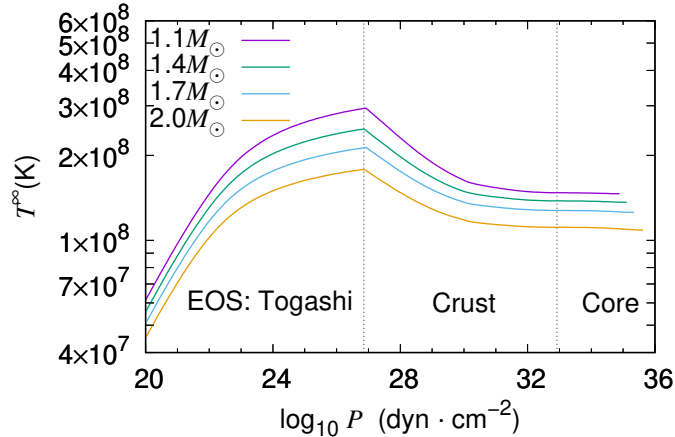
Fig. 6.3: The redshifted temperature structure in the steady state with $M_{\mathrm{NS}} = 1.1, 1.4, 1.7,$ and, $2.0\ M_{\odot}$, assuming the Togashi EOS and $\dot{M}_{-9} = 2.5$. Same as Fig. 6.1 for dotted lines.

where σ is the column depth. The effect of general relativity is considered in g_{s}; G is the gravitational constant, and c is the speed of light. In this one-zone framework, we assume all fuel in the shell is consumed in one burst event. Thus, using the energy generation density of nuclear burning (Q_{nuc}), the burst energy E_b^{1z} is expressed as

$$E_b^{1z} = 4\pi R_{\mathrm{NS}}^2 \sigma Q_{\mathrm{nuc}} \left(1 + z_g\right)\ . \tag{6.2}$$

A lower $R_{\mathrm{NS}}^2 \left(1 + z_g\right)\sigma$ with a compact NS causes a lower E_b^{1z} when we consider only the effect of surface gravity ignoring other processes, e.g., the neutrino cooling.

We show the values of σ for several R_{NS} and M_{NS} in Fig. 6.2. As expected from the monotonic feature of the NS mass-radius relations (Fig. 2.2), g_{s} shows monotonically varies on the R_{NS}–M_{NS} plane. As we see Eq. (6.1) with a constant pressure condition, a more compact NS shows a higher g_{s} and lower σ. Therefore, a more compact NS has less nuclear fuel (a smaller value of σ). This means the duration of nuclear burning becomes longer for more compact NSs, i.e., a higher luminosity in the tail but a lower luminosity near the peak. We expect, moreover, that a lower σ takes more time than the accumulated matter from a companion to be ignited. The influence of g_{s} on multizone X-ray-burst models has already been discussed based on Eq. (6.1) [133], assuming the constant ignition pressure. In this work, however, we will show that such a previous discussion with only g_{s} and σ is insufficient to explain the multizone X-ray-burst models due to the neutrino cooling effect. That is, we will expect that not only g_{s} but also P_{ign} affect the multi-zone X-ray-burst models.

6.2.3 The effect of neutrino cooling

The temperature structure in steady-state (with compressional heating) should depend on the NS mass or radius because the neutrino emissivity depends on the density. We present the mass dependence of the temperature structure in steady-state in Fig. 6.3. As we see, if the mass is heavier, the temperature in steady-state is much lower because the neutrino cooling is more

Table 6.1: Calculated Values of $Q_{b+\nu}$ [MeV u^{-1}]

M_{NS}	Togashi	LS220	TM1e	TM1
$1.1 M_\odot$	0.70	0.71	0.71	0.73
$1.4 M_\odot$	0.64	0.67	0.68	0.68
$1.7 M_\odot$	0.61	0.62	0.65	0.66
$2.0 M_\odot$	0.54	0.57	0.59	0.62

enhanced owning to the higher central density. By transporting the cooled heat from the core to the outside regions, we see that not only the inside but also the outer regions are cooled, which lowers the temperature around the ignition pressure $P_{\mathrm{ign}} \approx 10^{22-23}$ dyn cm^{-2}.

This implies the possibility that neutrino cooling processes affect the burst light curve. Several studies show this by using Q_b (e.g., Refs. [87, 89]). Although their formulation, which covers only the accreted layer, has no choice but to give a physically groundless Q_b as the boundary condition, our formulation enables us to calculate Q_b without such an artificial parameter. Q_b includes only the crustal heating energy, not the energy lost from neutrino cooling. So, we define the net base heat, including the loss of neutrinos, as $Q_{b+\nu}$, which is expressed as

$$Q_{b+\nu} = \left(1.66 \times 10^{-35} \text{ MeV u}^{-1}\right) \frac{L_{\mathrm{crust}}}{\dot{M}_{-9}} \ , \tag{6.3}$$

where L_{crust} is the luminosity on the NS crust in cgs units. $b + \nu$ means that the base heat includes not only crustal heating but also neutrino cooling unlike Q_b. In Table 6.1, we show the values of $Q_{b+\nu}$.

As seen in Table 6.1, the $Q_{b+\nu}$ value with higher-mass stars is lower due to lower temperature, which is caused by the neutrino cooling effect. Thus, Q_b certainly depends on the mass (and radius). In the case of the crustal heating model by Ref. [155] and the slow neutrino cooling scenario assumed in this work, $Q_{b+\nu}$ is estimated to be around 0.5–0.7 MeV u^{-1}. $Q_{b+\nu}$ also depends on the EOS, but compared with the mass dependency, the change of $Q_{b+\nu}$ or temperature structure due to the EOS is negligible within the slow neutrino cooling scenario.

In Fig. 6.4, we show the correlation of $Q_{\mathrm{b}+\nu}$ and the surface gravitational acceleration $g_{\mathrm{s},14}$. They show anticorrelation for every EOS, where the effects of $Q_{\mathrm{b}+\nu}$, mainly neutrino cooling, becomes significant for higher M_{NS}. The impacts depend on the relative value of $Q_{\mathrm{b}+\nu}$ and $g_{\mathrm{s},14}$. Stiff EOS (e.g., TM1), which has a larger NS radius, shows much large $Q_{\mathrm{b}+\nu}$ compared with $g_{\mathrm{s},14}$, while the softer EOS shows an opposite trend. Although the effect of gravity is dominated, we cannot ignore the effect of neutrino cooling. We discuss this in detail using our X-ray-burst models in the next session.

6.3 Results

First, we calculate the thermal evolution of X-ray bursters from the initial conditions (described in Section 6.2), where energy generation by crustal heating balances the energy loss by neutrino cooling. At the early period of the outburst sequence, the energy generation tends to be higher than the burst events in the later phase due to the residual of the initial compositions in the accreted layer. This mechanism is known as "compositional inertia" [167, 56], which pre-
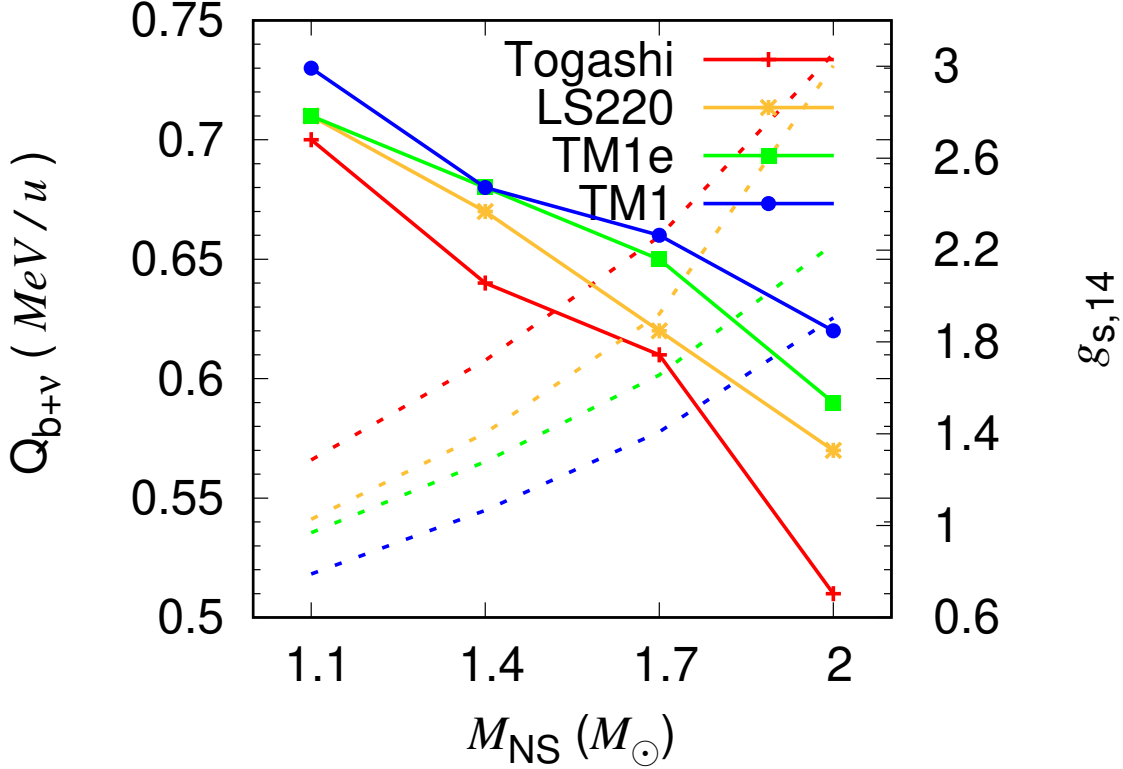
Fig. 6.4: The $Q_{b+\nu}$ (the solid lines for the left axis) and the surface gravitational acceleration $g_{s,14}$ (the dashed lines for the right axis) against M_{NS}.

vents a change in compositions in the accreted layer, converged at the early stage of the burst calculation. Therefore, we discard several decades of the burst with $t \lesssim 2 \times 10^5$ s for all burst calculations. We select at least 15 successive bursts for the following analysis in all subsequent burst events.

6.3.1 The Impacts of M_{NS} and EOS on X-Ray Bursts

In Fig. 6.5, we show the calculated light curves of the X-ray-burst models. The burst events of $M_{NS} = 1.7M_{\odot}$, $\dot{M}_{-9} = 2.5$, and $Z_{CNO} = 0.01$ with four different models are plotted. The time interval of each model is proportional to the NS radius, depending on the EOS. The NS radius becomes smaller in the following order: Togashi, LS220, TM1e, and TM1 (Fig. 2.2), due to the softness of EOSs. The bursts with Togashi (soft EOS) show the smallest interval, while TM1 (stiff EOS) has the longest time interval. As the interval becomes larger, the peak luminosity also appears larger.

In Fig. 6.6, we compare the profiles of a typical burst light curve for different EOS burst models, with $N_{NS} = 1.7$ and $M_{CNO} = 0.01$. Fig. 6.6a shows cases of $\dot{M}_{-9} = 2.5$. We find that the peak luminosity becomes higher for the larger NS radii, which is different from the relationship between the period and NS mass. In particular, burst models with the TM1 EOS ($M_{NS} = 2.0M_{\odot}$) have a significantly high peak luminosity. For the cases with a lower mass accretion ($\dot{M}_{-9} = 2.0$) in Fig. 6.6b, the change in the peak luminosity appears to follow the
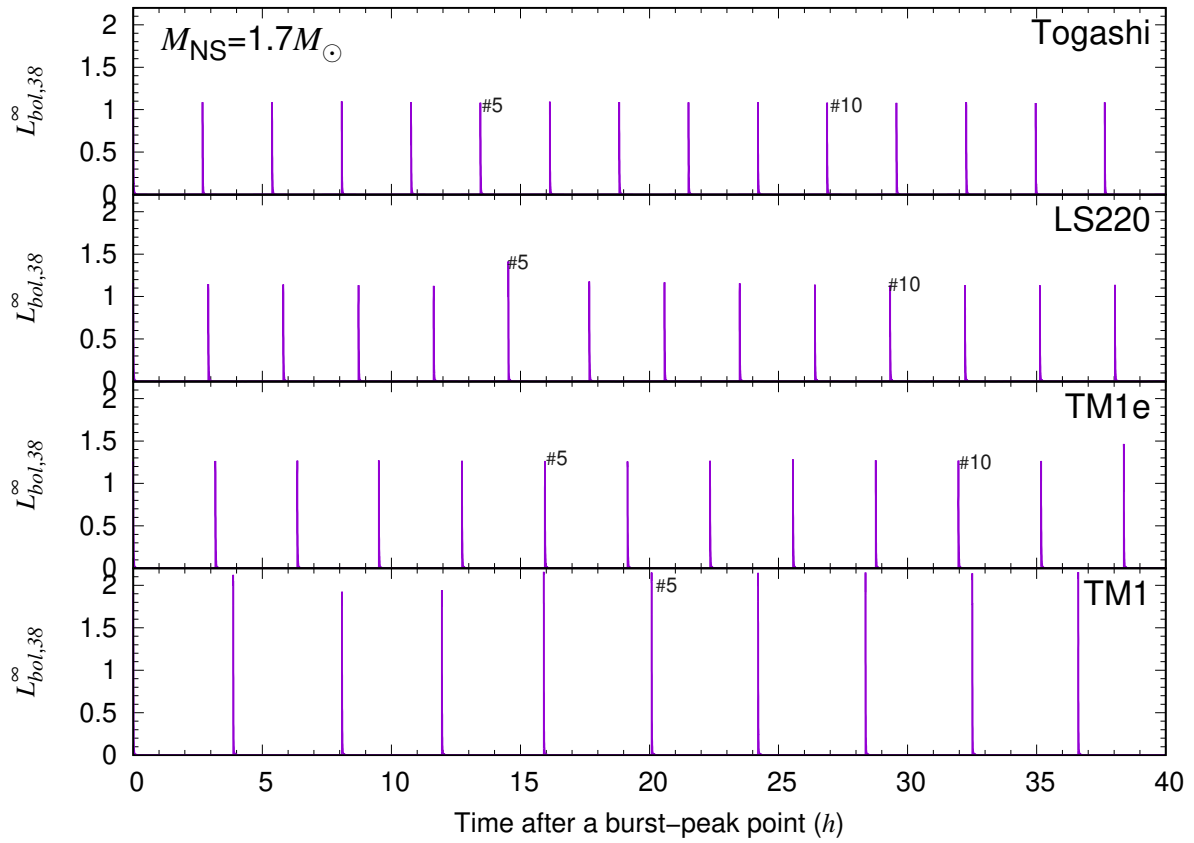
Fig. 6.5: The luminosity of the burst sequence from 0–40 hr for several NS EOSs. We adopt $M_{\rm NS} = 1.7 M_\odot$, $\dot{M}_{-9} = 2.5$, and $Z_{\rm CNO} = 0.01$.
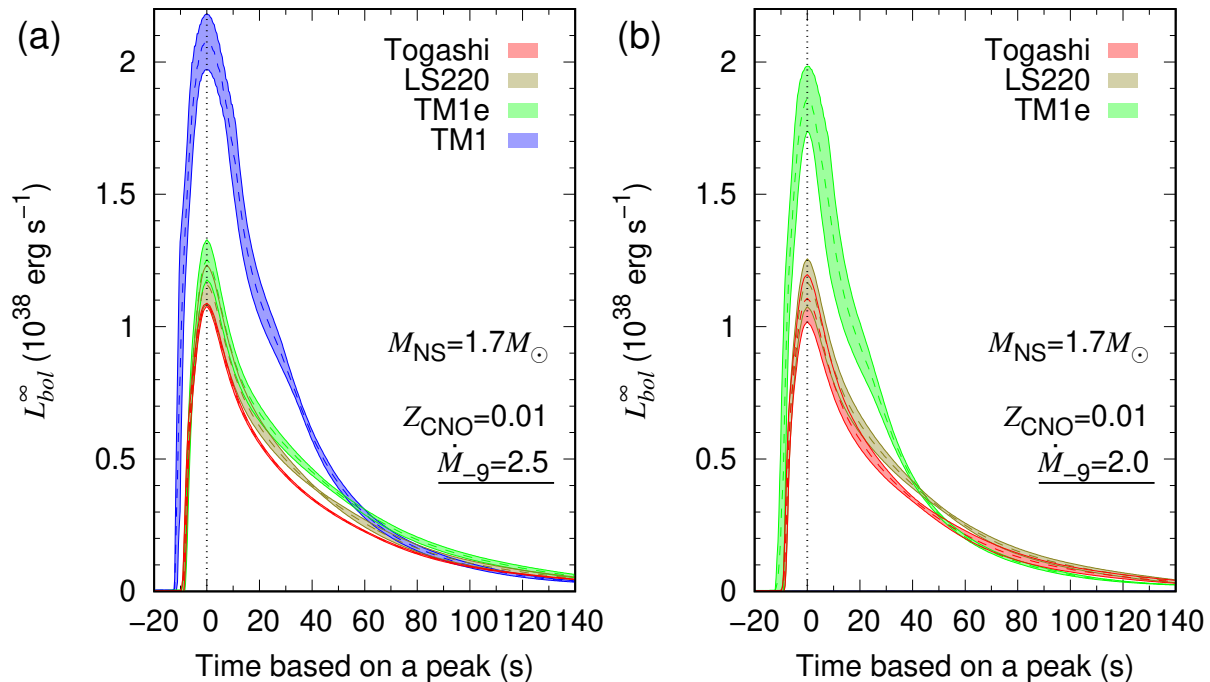
Fig. 6.6: The light curves of the burst phase with $M_{NS} = 1.7 M_\odot$ for several EOSs. Assuming $Z_{CNO} = 0.01$, we adopt (a) $\dot{M}_{-9} = 2.0$ and (b) $\dot{M}_{-9} = 2.5$. We omitted the case of TM1 with $\dot{M}_{-9} = 2.0$, which reaches the PRE.

same trend. The peak luminosity reaches at 2×10^{38} erg s^{-1}, near the Eddington luminosity, so that the TM1 case occurs in the photospheric radius expansion (PRE). On the other hand, the tail structure of the light curves, mainly determined by nuclear burning in the rp process, appears to be independent of the EOS with $\dot{M}_{-9} = 2.0$ and 2.5. Other timescales (i.e., the rising phase, transient to burst phase, and decay time) are also independent of the EOS.

We make a similar comparison in Fig. 6.7 and 6.8 focusing on the difference in M_{NS}. The profiles of the burst sequences for the $M_{CNO} = 0.01$ and $\dot{M}_{-9} = 2.5$ models are shown in Fig. 6.7. We find that the intervals change due to the mass of the NS. As M_{NS} increases, the time interval becomes larger (Fig. 6.7). The peak luminosity becomes higher (Fig. 6.8a), though their changes are smaller than the variation caused by the EOS (Fig. 6.8a). We should note that the M_{NS} and EOS are not determined independently, as shown in Fig. 2.2. However, a soft EOS has a compact NS (a smaller radius for the same M_{NS}), while a stiff EOS shows a less compact one (a larger radius for the same M_{NS}). Based on the compactness of NSs, the trends in mass dependence and EOS dependence are opposite. The time interval is higher with the larger-radius EOS (or the higher mass at the same radius) in Fig. 6.5 and 6.7, while it is lower with a higher mass. For the peak luminosity, a similar difference is seen.

To resolve the discrepancy between the mass and EOS dependence, the effect of neutrino emission via the NS mass may be a key issue. As we discussed in Section 6.2.3 and implied from the initial temperature structure (Fig. 6.3), neutrino emission inside the NS, which lowers
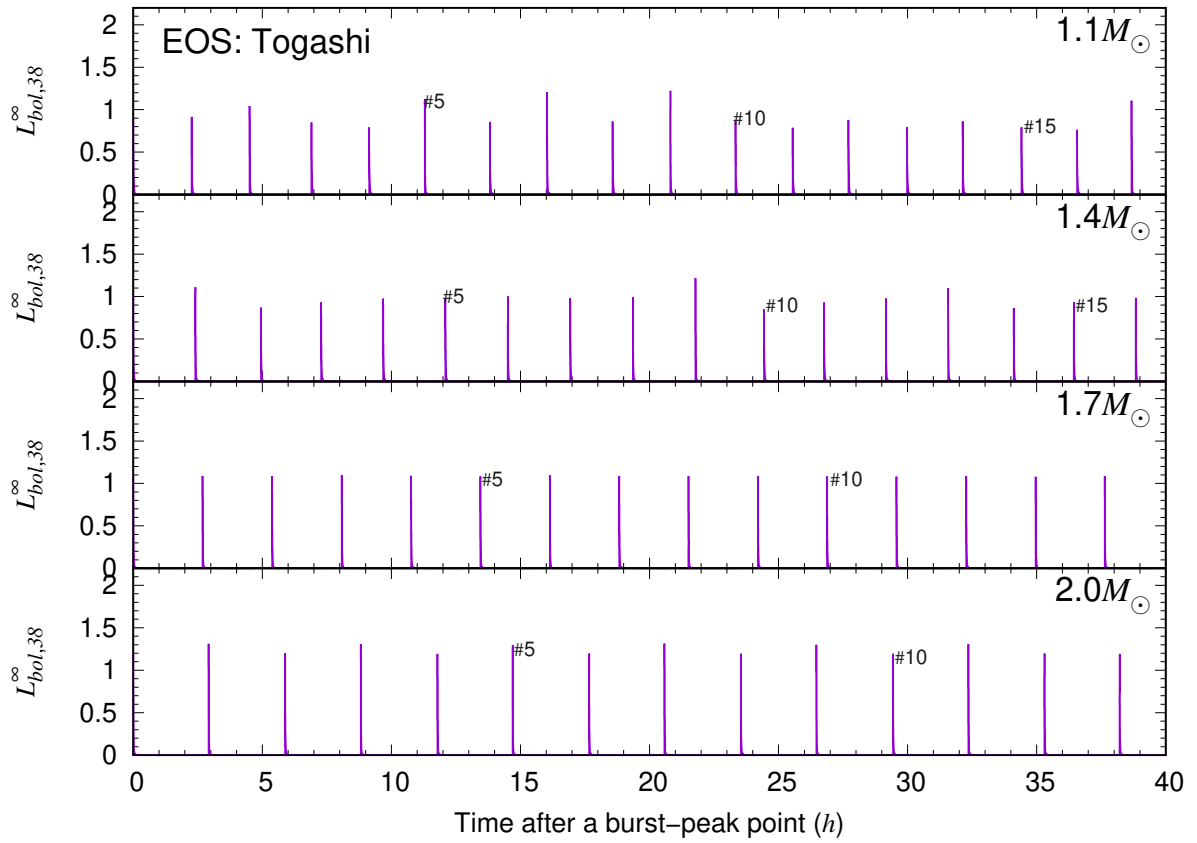
Fig. 6.7: The luminosity of the burst sequence from 0–40 hr for several $M_{\rm NS}$. Based on the Togashi EOS, we adopt $M_{\rm NS} = 1.7 M_\odot$, $\dot{M}_{-9} = 2.5$, and $Z_{\rm CNO} = 0.01$.
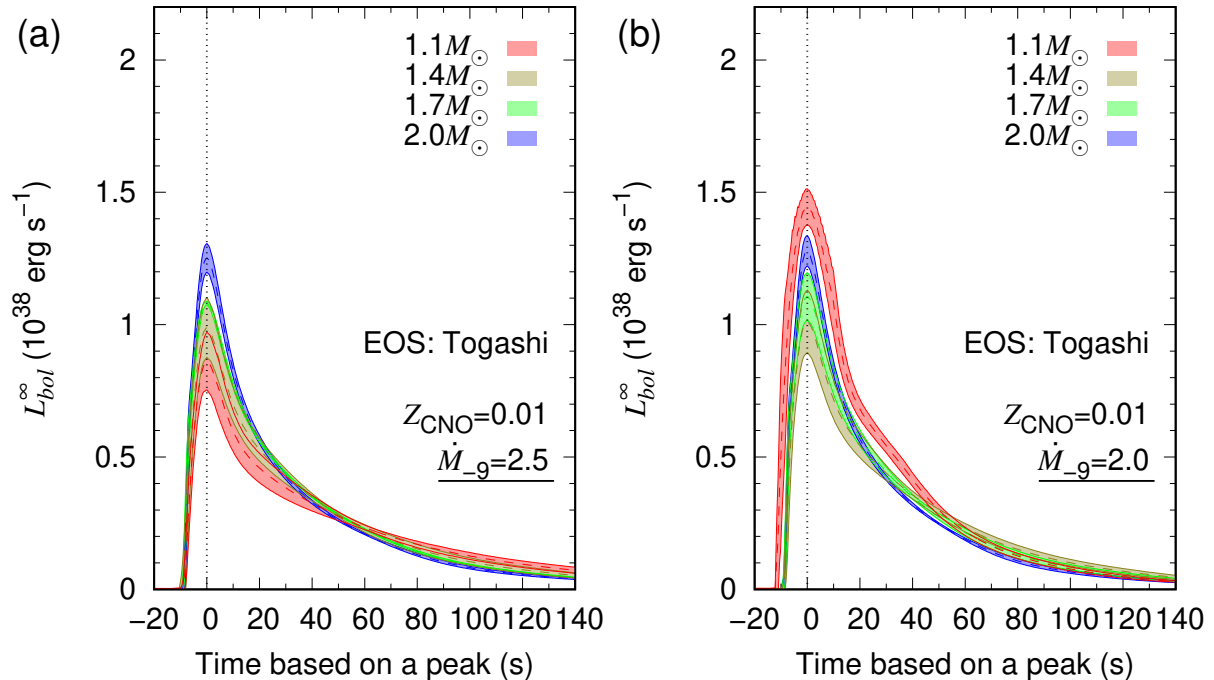
Fig. 6.8: The light curves of the burst phase with the Togashi EOS for several M_{NS}. Assuming $Z_{\mathrm{CNO}} = 0.01$, we adopt (a) $\dot{M}_{-9} = 2.0$ and (b) $\dot{M}_{-9} = 2.5$.

the temperature itself, is involved with light curves in the latter case of mass dependence. Under the current assumption of the same neutrino processes in any EOS, we recognize that the difference in light curves between both tendencies is caused by the neutrino emission inside the NS. The effect of neutrino cooling may change the dependence of the burst parameters on the mass and EOS (Fig. 6.3). This is seen in Fig. 6.8, where the mass dependence of light curves is nonmonotonic and complicated when we change $\dot{M}_{-9}$. While the peak luminosity becomes higher with higher mass for $\dot{M}_{-9} = 2.5$, conversely, the peak luminosity is lower for $\dot{M}_{-9} = 2.0$. The inversion of the trend is not seen in 6.6, which compares the EOS dependence between $\dot{M}_{-9} = 2.0$ and $\dot{M}_{-9} = 2.5$. It can be caused by neutrino cooling on the light curves, the impact of which can be larger than others.

The light curves of X-ray bursts are characterized by few parameters such as the recurrence time Δt, the peak luminosity L_{peak}, and the burst strength of nuclear burning α [83]. The α is defined by the ratio of the accretion energy to the burst energy, i.e.,

$$\alpha = \frac{z_g}{1 + z_g} \dot{M} c^2 \frac{\Delta t}{E_b}, \qquad (6.4)$$

where z_g is the gravitational redshift and E_b is the total burst energy. To calculate E_b, we set the minimum value for the luminosity in the numerical integration. We calculate E_b for $L > 0.25 L_{\mathrm{acc}}$, where L_{acc} is the accretion luminosity. In our calculations, L_{acc} is small enough to calculate E_b without the loss of generality. This is because the peak luminosities in the present
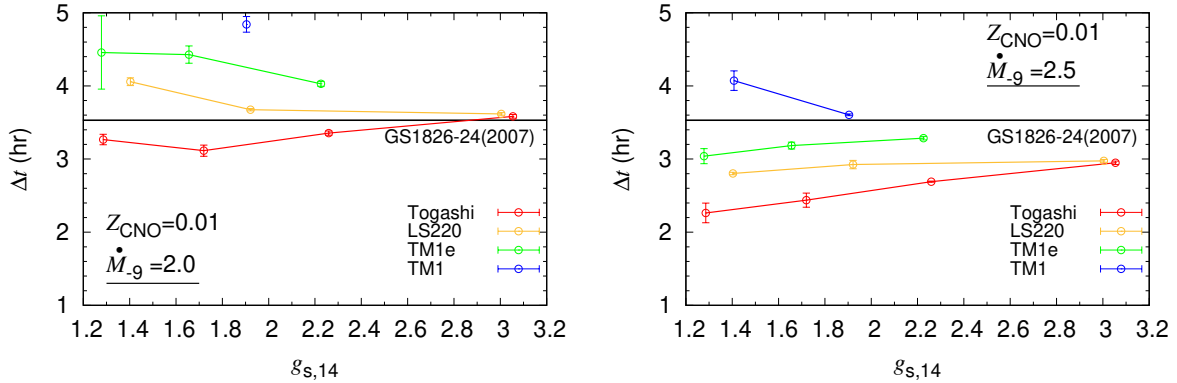
70

Fig. 6.9: The Δt plotted by $g_{s,14}$ with different EOSs, i.e., Togashi (red), LS220 (orange), TM1e (green), and TM1 (blue). We adopt $Z_{CNS} = 0.01$ with $\dot{M} = 2.0$ (left) and $\dot{M} = 2.5$ (right). The horizontal solid line corresponds to the observed value of GS 1826-24 [83]. Models with $L > L_{edd}$ are omitted, where the hydrostatic equilibrium is invalid.
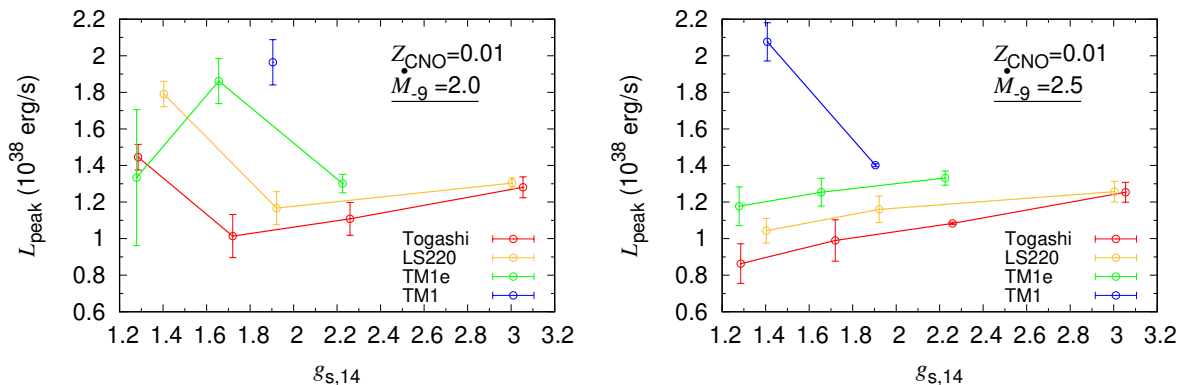

Fig. 6.10: Same as Fig. 6.9, but for the peak luminosity L_{peak}

study are $\sim 10^{38}$erg s^{-1}, which is much higher than $L_{acc} \sim 10^{35}$erg s^{-1}. The dependence of the integration range on E_b may change with high $\dot{M}$ near the Eddington accretion rate $\sim 10^{-8} M_\odot$yr (Ref. [168] for millihertz QPO from H/He mixed nuclear burning).

Figs. 6.9, 6.10, 6.11 and 6.12 show Δt, α, L_{peak}, and E_{burst}, respectively, for several M_{NS}'s. As the NS mass is uniquely determined by the EOS with fixed burst parameters, we find a relationship between M_{NS} and the EOS. With few exceptions that depend on the EOS, the burst parameters (i.e., Δt, L_{peak}, α, and E_{burst}) show a monotonic correlation with the NS mass. For the dependence on the NS mass, the behavior of Δt and L_{peak} is hard to see because at least two different physical processes are involved with their change. However, α becomes larger with a higher mass. This relationship of α is consistent with an EOS dependence in that the value is higher with more compact NSs.

In Fig. 6.9, we compare the calculated Δt with the value of the X-ray binary of GS 1826-24 [83]. The burst models of $M_{NS} = 2.0 M_\odot$, $Z_{CNO} = 0.01$, and $\dot{M}_{-9} = 2.0$ with the Togashi and LS220 EOSs are consistent with observed values. Observational burst parameters (i.e., Δt, L_{peak}, and α) may be useful to constrain the EOS. Considering the uncertainty due to M_{NS}, α provides the strictest restriction on the information of interior NS in many parameters related to the X-
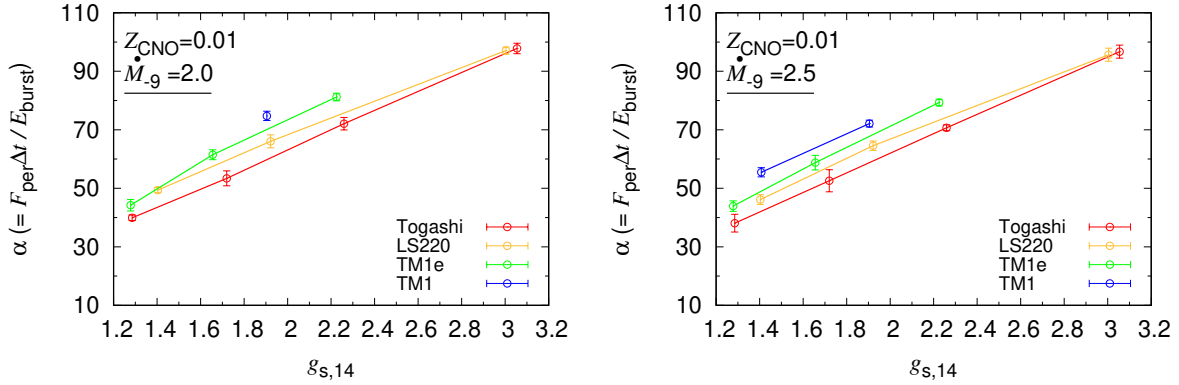
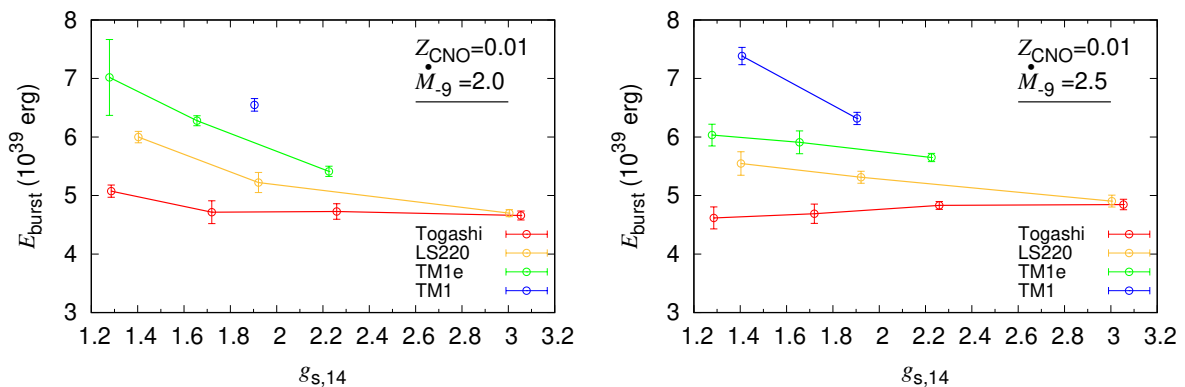Fig. 6.11: Same as Fig. 6.9, but for the burst strength α

Fig. 6.12: Same as Fig. 6.9, but for the total burst energy E_{burst}

ray burst, though the properties of burst light curves are still sensitive to other parameters, especially to $\dot{M}_{-9}$ and Z_{CNO} [169].

6.3.2 The Effects of g_s and $Q_{b+\nu}$ on the X-Ray-burst Models

We discuss physical reasons for the mass dependence of burst light curves. Assuming that the NS mass tends to have an anticorrelation with the NS radius in especially high-mass regions, though there are several exceptions, E_b should be higher in high-mass models owning to the strong surface gravity. However, the mass dependence (shown in Fig. 6.12) does not match this tendency and therefore is affected by another effect. It is presumed to be the effect of neutrino emission to decrease the temperature, as shown in the initial burst models in Fig. 6.3. This effect is characterized by the effective base heat $Q_{b+\nu}$ as seen in Fig. 6.4.

The $Q_{b+\nu}$ effect can be seen in the mass dependence of the temperature structure and hydrogen mass fraction in Fig. 6.19. These figures show that the ignition pressure is higher with high-mass models. This cannot be explained by the g_s effect but by the $Q_{b+\nu}$ effect, which plays a role to lower the overall temperature in higher-mass regions (Table 6.1). The pressure at peak temperature can judge whether g_s or $Q_{b+\nu}$ effect is stronger, depending on the burst model.

For the mass dependence of the burst models, the effect of g_s and $Q_{b+\nu}$ can be seen simultaneously. In Fig. 6.14, the $\dot{M}_{-9} = 2.5$ and $Z_{CNO} = 0.01$ case, both EOS models (Togashi
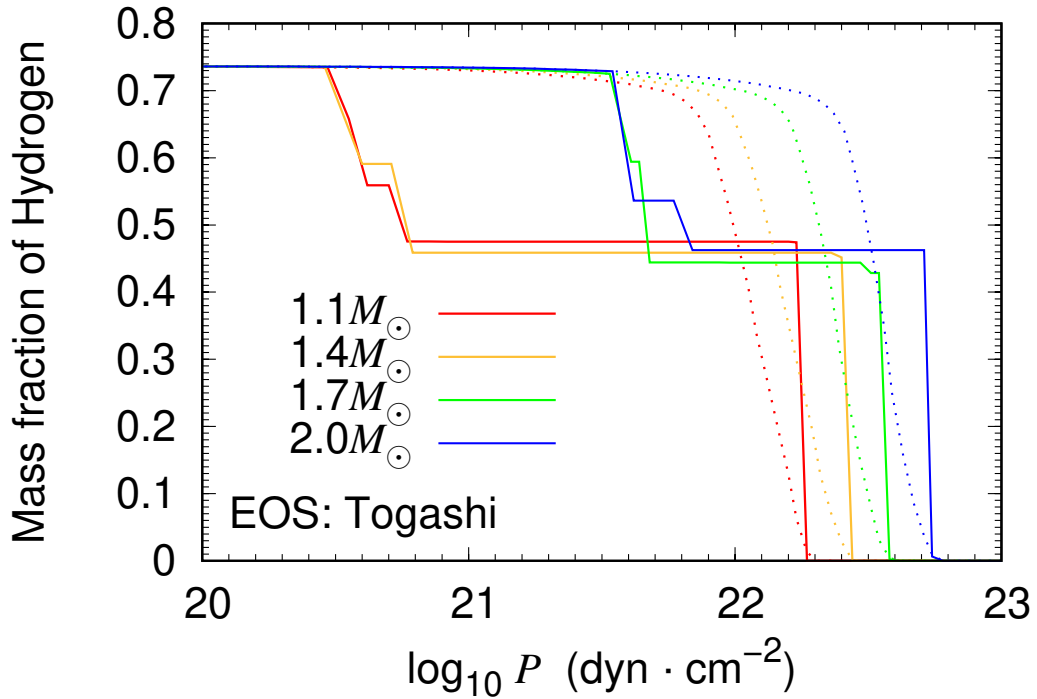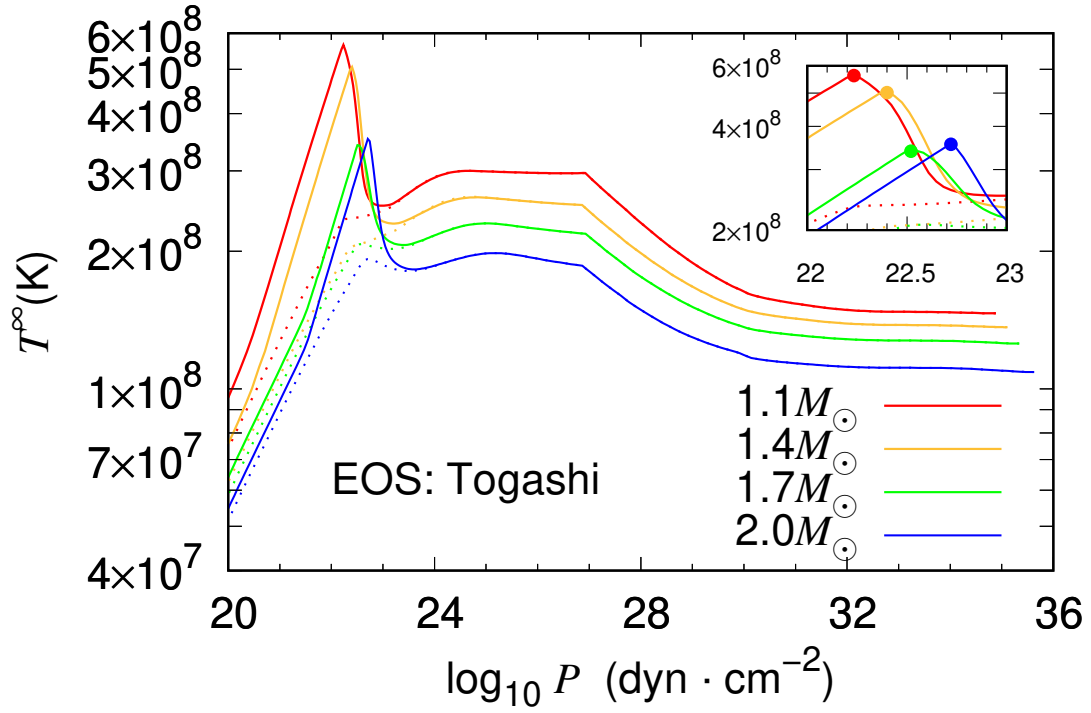
Fig. 6.13: The structures of the redshifted temperature (upper) and the mass fraction of hydrogen (lower) plotted against the ignition pressure with 1.7 $M_\odot$ stars. We adopted 1.7 $M_\odot$, $\dot{M}_{-9} = 2.5$, and $Z_{\mathrm{CNO}} = 0.01$. For each model, the dotted line and the solid line that show the structures before and after ignition (at $t \simeq 10^6$ s), respectively.
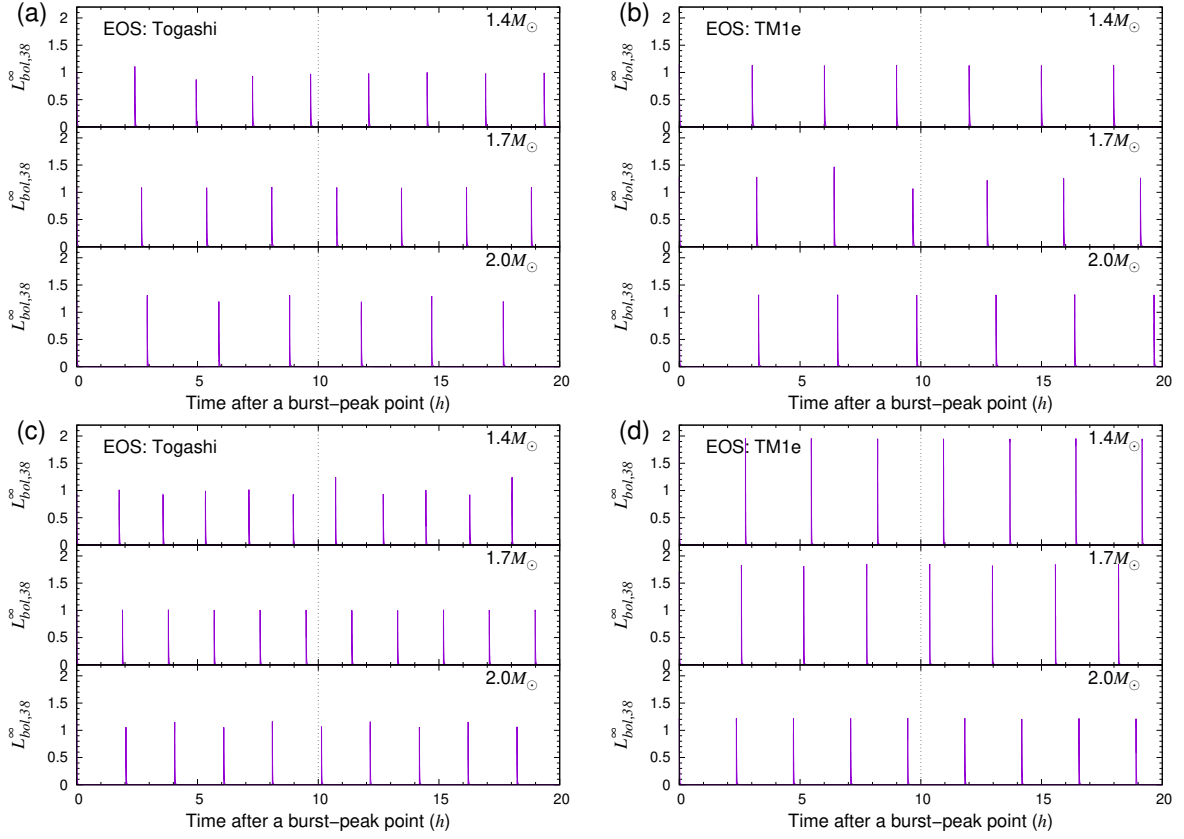
Fig. 6.14: The bolometric luminosity of the sequences of X-ray bursts over 20 hr. The results for $N_{\rm NS} = 1.4$, 1.7, and $2.0M_\odot$ are shown in the each panel: (a) $(\dot{M}_{-9}, Z_{\rm CNO}) = (2.5, 0.01)$ with Togashi, (b) $(\dot{M}_{-9}, Z_{\rm CNO}) = (2.5, 0.01)$ with TM1e, (c) $(\dot{M}_{-9}, Z_{\rm CNO}) = (3.0, 0.02)$ with Togashi, and (d) $(\dot{M}_{-9}, Z_{\rm CNO}) = (3.0, 0.02)$ with TM1e. The time at 10 hr is highlighted by the vertical dotted line.

and TM1e) have fewer burst events or higher Δt with higher-mass regions. For these burst models, therefore, the $Q_{b+\nu}$ effect is larger than the g_s effect. In Fig. 6.14, the $\dot{M}_{-9} = 3.0$ and $Z_{\mathrm{CNO}} = 0.02$ case; however, the number of burst sequences with the Togashi EOS is decreased with higher-mass regions, and Δt is higher, which is opposite to the case in the TM1e EOS. This implies that in the $\dot{M}_{-9} = 3.0$ and $Z_{\mathrm{CNO}} = 0.02$ case, the $Q_{b+\nu}$ effect is larger than the g_s effect with the Togashi EOS while it is lower with the TM1e EOS. Thus, by changing $\dot{M}_{-9}$ and Z_{CNO}, mass dependence of Δt could be changed qualitatively.

For the overall mass dependence of Δt, let us look at Fig. 6.9. With the Togashi EOS, for example, Δt has a positive correlation with mass, which means that the $Q_{b+\nu}$ effect is stronger than the g_s effect. For other EOSs, however, that tendency does not always remain, such as with the TM1e EOS case with $\dot{M}_{-9} = 3.0$ and $Z_{\mathrm{CNO}} = 0.02$. Assuming that the quantitatively same $Q_{b+\nu}$ effect works with any EOS-like setting in this work, the g_s effect appears more easily with the softer or higher-symmetry-energy EOS in high-density regions, such as the TM1 and TM1e EOSs. This is because the g_s effect is higher with a larger-radius EOS, as shown in Fig. 6.2.

In summary, the effect of the surface gravity is lower in higher-mass models, which makes Δt longer because more fuel needs to be ignited. Meanwhile, the $Q_{b+\nu}$ effect is higher, leading to shorter Δt. This is the reason why the effects of g_s and $Q_{b+\nu}$ (Fig. 6.4) show opposite dependence on Δt. This might be useful in specifying not only the NS structure but also the heating or cooling processes inside NSs via the $Q_{b+\nu}$ effect in the future, though elucidating this is hard in that burst light curves are sensitive to other input parameters such as $\dot{M}_{-9}$ and Z_{CNO}.

For L_{peak}, the tendency of the EOS and mass is similar to that of Δt. Because L_{peak} is highly related to how much hydrogen is burnt, a large amount of hydrogen is not burnt, as seen in Fig. 6.19. This dramatically affects the efficiency of the first nuclear burning in X-ray bursts, the triple-α reaction. Because the parameter dependence of the amount of fuel is unclear within the multizone framework, the reliance on the EOS and mass of L_{peak} is more unclear than that of Δt.

Despite the complicated mass dependence of Δt, α has a positive correlation with mass and an anticorrelation with the radius. Because Δt and E_{burst} are higher with a larger-radius EOS, it is hard to reveal the reason, but due to the $Q_{b+\nu}$ effect, the neutrino flux increases in higher-mass regions, and this makes the persistent flux F_{per} higher. This is because, in the persistent term, the crustal heating and neutrino cooling processes dominate the thermal evolution of accreting NSs. Their strength is not that different from nuclear burning. Moreover, as F_{per} depends on $z_g/(1+z_g)$, where z_g is the gravitational redshift, as shown in Eq. (6.4), the gravitational effect seems to be important for the mass dependence of α. These are two reasons for the positive correlation between α and mass.

6.3.3 Application to the Clocked Burster GS 1826–24

To examine the validity of the burst models, we compare the theoretical burst light curves and observations. For such an observation, we take the observed light curve of a clocked burster event with GS 1826–24 in 2007, whose burst number was ten times. We show the EOS (Togashi, TM1e) and mass ($M_{\mathrm{NS}} = 1.4, 2.0\ M_{\odot}$) dependence on the burst light curve in Fig. 6.15 with $\dot{M}_{-9} = 2.5$ and $Z_{\mathrm{CNO}} = 0.01$. If we change the EOS from Togashi to TM1e, the peak luminosity
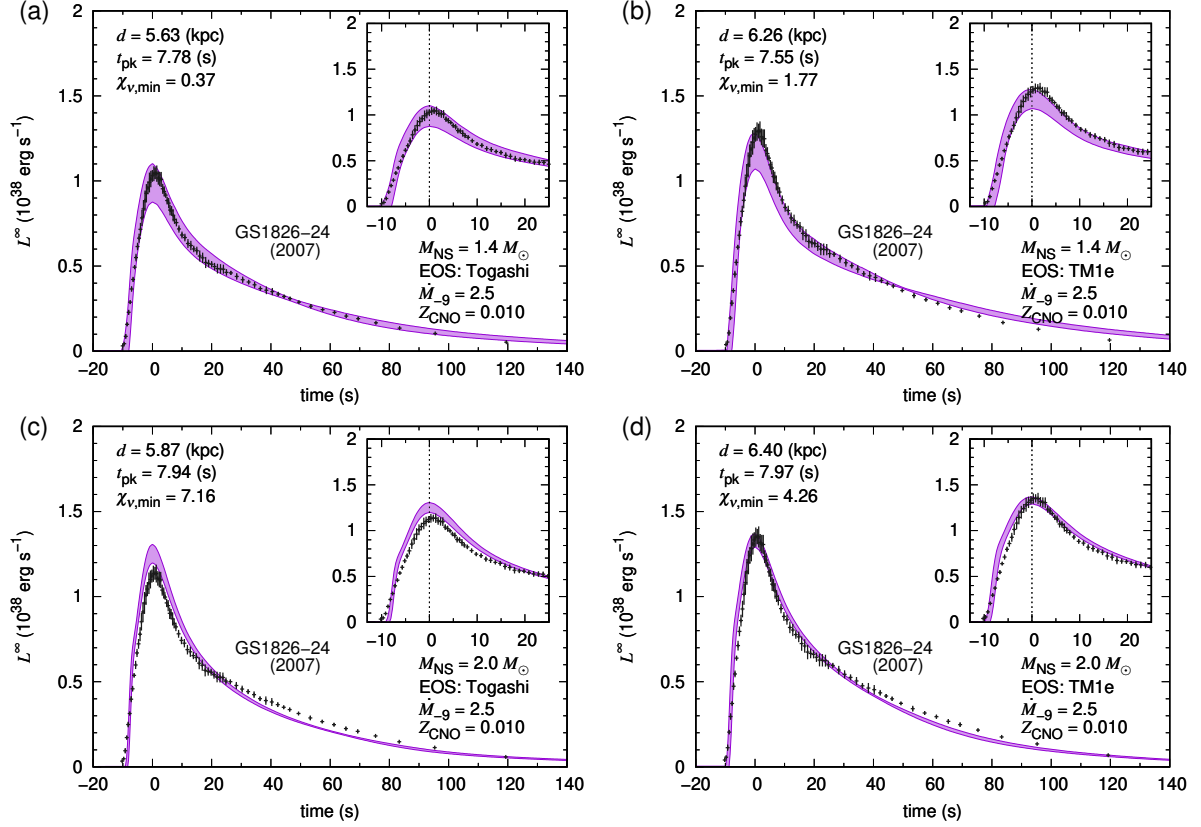
Fig. 6.15: Comparison of the calculated averaged burst light curves with observed ones of GS 1826-24 in 2007, assuming $\dot{M}_{-9} = 2.5, Z_{CNO} = 0.01$: (a) Togashi with $M_{NS} = 1.4\ M_{\odot}$, (b) Togashi with 2.0 $M_{\odot}$, (c) TM1e with $M_{NS} = 1.4\ M_{\odot}$, and (d) TM1e with $M_{NS} = 2.0\ M_{\odot}$. We set $t = 0$ s at the peak time of the light curves and plot within the 1σ regions of many burst light curves. The distance including burst anisotropy d, the time after the peak t_{pk}, and the minimum χ^2 value $\chi_{\nu,min}$ are shown in each panel.
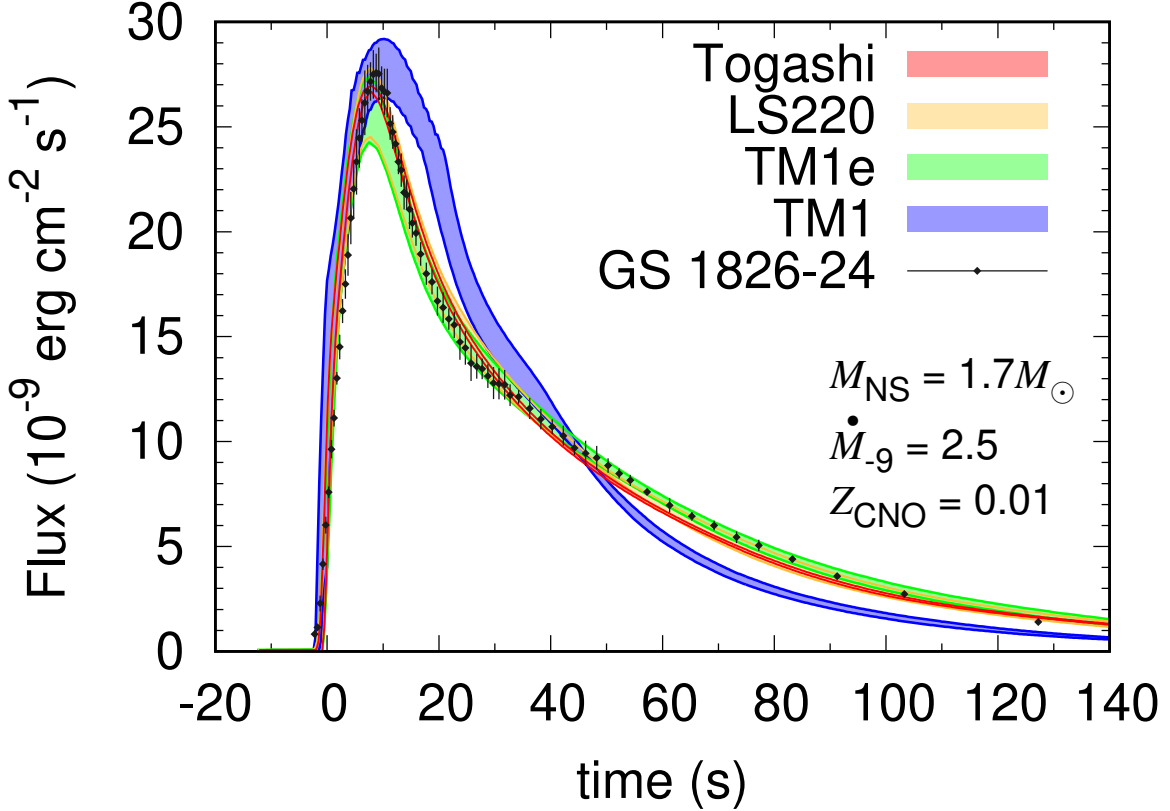
Fig. 6.16: Comparison between theoretical and observational X-ray flux of GS 1826$-$24 with $M_{NS} = 1.7\ M_\odot$, $\dot{M}_{-9} = 2.5$ and $Z_{CNO} = 0.01$, focusing on the constraint on EOSs.

becomes higher due to the g_s effect. If the mass is changed from $M_{NS} = 1.4\ M_\odot$ to $2.0\ M_\odot$, however, the qualitative change is different for the EOS; the peak luminosity is lower for the Togashi EOS while higher for the TM1e EOS. This is explained by the g_s and $Q_{b+\nu}$ effects. In Fig. 6.15, the Togashi EOS with $M_{NS} = 1.4\ M_\odot$ seems to be favored, which is plausible compared with other models. In our burst models, the larger-radius EOS has a higher luminosity or causes PRE, such as the TM1 EOS. However, it is known that all bursts of GS 1826–24 in 2007 did not show PRE [83]. Finally, for a large-radius EOS such as TM1, the peak luminosity is too high to explain the observations due to a larger g_s effect. We show the comparison between theoretical and observational X-ray flux in Fig. 6.16, which shows that the TM1 EOS with $1.7\ M_\odot$ NSs is clearly inconsistent with the shape of observed light curves, provided that we fix $\dot{M}_{-9} = 2.5$ and $Z_{CNO} = 0.01$. Thus, observations of clocked bursters can possibly constrain the NS EOS. Things similar to the EOS dependence can apply to the mass dependence. In Fig. 6.15, high-mass models seem to be inconsistent with the observations because the peak luminosity is lower than the observed light curves due to the larger $Q_{b+\nu}$ effect. Thus, the mass of clocked bursters might be constrained by the observations. Although burst models are very sensitive to the accretion rate and composition of the companion star, the g_s and $Q_{b+\nu}$ effects cannot be ignored for consistent burst modeling of bursters.

In this work, we could not find consistent models with both Δt and the shape of the burst light curve of GS 1826–24 in 2007 simultaneously. For example, we show the well-fitted burst model: Togashi EOS, $M_{NS} = 1.4\ M_\odot$, $\dot{M}_{-9} = 2.5$ and $Z_{CNO} = 0.01$. This burst model shows
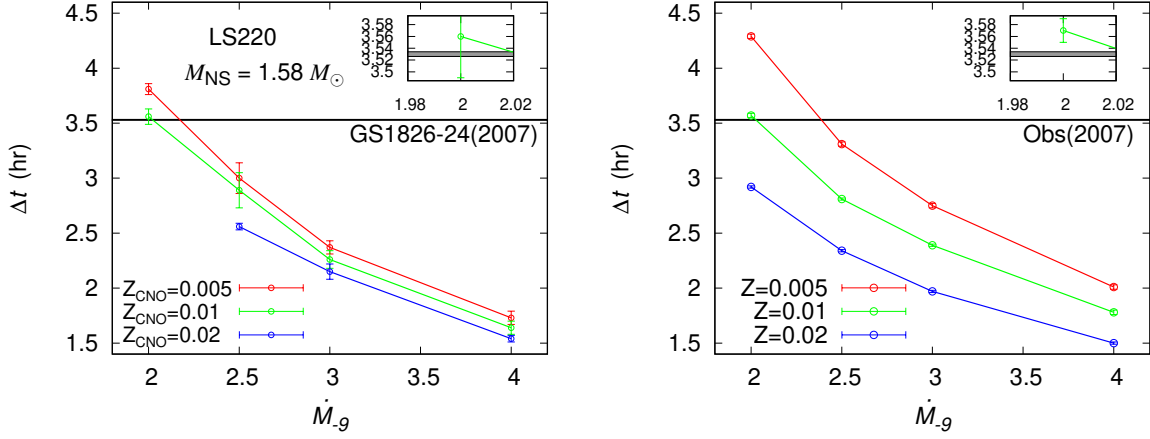
Fig. 6.17: Recurrence time Δt v.s. accretion rate $\dot{M}_{-9}$. The error bars are 1σ regions of Δt. From the latest observational value of GS 1826–24 in 2007, we adopt $\Delta t = 3.530 \pm 0.004$ hr as indicated by s black line. The insets in these upper-right corners indicate magnification of the region around $\Delta t = 3.53$ hr and $\dot{M}_{-9} = 2.0$. Left panel corresponds to $M = 1.58\ M_\odot$ while right $M = 2.00\ M_\odot$.
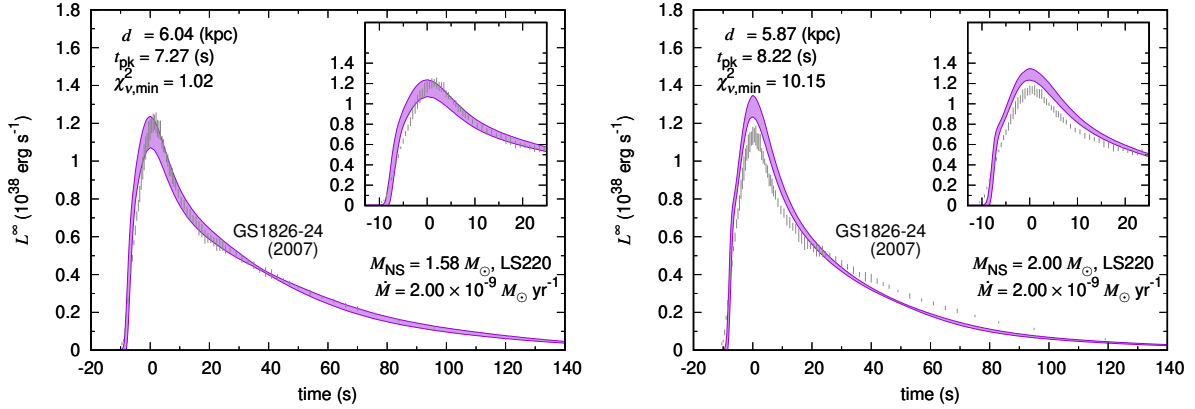

Fig. 6.18: Same as Fig. 6.15, but the *best fit* model of $M = 1.58\ M_\odot$ (left) and a model of $M = 2.0\ M_\odot$ whose overall shape is inconsistent with observations. We fix $\dot{M}_{-9} = 2.0$ and $Z_{\mathrm{CNO}} = 0.01$.
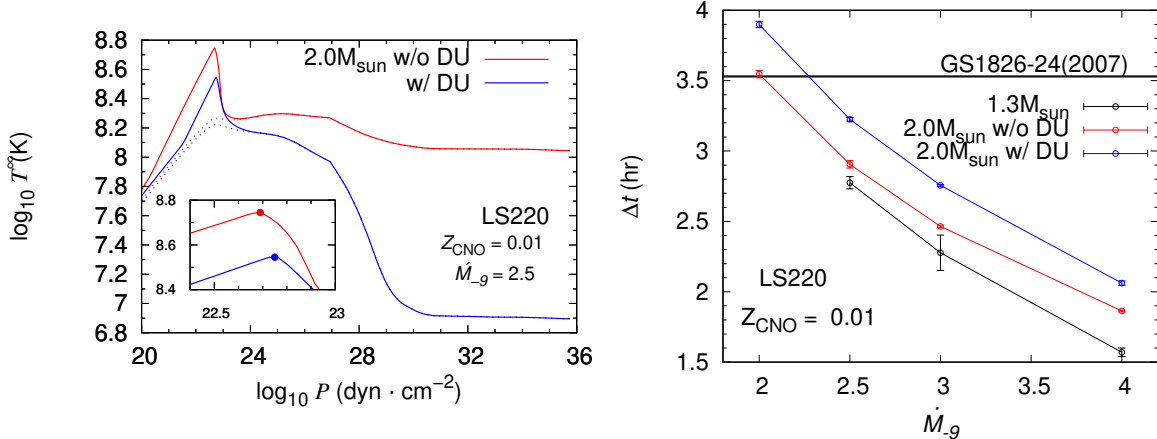
Fig. 6.19: Left: Same as the upper panel of Fig. , but without (blue) and with (red) the DU process. Right: Same as Fig. 6.17, but without (blue) and with (red) the DU process. We also plot the Δt–$\dot{M}_{-9}$ relation with $M_{NS} = 1.3\ M_\odot$ where the DU process does not work. For both figures, we fix the LS220 EOS.

a shorter recurrence time $\Delta t = 2.44 \pm 0.10$ h compared with the observed one of ~ 3.53 h. Thus, it is not easy to find consistent burst models with GS 1826–24 in 2007, but such a burst model can be created by changing the mass and EOS. Focusing on $M_{NS} = 1.58\ M_\odot$ and $2.0\ M_\odot$ with the LS220 EOS, we examine the model consistency with GS 1826–24 in 2007 in detail. We show the best-fit and not good models of the recurrence time and the shape of the burst light curve in Figs. 6.17 and 6.18, respectively. We can recognize that the burst model for the LS220 EOS and $M_{NS} = 1.58 M_\odot$, $\dot{M}_{-9} = 2.0$, and $Z_{CNO} = 0.01$ is consistent with both Δt and light-curve observations of GS 1826–24 in 2007 . Then, the effective base heat is calculated to be $Q_{b+\nu} = 0.67$ MeV u^{-1} ($Q_b = 0.35$ MeV u^{-1}), which is consistent with the recent studies of burst modeling of $Q_b < 0.5$ MeV u^{-1} [87, 89].

If the radius is large, such as in the TM1 EOS, the peak luminosity tends to be too high to explain the shape of burst light curves of GS 1826–24 due to the g_s^{-1} effect. PRE occurs in several models, which are inconsistent with GS 1826–24 in 2007. Hence, a large-radius EOS does not seem to be preferred from the observations of GS 1826–24, which is consistent with other observational constraints. Although the EOS and mass dependences of burst light curves are complicated due to the competition between the g_s and $Q_{b+\nu}$ effects, as shown above, if more information on the companion is available in the future, observational bursters can play a significant role in constraining the NS EOS and mass.

6.3.4   The Impact of Direct Urca Process on X-ray Bursts

As we see above, the neutrino cooling inside NS cores affects the burst behaviors by increasing the ignition pressure. However, we assume the slow cooling scenario, that is, the DU (DU) process is artificially turned off, though the large symmetry energy EOSs such as the LS220 and TM1 easily cause such a fast cooling process as shown in Figs. 4.1 and 4.2. Intuitively, if the DU process occurs and cools accreting NSs, it should take more time for unstable mixed H/He nuclear burning, i.e., Δt should be higher. In this subsection, we implement the DU process

for the LS220 with the 2 $M_\odot$ NSs and calculate the X-ray burst light curves in the same way as the above. In this work, we neglect the effects of nucleon superfluidity, which must suppress the DU process. We show the temperature structure just before and after the ignition of light elements in the left panel of Fig. 6.19. We can see that the DU process certainly makes ignition pressure P_{ign} higher by orders of 0.05 or $\sim$10%.

According to the one-zone model, we can express the column density σ in two ways [170]:

$$\sigma = P_{\mathrm{ign}}/g_s \simeq \dot{M}\Delta t/\left(4\pi R_{\mathrm{NS}}^2\right) \ . \tag{6.5}$$

The second $\simeq$ means that the total fuels for ignition can be roughly expressed as the total amounts accumulated due to the accretion during a period, Δt. Eq. (6.5) shows that Δt should be proportional to P_{ign} in the same order, are the NS mass, radius, and accretion rate the same. Thus, Δt should increase by around 10% by the DU process. The right panel in Fig. 6.19 shows the difference of Δt between the slow and fast neutrino cooling models. As expected, we confirm that the DU process enhances Δt by around 10% (+ 0.2–0.4 h). Assuming $\dot{M}_{-9} = 2$, the DU process is likely to occur, but whether to cause the DU process is completely model dependence as a representative of the accretion rate. However, we can present the method to probe the occurrence of the fast cooling process from the observations of Clocked bursters.

We also mention the case of very high Δt such as the superburst, whose burst duration is 1000 times as long as that of the usual Type-I X-ray burst because the superburst is thought to be triggered by carbon ignition necessary for at least high temperature unlike the typical bursts triggered by hydrogen or helium [92]. Then, since the carbon ignition occurs at deeper NS layers than the helium one according to Eq. (6.5), the heating and cooling inside NSs highly affect the temperature at the deep position. From the observed Δt of superbursters such as the 4U 1820–30 [171], we could extract the information on the occurrence of the fast cooling processes compared with the usual X-ray bursts. Such investigation with the numerical modeling of superbursts is left in the future.

6.3.5   Final Products during X-ray Burst Nucleosynthesis

We discuss the EOS dependence of final products during X-ray burst nucleosynthesis. In Fig 6.11, we show that the value of α is larger for more compact NSs. This implies that heavier nuclei should be produced in soft compact EOSs. To check this, we show the EOS dependence of final products in Fig. 6.20. As we see, nuclei heavier than ^{64}Ge are produced with smaller-radius EOSs, while light nuclei are produced with larger-radius EOSs. Hence, this is consistent with the EOS dependence of α. Intuitively, since a larger-radius EOS has higher L_{peak} where the first waiting point nucleus ^{56}Ni is actively synthesized, then the energy necessary for the proceeding of the reaction path does not remain. Finally, the rp process stagnates, and nucleosynthesis is terminated. Conversely, small-radius NSs can keep the energy for the proceed around ^{56}Ni. The EOS dependence of heavier produces than ^{88}Ru is complicated, but qualitatively they tend to be more produced with the smaller-radius EOS.

Fig. 6.21 shows the mass relationship with the final products with the Togashi EOS. We can recognize that heavy nuclei than ^{64}Ge are synthesized in higher-mass NSs. Thus, as we expect
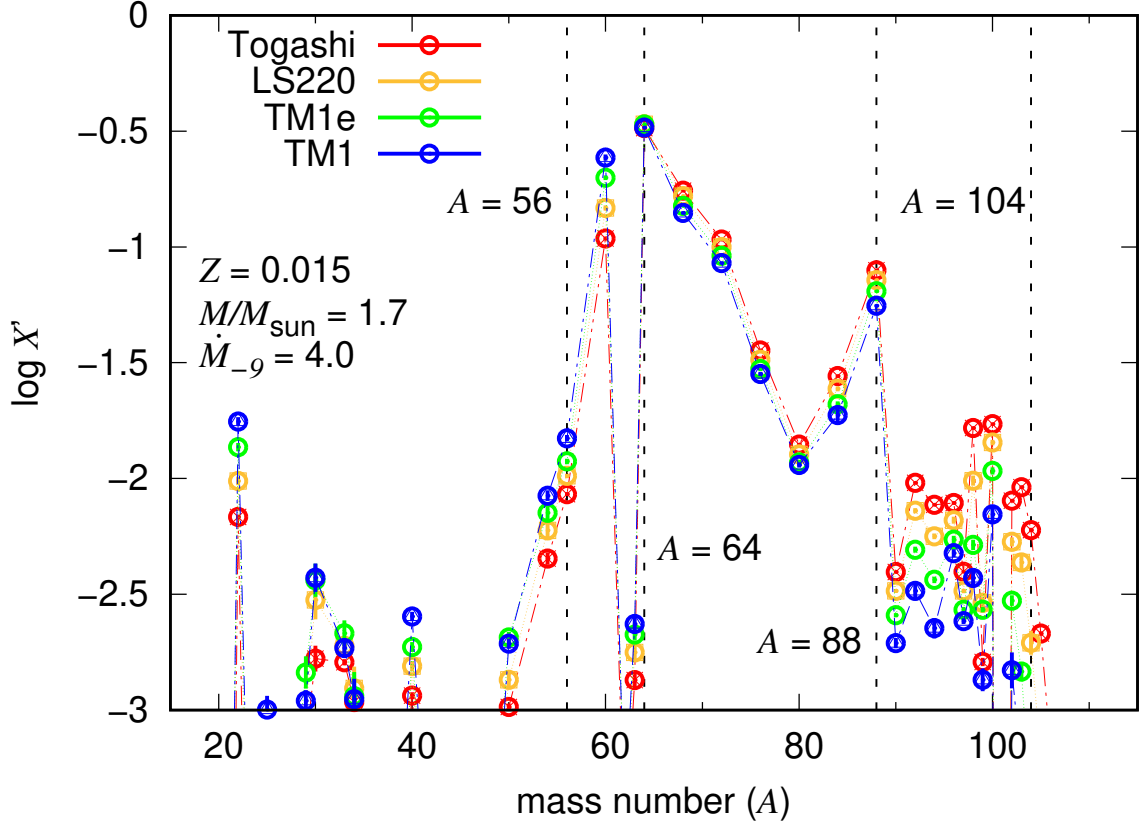
Fig. 6.20: EOS dependence of averaged final products during the nucleosynthesis in X-ray burst with 1.7 $M_\odot$ stars. We fix $\dot{M}_{-9} = 4$ and $Z_{\mathrm{CNO}} = 0.015$. Since light elements of H, He, ^{14}O and ^{15}O initially exists, the only elements with $A \gtrsim 16$ is shown.

from the behavior of the α parameter in Fig 6.11, heavier rp-process elements are synthesized in more compact NSs. We also note that this trend should be universal in mixed hydrogen and helium burning considered in this thesis due to the monotonic relation between α and surface gravity. Thus, if the line emissions from the rp-process element are detected by X-ray observations, we may constrain the EOSs from the observed flux. Actually, Ref. [172] suggests that an enigmatic hump-like structure around 30 keV observed in an accreting NS Aql X-1 comes from the recombination (free-bound) radiation of heavy elements with $Z \sim 50$ in the atmosphere, which is an evidence of rp process. Although how such heavy elements are carried from the synthesized layer to the atmosphere is the crucial problem for the validity of this scenario, such X-ray observations in the hard state will help us to probe the uncertainties of rp process and indirectly other physical ingredients such as the EOS.

6.4   Summary and conclusions

In this study, we investigated theoretical models of X-ray bursts using a 1D general-relativistic evolution code with detailed microphysics. We performed a set of X-ray-bursts models, the light curves of which are compared with observations. We found the microphysics of NSs (i.e., the EOS and cooling and heating) significantly affected the theoretical prediction of the X-ray light curves. The results are summarized as follows.
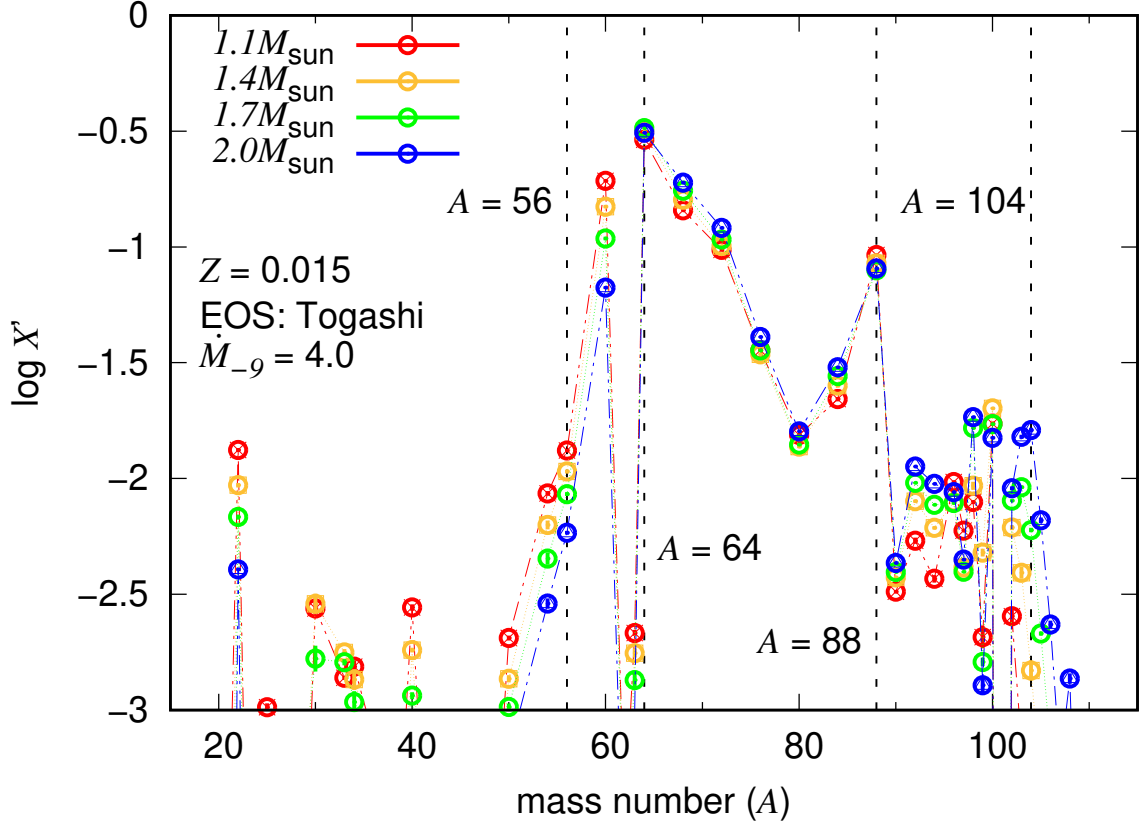
Fig. 6.21: Same as Fig. 6.20, but for the mass relationship for the Togashi EOS.

- The burst parameters characterizing the X-ray-burst light curves depend on the micro-physics of the NS interior (Fig. 6.9–6.12). The recurrence time (Δt) and the peak luminos-ity (L_{peak}) have a positive correlation with the radius of the NS. The α has a monotonic correlation with the surface gravity. However, the uncertainty of the EOS affects the NS mass and radius relation and can significantly impact the burst parameters.

- The NS cooling may vary the burst light curves (i.e., burst parameters) even in the slow cooling scenario. If the mass is higher, Δt and L_{peak} are higher owing to the neutrino cooling. As the temperature in the accreted layer is reduced by NS cooling, the required ignition pressure becomes higher. Furthermore, if the DU process works, the Δt becomes longer by ∼10% due to the increase of the ignition pressure.

- Even considering NS cooling, α shows a strong correlation to the surface gravity (Fig. 6.11). Thus, the α may be the primary parameter to constrain the NS mass and radius among burst parameters. As expected from the monotonic relation between α and surface gravity, final products during X-ray burst nucleosynthesis become heavier in softer NSs.

- We constrained the mass and EOS of the NS GS 1826-24 by comparing observations of X-ray-burst events in 2017. Generally, the models with a stiffer EOS, resulting in a larger NS radius, are ruled out.

We showed that the microphysics of the NS, such as the EOS and neutrino cooling, is important for theoretical X-ray-burst models. On the other hand, many previous works, even

based on multizone X-ray burst models, treat Q_b as an artificial parameter instead of considering the neutrino cooling effect. In this study, the effective base heat $Q_{b+\nu}$ varies with the mass and affects the burst light curves and parameters. Thus, our study implies that the base heat should not be treated as an artificial parameter for more realistic burst models.

As an observational reference, we took the clocked burster events of GS 1826-24 in 2007. We compared our burst models with the observed light curves. As a result, we attempted to constrain the NS EOS and the mass of GS 1826-24. The X-ray binary parameters (e.g., the accretion rate and chemical composition of accreted matter) may change our constraints on the EOS and the NS mass. However, we can develop a deeper understanding if we have more information on the accreted matter and accretion rate.

We assume the slow cooling scenario for the neutrino energy loss, which affects $Q_{b+\nu}$. However, this assumption may be insufficient in modern cooling theory. One of the most important physics to describe the neutrino emissivity is the superfluidity of nucleons. Once the temperature in the NS layers drops below the critical temperature, the nuclear matter transits to a superfluid state, and it proceeds via the following two mechanisms of neutrino emissivity: nucleon superfluidity suppresses conventional neutrino emissions and opens an additional cooling channel, which we call the pair breaking formation process. The efficiency of these effects depends on the superfluid models. Various states of the superfluid phase can appear in a single NS simultaneously (Ref. [35]). Pulsar glitches correspond to the neutron singlet pairing superfluidity, which occurs in the crust of the NS, and the observation of Cassiopeia A may require the triplet pairing of neutrons in the core [173, 174]. Hence, X-ray-burst calculations with neutrino cooling, including the effect of nucleon superfluidity, would be necessary to make more realistic burst models.

Also, the fast neutrino cooling process is required by some observations of cold NSs. The fast cooling process could occur under some specific conditions. Its emissivity is much larger than that of slow cooling processes, and it affects the thermal evolution of the NS, including X-ray bursts. The fast cooling process that likely occurs in NSs is the nucleon DU process, whose cooling effects on burst behavior we examine in this work. Except for the DU process, other fast cooling processes with exotic states of matter could also occur (e.g., [54]). Even within the slow cooling processes, the burst light curves and parameters are affected in this paper. Hence, compared with slow cooling processes, fast cooling processes could significantly change the $Q_{b+\nu}$ value and finally affect the burst light curves and parameters.

Modifying the heating processes as well as the cooling processes inside the NSs is important to describe the burst light curve. One important heating process is crustal heating. Despite some recent work to investigate the heating rate [175, 161, 69, 70], the amount of heat released from the total crustal heating processes has significant uncertainties (typically 1–2 MeV u^{-1}). Moreover, the efficiency in the heat transport from the source to the NS surface of accreted layers depends on the NS model. These uncertainties in the heating process affect burst light curves. Such detail of the heating and cooling effects on the X-ray burst is left for our future work.

Chapter 7

Summary and Outlook

In this thesis, we examined the uncertainties of EOSs on various thermal evolution of NSs. To perform their calculation, we utilized a general relativistic evolutionary code. We also implemented the approximated reaction network with 88 nuclei for mixed H/He burning for the X-ray burst simulation.

First, we employed four EOSs with different symmetry energy and considered the pion condensation for each EOS. Pion condensation tends to make EOSs soft, and we found that if the symmetry energy is lower, the EOS becomes soft in only high-density regions near the central density. This prevents the maximum mass from significantly decreasing, although the radius becomes small for most masses. Hence, low-symmetry-energy EOSs such as the Togashi EOS could reproduce the observations of 2 $M_\odot$ NSs even with pion condensation. Conversely, it is hard for large-symmetry-energy EOSs with the pion condensation to reproduce them. As a consequence of comparison with various observations, we found that the Togashi EOS with pion condensation (Togashi+π) can meet most observational constraints on NS mass and radius.

Second, we discussed the EOS uncertainties on the cooling curves of isolated NSs. If the symmetry energy is very low enough to prohibit the DU process, such as the Togashi EOS, the DU process is prohibited with any masses, and a rapid cooling process through exotic matter should be required for explaining cold observations (Vela, 3C58, RX J0007.0). We focus on this critical problem peculiar to low symmetry energy EOSs. As a result, we found that the Togashi+π can reproduce most of the cooling observations with strong neutron $^3P_2$ superfluidity (TTav). On the other hand, we also found that large-symmetry-energy EOSs do not require any exotic cooling process such as the pion condensation because the DU process occurs for low-mass NSs.

Third, we discussed the EOS uncertainties on the quiescent luminosities of accreting NSs, similar to the case of isolated NS cooling. In particular, 1H 1905+00 and SAX J1808.4–3658 are cold enough to require a strong cooling process. As a result, we found that the Togashi+π EOS can reproduce the most quiescent-luminosity data by considering the strong $^3P_2$ neutron superfluidity. Thus, we showed that the pion condensation is one of the scenarios in low-symmetry-energy EOSs for massive and cold isolated/accreting NS observations. For the observations of hot accreting NSs RX J0812.4–3114, another heating mechanism should be considered regardless of the EOSs.

In this thesis, we considered a pion condensation as an exotic matter to cause the rapid

cooling process. However, the pion condensation scenario is not a unique one to solve the problem of low-symmetry-energy EOSs. Hyperon mixing is also another candidate because hyperon DU processes occur and may cool NSs rapidly. In particular, Λ-hyperon DU processes (e.g., $\Lambda \to p + e + \bar{\nu}_e$) does work because of weak $\Lambda\Lambda$ pairing gap [176, 177] (but see also Ref. [178] for a recent similar experiment). For another example, the kaon condensation could be another good candidate because the kaon-Urca process occurs just like the pion-Urca process and may also cool NSs rapidly. Recently, such exotic-matter EOSs with strangeness have been well constructed and can support $2M_\odot$ stars caused by three-body force (e.g., Ref. [179] for hyperon-mixed matter, and Ref. [180] for kaon-condensation matter). We are going to investigate cooling behavior in such EOSs with strangeness. We hope that further cooling observations are beneficial in exploring the NS matter.

Fourth, we examined the EOS dependence of X-ray burst light curves. We showed that larger-radius (large-symmetry-energy) EOSs have higher recurrence time Δt and peak luminosity $L_{\rm peak}$. This property can be explained by the surface gravity of NSs. We found the complexity of the mass relationship with burst behavior; if the strength of surface gravity is higher, Δt and $L_{\rm peak}$ become lower. Since the surface gravity has positively correlated with the central density of NSs, neutrino luminosity becomes higher in higher-mass NSs. Then, if the strength of neutrino cooling is higher, Δt and $L_{\rm peak}$ become higher in spite of being higher mass or surface gravity. Furthermore, we confirmed that the DU process makes Δt higher by $\sim 10\%$ in current studies. We also found the monotonic relation of α with the EOS, not neutrino cooling properties. Thus, α is the most powerful observational property to constrain EOSs. For the X-ray burst nucleosynthesis, if the NS radius is smaller, heavier p-rich elements are synthesized by the rp process as expected from the monotonic relation between α and the surface gravity.

We applied our models to the *Clocked burster* GS 1826–24. We found that larger-radius EOS such as the TM1 could be rejected due to high $L_{\rm peak}$ or causing photospheric radius expansion. We also suggested that whether the rapid cooling process occurs or not could be judged by the observations of GS 1826–24. Although many model parameters make the exact constraints on EOSs very difficult at present, future X-ray observations above all for accretion rate and compositions of accreted matter will help us probe the EOSs from *Clocked burster*.

The X-ray burst triggered by the unstable mixed H/He burning we considered in this thesis can be easily applied to the constraints on burst models because of the *Clocked bursters* and rp-process nucleosynthesis. However, other types of X-ray bursts could also become important. For instance, pure He burst triggered by unstable He burning has often been observed (e.g., Ref. [181]). Moreover, superburst triggered by unstable carbon burning has been found in a few LMXBs [171, 65, 182]. In a recent study, *"hyperburst"* triggered by unstable burning of heavier elements than ^{12}C has been reported to possibly occur in MAXI J0556–332 [183]. Since these bursts with a long burst duration are caused by the deeper NS layer compared with the mixed H/He bursts, the heating and cooling processes inside NSs should effectively work and change the ignition conditions (e.g., Refs. [92, 90]). Probing NS EOSs through their long-burst observations is therefore valuable.

We studied thermal evolution of NSs within spherically symmetric one-dimensional formulations, but multi-dimensional effects such as the NS spin, magnetic-field decays, and convection

are indispensable for describing the temperature of NSs more precisely. For example, rotational effects deform the NS asymmetrically, which gives rise to a difference in the distribution of surface temperature (e.g., Ref. [184]). In fact, such an inhomogeneity of surface temperature has been found in the pulsar PSR J0030+0451 as the southern hot spots [9, 10]. In LMXBs, it is natural to consider the rapid NS rotations because the companion star transports the angular momentum to the NSs through the accretion (e.g., Ref. [185]). In Type-I X-ray bursts, the NS rotation (and unstable convection) can significantly affect the dynamics of laterally propagating flames [186]. Besides, the magnetic-field effects on the thermal evolution have been widely discussed as well [187, 188, 189] (for a review, see Ref. [190]). We also plan to do multi-dimensional calculations of the thermal evolution of NSs based on the work in this thesis.

Throughout this thesis, we tried to constrain the NS EOSs from observations of temperature and luminosity. In particular, we found that cooling observations of isolated/accreting NSs constrain EOSs in terms of the presence or absence of fast cooling processes such as the DU process and pion condensation, while X-ray burst observations in terms of the softness and temperature of NSs. Since the NS mass and radius observations can only constrain the pressure-density relation of EOSs, temperature and luminosity observations are beneficial for probing heating and cooling mechanisms, ultimately clarifying what particles there are inside NSs. In that sense, our studies provide new tools to constrain the EOS as a function of density, temperature, and mass fraction of particles. As X-ray astronomy makes progress, our finding tools will become more valuable.

Acknowledgment

Bibliography

[1] T. Enoto and N. Yasutake, Butsuri（日本物理学会誌） **76**, 637 (2021).

[2] A. Akmal, V. R. Pandharipande, and D. G. Ravenhall, Phys. Rev. C**58**, 1804 (1998), nucl-th/9804027.

[3] I. Bombaci and D. Logoteta, Astron. Astrophys. **609**, A128 (2018), 1805.11846.

[4] V. Dexheimer and S. Schramm, Astrophys. J. **683**, 943 (2008), 0802.1999.

[5] K. Otto, M. Oertel, and B.-J. Schaefer, Phys. Rev. D**101**, 103021 (2020), 1910.11929.

[6] F. Gulminelli and A. R. Raduta, Phys. Rev. C**92**, 055803 (2015), 1504.04493.

[7] G. Baym *et al.*, Reports on Progress in Physics **81**, 056902 (2018), 1707.04966.

[8] G. Baym, S. Furusawa, T. Hatsuda, T. Kojo, and H. Togashi, Astrophys. J. **885**, 42 (2019), 1903.08963.

[9] G. Raaijmakers *et al.*, Astrophys. J. Lett. **887**, L22 (2019), 1912.05703.

[10] M. C. Miller, F. K. Lamb, A. J. Dittmann, S. Bogdanov, and Z. Arzoumanian *et al.* (*NICER* Collaboration), Astrophys. J. Lett. **887**, L24 (2019), 1912.05705.

[11] P. B. Demorest, T. Pennucci, S. M. Ransom, M. S. E. Roberts, and J. W. T. Hessels, Nature **467**, 1081 (2010), 1010.5788.

[12] T. E. Riley *et al.*, Astrophys. J. Lett. **918**, L27 (2021), 2105.06980.

[13] LIGO Scientific Collaboration and Virgo Collaboration, Phys. Rev. Lett. **119**, 161101 (2017), 1710.05832.

[14] A. Bauswein, O. Just, H.-T. Janka, and N. Stergioulas, Astrophys. J. Lett. **850**, L34 (2017), 1710.06843.

[15] C. J. Horowitz, Annals of Physics **411**, 167992 (2019), 1911.00411.

[16] B. T. Reed, F. J. Fattoyev, C. J. Horowitz, and J. Piekarewicz, Phys. Rev. Lett. **126**, 172503 (2021), 2101.03193.

[17] P.-G. Reinhard, X. Roca-Maza, and W. Nazarewicz, arXiv e-prints , arXiv:2206.03134 (2022), 2206.03134.

[18] C. de Jager and Z. Švestka, Sol. Phys. **100** (1985).

[19] Y. Fujimoto and K. Fukushima, Phys. Rev. D**105**, 014025 (2022), 2011.10891.

[20] J. Ghiglieri, A. Kurkela, M. Strickland, and A. Vuorinen, Phys. Rep. **880**, 1 (2020), 2002.10188.

[21] M. Oertel, M. Hempel, T. Klähn, and S. Typel, Rev. Mod. Phys. **89**, 015007 (2017), 1610.03361.

[22] P. Danielewicz, R. Lacey, and W. G. Lynch, Science **298**, 1592 (2002), nucl-th/0208016.

[23] J. Estee *et al.*, Phys. Rev. Lett. **126**, 162701 (2021), 2103.06861.

[24] F. Özel and P. Freire, Ann. Rev. Astron. Astrophy. **54**, 401 (2016), 1603.02698.

[25] J. M. Lattimer, Annual Review of Nuclear and Particle Science **62**, 485 (2012), 1305.3510.

[26] J. Antoniadis, P. C. C. Freire, N. Wex, T. M. Tauris, and R. S. Lynch *et al.*, Science **340**, 448 (2013), 1304.6875.

[27] H. T. Cromartie, E. Fonseca, S. M. Ransom, P. B. Demorest, and Z. Arzoumanian *et al.*, Nat. Astron. **4**, 72 (2020), 1904.06759.

[28] D. Chatterjee and I. Vidaña, European Physical Journal A **52**, 29 (2016), 1510.06306.

[29] N. Tsuneo, PhD thesis in Kyushu Univ. (2009).

[30] M. V. Beznogov, A. Y. Potekhin, and D. G. Yakovlev, Phys. Rep. **919**, 1 (2021), 2103.12422.

[31] D. G. Ravenhall, C. J. Pethick, and J. R. Wilson, Phys. Rev. Lett. **50**, 2066 (1983).

[32] M. Hashimoto, H. Seki, and M. Yamada, Progress of Theoretical Physics **71**, 320 (1984).

[33] K. Oyamatsu, Nucl. Phys. A**561**, 431 (1993).

[34] G. Watanabe, K. Iida, and K. Sato, Nucl. Phys. A**676**, 455 (2000), astro-ph/0001273.

[35] T. Noda *et al.*, Astrophys. J. **765**, 1 (2013), 1109.1080.

[36] S. L. Shapiro and S. A. Teukolsky, *Black holes, white dwarfs, and neutron stars : the physics of compact objects* (WILEY-VCH, 1983).

[37] P. Haensel and A. J. Jerzak, Astron. Astrophys. **179**, 127 (1987).

[38] G. G. Festa and M. A. Ruderman, Physical Review **180**, 1227 (1969).

[39] A. D. Kaminker, C. J. Pethick, A. Y. Potekhin, V. Thorsson, and D. G. Yakovlev, Astron. Astrophys. **343**, 1009 (1999), astro-ph/9812447.

[40] A. D. Kaminker, K. P. Levenfish, D. G. Yakovlev, P. Amsterdamski, and P. Haensel, Phys. Rev. D**46**, 3256 (1992).

[41] N. Itoh, H. Hayashi, A. Nishikawa, and Y. Kohyama, Astrophys. J. Suppl. **102**, 411 (1996).

[42] N. Itoh, T. Adachi, M. Nakagawa, Y. Kohyama, and H. Munakata, Astrophys. J. **339**, 354 (1989).

[43] D. G. Yakovlev, A. D. Kaminker, O. Y. Gnedin, and P. Haensel, Phys. Rep. **354**, 1 (2001), astro-ph/0012122.

[44] M. V. Beznogov, D. Page, and E. Ramirez-Ruiz, Astrophys. J. **888**, 97 (2020), 1908.04888.

[45] S. Tsuruta, Phys. Rep. **56**, 237 (1979).

[46] P. Haensel, A. D. Kaminker, and D. G. Yakovlev, Astron. Astrophys. **314**, 328 (1996), astro-ph/9604073.

[47] D. G. Yakovlev and K. P. Levenfish, Astron. Astrophys. **297**, 717 (1995).

[48] R. Tamagaki, Progress of Theoretical Physics **44**, 905 (1970).

[49] J. Bardeen, L. N. Cooper, and J. R. Schrieffer, Physical Review **108**, 1175 (1957).

[50] D. G. Yakovlev, A. D. Kaminker, and K. P. Levenfish, Astron. Astrophys. **343**, 650 (1999), astro-ph/9812366.

[51] D. Page, J. M. Lattimer, M. Prakash, and A. W. Steiner, Astrophys. J. Suppl. **155**, 623 (2004), astro-ph/0403657.

[52] D. Page, J. M. Lattimer, M. Prakash, and A. W. Steiner, Astrophys. J. **707**, 1131 (2009), 0906.1621.

[53] M. E. Gusakov, A. D. Kaminker, D. G. Yakovlev, and O. Y. Gnedin, Astron. Astrophys. **423**, 1063 (2004), astro-ph/0404002.

[54] D. G. Yakovlev and C. J. Pethick, Ann. Rev. Astron. Astrophy. **42**, 169 (2004), astro-ph/0402143.

[55] J. M. Lattimer, C. J. Pethick, M. Prakash, and P. Haensel, Phys. Rev. Lett. **66**, 2701 (1991).

[56] S. E. Woosley *et al.*, Astrophys. J. Suppl. **151**, 75 (2004), astro-ph/0307425.

[57] K. P. Levenfish and D. G. Yakovlev, Astronomy Reports **38**, 247 (1994).

[58] T. Muto, T. Takatsuka, R. Tamagaki, and T. Tatsumi, Prog. Theor. Phys. Suppl. **112**, 221 (1993).

[59] Y. Matsuo, H. Liu, M.-A. Hashimoto, and T. Noda, Int. J. Mod. Phys. E **27**, 1850067 (2018).

[60] A. B. Migdal, Rev. Mod. Phys. **50**, 107 (1978).

[61] D. N. Voskresensky, Phys. Atom. Nucl. **83**, 188 (2020).

[62] T. Takatsuka, K. Tamiya, T. Tatsumi, and R. Tamagaki, Progress of Theoretical Physics **59**, 1933 (1978).

[63] Y. Matsuo, PhD thesis in Kyushu Univ. (2017).

[64] Q. Z. Liu, J. van Paradijs, and E. P. J. van den Heuvel, Astron. Astrophys. **469**, 807 (2007), 0707.0544.

[65] M. Serino *et al.*, Publ. Astron. Soc. Japan. **68**, 95 (2016), 1608.04886.

[66] H. Liu *et al.*, Progress of Theoretical and Experimental Physics **2020**, 043E01 (2020).

[67] A. Y. Potekhin, A. I. Chugunov, and G. Chabrier, Astron. Astrophys. **629**, A88 (2019), 1907.08299.

[68] Y. Zhao *et al.*, Mon. Not. Roy. Astron. Soc. **488**, 4427 (2019), 1907.04969.

[69] N. N. Shchechilin, M. E. Gusakov, and A. I. Chugunov, Mon. Not. Roy. Astron. Soc. **507**, 3860 (2021), 2105.01991.

[70] N. N. Shchechilin, M. E. Gusakov, and A. I. Chugunov, Mon. Not. Roy. Astron. Soc. (2022), 2202.07486.

[71] J. Grindlay *et al.*, Astrophys. J. Lett. **205**, L127 (1976).

[72] D. K. Galloway *et al.*, Astrophys. J. Suppl. **249**, 32 (2020), 2003.00685.

[73] J. A. Hoffman, H. L. Marshall, and W. H. G. Lewin, Nature **271**, 630 (1978).

[74] W. H. G. Lewin, R. E. Rutledge, J. M. Kommers, J. van Paradijs, and C. Kouveliotou, Astrophys. J. Lett. **462**, L39 (1996).

[75] H. Schatz and K. E. Rehm, Nucl. Phys. A**777**, 601 (2006), astro-ph/0607624.

[76] R. H. Cyburt *et al.*, Astrophys. J. Suppl. **189**, 240 (2010).

[77] H. Schatz *et al.*, Phys. Rep. **294**, 167 (1998).

[78] H. Schatz, International Journal of Mass Spectrometry **251**, 293 (2006), astro-ph/0607625.

[79] H. Schatz and W. J. Ong, Astrophys. J. **844**, 139 (2017), 1610.07596.

[80] H. Schatz *et al.*, Phys. Rev. Lett. **86**, 3471 (2001), astro-ph/0102418.

[81] M. Y. Fujimoto, M. Sztajno, W. H. G. Lewin, and J. van Paradijs, Astrophys. J. **319**, 902 (1987).

[82] L. Keek, A. Heger, and J. J. M. in't Zand, Astrophys. J. **752**, 150 (2012), 1204.1343.

[83] D. K. Galloway, A. J. Goodwin, and L. Keek, Publ. Astron. Soc. Australia. **34**, e019 (2017), 1703.07485.

[84] Y. Tanaka, Black-Holes in X-Ray Binaries - X-Ray Properties of the Galactic Black-Hole Candidates, in *Two Topics in X-Ray Astronomy, Volume 1: X Ray Binaries. Volume 2: AGN and the X Ray Background*, edited by J. Hunt and B. Battrick, , ESA Special Publication Vol. 1, p. 3, 1989.

[85] A. Heger, A. Cumming, D. K. Galloway, and S. E. Woosley, Astrophys. J. Lett. **671**, L141 (2007), 0711.1195.

[86] R. H. Cyburt *et al.*, Astrophys. J. **830**, 55 (2016), 1607.03416.

[87] Z. Meisel, Astrophys. J. **860**, 147 (2018), 1805.05552.

[88] Z. Meisel, G. Merz, and S. Medvid, Astrophys. J. **872**, 84 (2019), 1812.07155.

[89] Z. Johnston, A. Heger, and D. K. Galloway, Mon. Not. Roy. Astron. Soc. **494**, 4576 (2020), 1909.07977.

[90] L. Keek and A. Heger, Astrophys. J. **743**, 189 (2011), 1110.2172.

[91] M. Y. Fujimoto, T. Hanawa, J. Iben, I., and M. B. Richardson, Astrophys. J. **278**, 813 (1984).

[92] A. Cumming, J. Macbeth, J. J. M. in 't Zand, and D. Page, Astrophys. J. **646**, 429 (2006), astro-ph/0508432.

[93] M. Y. Fujimoto, T. Hanawa, and S. Miyaji, Astrophys. J. **247**, 267 (1981).

[94] H. Togashi *et al.*, Nucl. Phys. A**961**, 78 (2017), 1702.05324.

[95] J. M. Lattimer and D. F. Swesty, Nucl. Phys. A**535**, 331 (1991).

[96] H. Shen, H. Toki, K. Oyamatsu, and K. Sumiyoshi, Nucl. Phys. A**637**, 435 (1998), nucl-th/9805035.

[97] H. Shen, H. Toki, K. Oyamatsu, and K. Sumiyoshi, Prog. Theor. Phys. **100**, 1013 (1998), nucl-th/9806095.

[98] H. Shen, H. Toki, K. Oyamatsu, and K. Sumiyoshi, Astrophys. J. Suppl. **197**, 20 (2011), 1105.1666.

[99] K. Sumiyoshi, K. Nakazato, H. Suzuki, J. Hu, and H. Shen, Astrophys. J. **887**, 110 (2019), 1908.02928.

[100] H. Shen, F. Ji, J. Hu, and K. Sumiyoshi, Astrophys. J. **891**, 148 (2020), 2001.10143.

[101] K. Hebeler, J. M. Lattimer, C. J. Pethick, and A. Schwenk, Astrophys. J. **773**, 11 (2013), 1303.4662.

[102] U. Garg and G. Colò, Progress in Particle and Nuclear Physics **101**, 55 (2018), 1801.03672.

[103] G. Baym, C. Pethick, and P. Sutherland, Astrophys. J. **170**, 299 (1971).

[104] M. B. Richardson, H. M. van Horn, K. F. Ratcliff, and R. C. Malone, Astrophys. J. **255**, 624 (1982).

[105] G. F. Burgio, H. J. Schulze, I. Vidaña, and J. B. Wei, Progress in Particle and Nuclear Physics **120**, 103879 (2021), 2105.03747.

[106] T. Muto and T. Tatsumi, Prog. Theor. Phys. **78**, 1405 (1987).

[107] H. Umeda, K. Nomoto, S. Tsuruta, T. Muto, and T. Tatsumi, Astrophys. J. **431**, 309 (1994).

[108] K. Yako, H. Sakai, M. B. Greenfield, K. Hatanaka, and M. Hatano *et al.*, Phys. Lett. B **615**, 193 (2005), nucl-ex/0411011.

[109] M. Ichimura, H. Sakai, and T. Wakasa, Prog. Part. Nucl. Phys. **56**, 446 (2006).

[110] LIGO Scientific Collaboration and Virgo Collaboration, Phys. Rev. Lett. **121**, 161101 (2018), 1805.11581.

[111] D. Blaschke, A. Ayriyan, D. E. Alvarez-Castillo, and H. Grigorian, Universe **6**, 81 (2020), 2005.02759.

[112] A. W. Steiner, J. M. Lattimer, and E. F. Brown, Astrophys. J. **722**, 33 (2010), 1005.0811.

[113] S. van Straaten, E. C. Ford, M. van der Klis, M. Méndez, and P. Kaaret, Astrophys. J. **540**, 1049 (2000), astro-ph/0001480.

[114] J. A. Pons *et al.*, Astrophys. J. **564**, 981 (2002), astro-ph/0107404.

[115] J. E. Trümper, V. Burwitz, F. Haberl, and V. E. Zavlin, Nucl. Phys. B Proc. Suppl. **132**, 560 (2004), astro-ph/0312600.

[116] S. Bogdanov, Astrophys. J. **762**, 96 (2013), 1211.6113.

[117] D. J. Reardon, G. Hobbs, W. Coles, Y. Levin, and Keith *et al.*, Mon. Not. Roy. Astron. Soc. **455**, 1751 (2016), 1510.04434.

[118] R. C. Tolman, Physical Review **55**, 364 (1939).

[119] J. R. Oppenheimer and G. M. Volkoff, Physical Review **55**, 374 (1939).

[120] T. Kojo, arXiv e-prints , arXiv:2106.06687 (2021).

[121] D. Hiramatsu, D. A. Howell, S. D. Van Dyk, J. A. Goldberg, and K. Maeda *et al.*, Nat. Astron. (2021), 2011.02176.

[122] P. Podsiadlowski *et al.*, Mon. Not. Roy. Astron. Soc. **361**, 1243 (2005), astro-ph/0506566.

[123] K. A. Maslov, E. E. Kolomeitsev, and D. N. Voskresensky, Phys. Lett. B **748**, 369 (2015), 1504.02915.

[124] F. S. Kitaura, H. T. Janka, and W. Hillebrandt, Astron. Astrophys. **450**, 345 (2006), astro-ph/0512065.

[125] K. S. Thorne, Astrophys. J. **212**, 825 (1977).

[126] A. Y. Potekhin and G. Chabrier, Astron. Astrophys. **609**, A74 (2018), 1711.07662.

[127] D. Sugimoto, K. Nomoto, and Y. Eriguchi, Progress of Theoretical Physics Supplement **70**, 115 (1981).

[128] H. Liu, Y. Matsuo, M.-a. Hashimoto, T. Noda, and M. Y. Fujimoto, Journal of the Physical Society of Japan **86**, 123901 (2017), 1703.01734.

[129] H. Schatz, L. Bildsten, A. Cumming, and M. Wiescher, Astrophys. J. **524**, 1014 (1999), astro-ph/9905274.

[130] D. A. Baiko, P. Haensel, and D. G. Yakovlev, Astron. Astrophys. **374**, 151 (2001), astro-ph/0105105.

[131] A. Y. Potekhin, J. A. Pons, and D. Page, Space Sci. Rev. **191**, 239 (2015), 1507.06186.

[132] P. S. Shternin and D. G. Yakovlev, Phys. Rev. D**75**, 103004 (2007), 0705.1963.

[133] A. Dohi, M.-a. Hashimoto, R. Yamada, Y. Matsuo, and M. Y. Fujimoto, Progress of Theoretical and Experimental Physics **2020**, 033E02 (2020), 2001.08367.

[134] S.-i. Fujimoto, M.-a. Hashimoto, O. Koike, K. Arai, and R. Matsuba, Astrophys. J. **585**, 418 (2003), astro-ph/0211171.

[135] O. Koike, M.-a. Hashimoto, R. Kuromizu, and S.-i. Fujimoto, Astrophys. J. **603**, 242 (2004).

[136] A. Dohi, H. Liu, T. Noda, and M.-A. Hashimoto, International Journal of Modern Physics E **31**, 2250006 (2022), 2112.13302.

[137] A. Dohi, K. Nakazato, M.-a. Hashimoto, M. Yasuhide, and T. Noda, Prog. Theor. Exp. Phys. **2019**, 113E01 (2019), 1910.01431.

[138] I. Tews, J. M. Lattimer, A. Ohnishi, and E. E. Kolomeitsev, Astrophys. J. **848**, 105 (2017), 1611.07133.

[139] D. Page, J. M. Lattimer, M. Prakash, and A. W. Steiner, Eds. K. H. Bennemann and J. B. Ketterson, (2013), 1302.6626.

[140] W. C. G. Ho, K. G. Elshamouty, C. O. Heinke, and A. Y. Potekhin, Phys. Rev. C**91**, 015806 (2015), 1412.7759.

[141] L. G. Cao, U. Lombardo, and P. Schuck, Phys. Rev. C**74**, 064301 (2006), nucl-th/0608005.

[142] S. Gandolfi, A. Y. Illarionov, F. Pederiva, K. E. Schmidt, and S. Fantoni, Phys. Rev. C**80**, 045802 (2009), 0907.1588.

[143] J. M. C. Chen, J. W. Clark, R. D. Davé, and V. V. Khodel, Nucl. Phys. A**555**, 59 (1993).

[144] S. Tsuruta, Phys. Rep. **292**, 1 (1998).

[145] Ø. Elgarøy, L. Engvik, M. Hjorth-Jensen, and E. Osnes, Nucl. Phys. A**607**, 425 (1996), nucl-th/9604032.

[146] T. Takatsuka and R. Tamagaki, Prog. Theor. Phys. **112**, 37 (2004), nucl-th/0402011.

[147] A. Y. Potekhin, G. Chabrier, and D. G. Yakovlev, Astron. Astrophys. **323**, 415 (1997), astro-ph/9706148.

[148] Y. Lim, C. H. Hyun, and C.-H. Lee, Int. J. Mod. Phys. E **26**, 1750015 (2017).

[149] T. Takatsuka, Prog. Theor. Phys. **48**, 1517 (1972).

[150] J. Yasuda, M. Sasano, R. G. T. Zegers, H. Baba, and D. Bazin *et al.*, Phys. Rev. Lett. **121**, 132501 (2018).

[151] T. Suzuki and H. Sakai, Physics Letters B **455**, 25 (1999).

[152] T. Muto, R. Tamagaki, and T. Tatsumi, Progress of Theoretical Physics Supplement **112**, 159 (1993).

[153] D. G. Ravenhall and C. J. Pethick, Astrophys. J. **424**, 846 (1994).

[154] H.-L. Liu *et al.*, Phys. Rev. D**104**, 123004 (2021), 2110.09729.

[155] P. Haensel and J. L. Zdunik, Astron. Astrophys. **227**, 431 (1990).

[156] P. Haensel and J. L. Zdunik, Astron. Astrophys. **480**, 459 (2008), 0708.3996.

[157] Y.-C. Ma *et al.*, Research in Astronomy and Astrophysics **20**, 049 (2020).

[158] S. S. Tsygankov, R. Wijnands, A. A. Lutovinov, N. Degenaar, and J. Poutanen, Mon. Not. Roy. Astron. Soc. **470**, 126 (2017), 1703.04634.

[159] Z.-F. Gao, N. Wang, H. Shan, X.-D. Li, and W. Wang, Astrophys. J. **849**, 19 (2017), 1709.03459.

[160] A. Dohi *et al.*, Astrophys. J. **923**, 64 (2021), 2105.13958.

[161] A. F. Fantina *et al.*, Astron. Astrophys. **620**, A105 (2018), 1806.03861.

[162] H. Sotani, N. Nishimura, and T. Naito, Progress of Theoretical and Experimental Physics **2022**, 041D01 (2022), 2203.05410.

[163] V. Baruah Thapa and M. Sinha, arXiv e-prints , arXiv:2203.02272 (2022), 2203.02272.

[164] S. Lalit, Z. Meisel, and E. F. Brown, Astrophys. J. **882**, 91 (2019), 1906.01535.

[165] O. Koike, M. Hashimoto, K. Arai, and S. Wanajo, Astron. Astrophys. **342**, 464 (1999).

[166] D. Sugimoto and M. Y. Fujimoto, Publ. Astron. Soc. Japan. **30**, 467 (1978).

[167] R. E. Taam, Astrophys. J. **241**, 358 (1980).

[168] A. Heger, A. Cumming, and S. E. Woosley, Astrophys. J. **665**, 1311 (2007), astro-ph/0511292.

[169] N. Lampe, A. Heger, and D. K. Galloway, Astrophys. J. **819**, 46 (2016), 1512.05769.

[170] S. Gupta, E. F. Brown, H. Schatz, P. Möller, and K.-L. Kratz, Astrophys. J. **662**, 1188 (2007), astro-ph/0609828.

[171] J. J. M. in't Zand, E. Kuulkers, F. Verbunt, J. Heise, and R. Cornelisse, Astron. Astrophys. **411**, L487 (2003), astro-ph/0310364.

[172] M. Kubota *et al.*, Publ. Astron. Soc. Japan. **71**, 33 (2019), 1902.05225.

[173] D. Page, M. Prakash, J. M. Lattimer, and A. W. Steiner, Phys. Rev. Lett. **106**, 081101 (2011), 1011.6142.

[174] P. S. Shternin, D. G. Yakovlev, C. O. Heinke, W. C. G. Ho, and D. J. Patnaude, Mon. Not. Roy. Astron. Soc. **412**, L108 (2011), 1012.0045.

[175] R. Lau *et al.*, Astrophys. J. **859**, 62 (2018), 1803.03818.

[176] H. Takahashi, J. K. Ahn, H. Akikawa, S. Aoki, and K. Arai *et al.*, Phys. Rev. Lett. **87**, 212502 (2001).

[177] T. Takatsuka, S. Nishizaki, Y. Yamamoto, and R. Tamagaki, Prog. Theor. Phys. **115**, 355 (2006), nucl-th/0601043.

[178] H. Ekawa *et al.*, Progress of Theoretical and Experimental Physics **2019**, 021D02 (2019), 1811.07726.

[179] H. Togashi, E. Hiyama, Y. Yamamoto, and M. Takano, Phys. Rev. C**93**, 035808 (2016), 1602.08106.

[180] T. Muto, T. Maruyama, and T. Tatsumi, Physics Letters B **820**, 136587 (2021), 2106.03449.

[181] D. K. Galloway and A. Cumming, Astrophys. J. **652**, 559 (2006), astro-ph/0607213.

[182] W. B. Iwakiri *et al.*, Publ. Astron. Soc. Japan. **73**, 1405 (2021), 2108.13568.

[183] D. Page *et al.*, arXiv e-prints , arXiv:2202.03962 (2022), 2202.03962.

[184] M. V. Beznogov, J. Novak, D. Page, and A. R. Raduta, arXiv e-prints , arXiv:2206.04539 (2022), 2206.04539.

[185] N. Kuechel, M. Teter, A. C. Liebmann, and S. Tsuruta, arXiv e-prints , arXiv:2010.06638 (2020), 2010.06638.

[186] A. Harpole *et al.*, Astrophys. J. **912**, 36 (2021), 2102.00051.

[187] D. Viganò *et al.*, Mon. Not. Roy. Astron. Soc. **434**, 123 (2013), 1306.2156.

[188] N. Yasutake, K. Kotake, M. Kutsuna, and T. Shigeyama, Publ. Astron. Soc. Japan. **66**, 50 (2014), 1401.2723.

[189] D. Viganò, A. Garcia-Garcia, J. A. Pons, C. Dehman, and V. Graber, Computer Physics Communications **265**, 108001 (2021), 2104.08001.

[190] J. A. Pons and D. Viganò, Living Reviews in Computational Astrophysics **5**, 3 (2019), 1911.03095.